

PL-TR-96-2094(I)

**PLASMA AND FLOWFIELD INDUCED EFFECTS ON
RE-ENTRY VEHICLES FOR L-BAND AT NEAR-
BROADSIDE ASPECT ANGLES**

**Volume I: Experimental Measurements Program Summary And
Aerothermal Data Analysis**

**Kenneth M. Chadwick
Donald W. Boyer
Stephen N. Andre**

**Calspan SRL Corporation
PO Box 400
Buffalo, NY 14225**

September 1996

**Final Report
January 1994 - September 1996**

APPROVED FOR PUBLIC RELEASE; DISTRIBUTION UNLIMITED

19961106 141



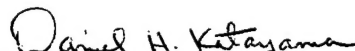
**PHILLIPS LABORATORY
Directorate of Geophysics
AIR FORCE MATERIEL COMMAND
HANSCOM AFB, MA 01731-3010**

DTIC QUALITY INSPECTED 1

"This technical report has been reviewed and is approved for publication"



ROBERT A. MORRIS
Contract Manager



DANIEL H. KATAYAMA
Branch Chief



CHARLES P. PIKE
Division Director

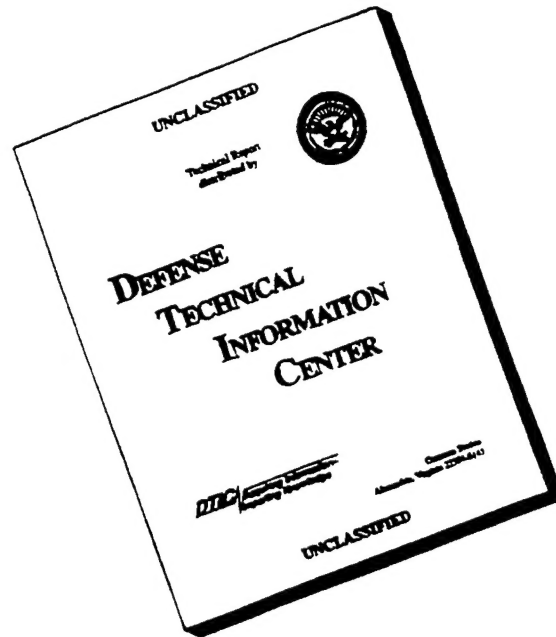
This report has been reviewed by the ESC Public Affairs Office (PA) and is releasable to the National Technical Information Service (NTIS).

Qualified requestors may obtain additional copies from the Defense Technical Information Center (DTIC). All others should apply to the National Technical Information Service (NTIS).

If your address has changed, if you wish to be removed from the mailing list, if the addressee is no longer employed by your organization, please notify PL/IM, 29 Randolph Road, Hanscom AFB, MA 01731-3010. This will assist us in maintaining a current mailing list.

Do not return copies of this report unless contractual obligations or notices on a specific document require that it be returned.

DISCLAIMER NOTICE



**THIS DOCUMENT IS BEST
QUALITY AVAILABLE. THE
COPY FURNISHED TO DTIC
CONTAINED A SIGNIFICANT
NUMBER OF PAGES WHICH DO
NOT REPRODUCE LEGIBLY.**

REPORT DOCUMENTATION PAGE			Form Approved OMB No. 0704-0188	
Public reporting burden for this collection of information is estimated to average 1 hour per response, including the time for reviewing instructions, searching existing data sources, gathering and maintaining the data needed, and completing and reviewing the collection of information. Send comments regarding this burden estimate or any other aspect of this collection of information, including suggestions for reducing this burden, to Washington Headquarters Services, Directorate for Information Operations and Reports, 1215 Jefferson Davis Highway, Suite 1204, Arlington, VA 22202-4302, and to the Office of Management and Budget, Paperwork Reduction Project (0704-0188), Washington, DC 20503.				
1. AGENCY USE ONLY (Leave blank)		2. REPORT DATE September 1996		3. REPORT TYPE AND DATES COVERED Final (January 1994-September 1996)
4. TITLE AND SUBTITLE Plasma and Flowfield Induced Effects on Re-Entry Vehicles for L-Band at Near-Broadside Aspect Angles. Volume I: Experimental Measurements Program Summary and Aerothermal Data Analysis			5. FUNDING NUMBERS PE:62101F PR 4087 TA GJ WU AA Contract F19628-94-C-0015	
6. AUTHOR(S) Kenneth M. Chadwick Donald W. Boyer Stephen N. Andre				
7. PERFORMING ORGANIZATION NAME(S) AND ADDRESS(ES) Calspan SRL Corporation PO Box 400 Buffalo, NY 14225			8. PERFORMING, ORGANIZATION REPORT NUMBER	
9. SPONSORING/MONITORING AGENCY NAME(S) AND ADDRESS(ES) Phillips Laboratory 29 Randolph Road Hanscom AFB, MA 01731-3010 Contract Manager: Robert Morris/GPID			10. SPONSORING/MONITORING AGENCY REPORT NUMBER PL-TR-96-2094(I)	
11. SUPPLEMENTARY NOTES				
12a. DISTRIBUTION/AVAILABILITY STATEMENT Approved for public release; distribution unlimited			12b. DISTRIBUTION CODE	
13. ABSTRACT (Maximum 200 words) A laboratory measurements program has been performed in the Calspan 96-inch hypersonic shock tunnel which has provided a data base on the effects of the ionized flow field about a reentry vehicle on RF energy propagation. The measurements, performed under laminar flow conditions, provide data on plasma-induced phase shift and attenuation of incident (uplink) RF signals for three aspect angles around broadside of the test vehicle, as well as measurements of reflection coefficient of an open ended waveguide antenna and mutual coupling between antennas on the vehicle. Vehicle orientations included combinations of pitch and yaw so as to include the effects of crossflow on the measurements. The experiments were performed at an L-band frequency, under freestream test conditions of 14,000 ft/sec at an equivalent density altitude of 140 kft. Surface distributions of pressure and heat transfer were measured, as well as profiles of the electron number density through the ionized flow field by means of thin-wire electrostatic probes.				
14. SUBJECT TERMS Plasma Flowfield Re-entry vehicles			15. NUMBER OF PAGES 122	
			16. PRICE CODE	
17. SECURITY CLASSIFICATION OF REPORT Unclassified	18. SECURITY CLASSIFICATION OF THIS PAGE Unclassified	19. SECURITY CLASSIFICATION OF ABSTRACT Unclassified	20. LIMITATION OF ABSTRACT SAR	

CONTENTS

Foreword	ix
1.0 Introduction	1
2.0 Design Of The Experiments	3
2.1 Analysis Of Electromagnetic (Em) Tunnel Environment For Testing At L-Band	6
2.2 Investigation Of The Electromagnetic Environment Within The Shock Tunnel	8
2.3 Test Model.....	13
2.3.1 Test Model Antenna Configuration	13
2.3.2 Model Instrumentation	14
2.3.3 Surface Instrumentation	14
2.3.4 Thin Wire Electrostatic Probes.....	18
2.4 Microwave System Design	18
2.4.1 Antenna Design For Installation In The Shock Tunnel.....	18
2.4.2 Microwave Instrumentation Data Multiplexing.....	21
2.4.3 Microwave Instrumentation Design.....	21
3.0 Model Antenna Measurements And Calibration Procedures	24
3.1 Antenna Measurements	24
3.2 Calibration Of Microwave Instrumentation.....	27
3.2.1 Measurement Of Antenna Aperture/Mixer Reflection Coefficients	27
3.2.2 Measurement Of I/Q Channel Relative Gain.....	27
3.2.3 Receiver Calibration.....	28
3.2.4 Reflectometer Calibration	28
4.0 Numerical Analysis Of The Model Flowfield.....	29
5.0 Results	39
5.1 Test Stream Diagnostics And Condition	39
5.2 Aerothermal Measurements.....	42
5.3 Electron Number Density Measurements	49
6.0 Summary And Conclusions	62
7.0 References	64

CONTENTS (cont)

Appendix A	Antenna Coupling Data Reduction To Obtain Antenna Scattering Parameters.....	66
Appendix B	Conversion Of Shock Tunnel Run Data To Antennaaperture Planes.....	70
Appendix C	Thin-Wire, Swept-Voltage Probe Measurements Of Electron Number Densities In Plasma Flow Fields	74
Appendix D	Bowshock Radiation Study.....	80
Appendix E	Flush-Mounted Surface Electrostatic Probe Data	93
Appendix F	Thin Wire Electrostatic Probe Data	98

FIGURES

<u>Figure</u>	<u>Page</u>
1 Schematic Of The Experimental Arrangement Used For The Hypersonic Shock Tunnel Tests	3
2 Photograph of the Driven Tube and Test Section of the 96" Hypersonic Shock Tunnel	4
3 Photograph of the Driver Section of the 96" Hypersonic Shock Tunnel	5
4 Photograph of the Microwave Absorber Material Installed In the Shock Tunnel Test Section.....	9
5 Sketch of the Electromagnetic Environment Test Equipment	10
6 Photograph of the Receiver Waveguide Antenna for the EM Environment Tests	11
7 Illustrative Record of Received Waveguide Antenna Signal for Minimization of Scattered Return Effects.....	12
8 Design Drawing Of The Vehicle Test Model	15
9 Photograph Of The Vehicle Test Model	16
10 Schematic of the Surface Instrumentation	17
11 Photograph of the Thin-Wire Electrostatic Probe Rake.....	19
12 Schematic of the L-Band Microwave System	23
13 Sketch of the Important Flowfield Regions for the Computations	30
14 Species Distribution for Airflow Expansion in Hypersonic Nozzle.....	32
15 Flowfield Gasdynamic Parameter Distributions Normal to the L1 Antenna Aperture	34
16 Flowfield Gasdynamic Parameter Distributions Normal to the L2 Antenna Aperture	35
17 Flowfield Gasdynamic Parameter Distributions Normal to the L3 Antenna Aperture	36
18 Flowfield Species Mole Fraction Distributions Normal to Antenna 1, L1 Aperture	37
19 Freestream Flowfield Pitot Measurements with Navier-Stokes Prediction.....	38
20 Photograph of the Highly Instrumented Flowfield Survey Rake	40
21 Summary of the Freestream Variables for the Test Program	41
22 Contour Map of the Flow Around the nose of the Test Model	43
23 Test Model Surface Pressure Data.....	44
24 Test Model Surface Pressure Data.....	45
25 Test Model Surface Pressure Data.....	46
26 Test Model Surface Pressure Data.....	47
27 Schematic of the Model Orientation Scheme	48
28 Test Model Surface Heat Transfer Data	50
29 Test Model Surface Heat Transfer Data	51
30 Test Model Surface Heat Transfer Data	52
31 Test Model Surface Heat Transfer Data	53
32 Schematic Showing the Locations of the Heat Transfer Gauges and the L-Band Antennas	54
33 Electron Number Densities for Test Runs 2, 25 and 33 at 0° AOA	55
34 Electron Number Density for the +2° Pitch Test Model Orientation.....	57
35 Electron Number Density for the +6° Pitch Test Model Orientation.....	58

FIGURES (cont)

<u>Figure</u>	<u>Page</u>
36 Electron Number Density for the +2° Yaw Test Model Orientation	59
37 Electron Number Density for the -2° Pitch Test Model Orientation.....	60
38 Electron Number Density for the -6° Pitch Test Model Orientation.....	61
A-1 Antenna Coupling Configuration and Symbol Definition	68
C-1 Sketch of the Complete Ion Probe Characteristic	79
D-1 Experimental Arrangement for Gas Cap Radiation Measurement.....	81
D-2 UV Spectra Illustration OH And Cu, Test Run 12	83
D-3 Spectral Measurements of Na and Cu, Test Run 23	84
D-4 Spectral Measurements of Na and Cu, Test Run 23	85
D-5 Spectral Measurements, Test Run 22	87
D-6 Calibrated Spectral Measurements, Test Run 21	89
E-1 Electrostatic Surface Probe Locations	94
E-2 Electrostatic Probe Data Summary	97
F-1 Electron Number Density Profile, Test Run 01	98
F-2 Electron Number Density Profile, Test Run 02	98
F-4 Electron Number Density Profile, Test Run 04	99
F-5 Electron Number Density Profile, Test Run 05	99
F-7 Electron Number Density Profile, Test Run 07	100
F-8 Electron Number Density Profile, Test Run 08	100
F-10 Electron Number Density Profile, Test Run 10	101
F-11 Electron Number Density Profile, Test Run 11	101
F-12 Electron Number Density Profile, Test Run 12	102
F-13 Electron Number Density Profile, Test Run 13	102
F-14 Electron Number Density Profile, Test Run 14	103
F-15 Electron Number Density Profile, Test Run 15	103
F-16 Electron Number Density Profile, Test Run 16	104
F-17 Electron Number Density Profile, Test Run 17	104
F-18 Electron Number Density Profile, Test Run 18	105
F-19 Electron Number Density Profile, Test Run 19	105
F-20 Electron Number Density Profile, Test Run 20	106
F-21 Electron Number Density Profile, Test Run 21	106
F-22 Electron Number Density Profile, Test Run 22	107
F-23 Electron Number Density Profile, Test Run 23	107
F-24 Electron Number Density Profile, Test Run 24	108
F-25 Electron Number Density Profile, Test Run 25	108
F-26 Electron Number Density Profile, Test Run 26	109
F-27 Electron Number Density Profile, Test Run 27	109
F-28 Electron Number Density Profile, Test Run 28	110
F-29 Electron Number Density Profile, Test Run 29	110
F-30 Electron Number Density Profile, Test Run 30	111
F-31 Electron Number Density Profile, Test Run 31	111
F-32 Electron Number Density Profile, Test Run 32	112
F-33 Electron Number Density Profile, Test Run 33	112

TABLES

<u>Table</u>	<u>Page</u>
1 Measured Antenna Free Space Reflection Coefficients (Input Scattering Parameters At Antenna Apertures)	25
2 Measured Free Space Antenna Coupling (Input Scattering Parameters At Antenna Apertures)	26
A1 Scattering Matrix for Mutual Coupling	69
E-1 Flush Mounted Electrostatic Probe Results	95

FOREWORD

This research effort was supported by the Air Force Electronics Systems Center, Hanscom Air Force Base, Hanscom MA with Dr. Robert Morris of the Air Force Geophysics Laboratory as technical monitor.

Particular acknowledgment must be given to Dr. Donald W. Boyer who served as Principal Investigator for much of the program and to Dr. Stephen Andre of Buffalo State University for the design and operation of the microwave electronics and for much of the analysis of the RF/plasma database.

Additionally, many thanks for assistance received from Dr. Emmett Sutton of Concord Sciences, Concord, MA and Dr. Tobenette Holtz of TRW, San Bernadino, CA.

Also, thanks to Robert Streit and many other Calspan SRL employees for their hard work and overall effort to make this research program a success.

1.0

INTRODUCTION

The potential for signal quality degradation in electromagnetic propagation through the flowfields surrounding hypervelocity vehicles during reentry is of specific interest to guidance sensor applications. Aerodynamic phenomena introduce density and temperature gradients into the non-planar flowfield behind the bow shock, and aerothermal phenomena introduce plasma levels as a result of thermal ionization processes.

Electromagnetic radiation will therefore experience attenuation, phase shift and scattering in propagating through such environments. The severity of these effects on guidance performance will depend upon the magnitude of the signal frequency relative to the plasma frequency (local electron number density, n_e) and the collision frequency, as well as their gradients. These plasma-microwave interaction effects will further be rendered more complex by the asymmetry of the flow field plasma due to vehicle angle of attack. Antenna window heating can also present critical problems in the flight case as high heat transfer rates can initiate softening or melting of the material leading to shape distortion, ablation and changes in refractive index. Microwave signal processing must account for all of these perturbation effects in order to provide reliable homing/guidance updates.

It is evident that RF transmission effects errors can result from aerodynamic and aerothermal effects, and homing concept development must address all of these issues. Codes must therefore be developed and validated to ensure an understanding of and a predictive capability for, the analysis of all phenomena capable of affecting microwave sensor performance. Validation of these codes necessarily requires a data base. Such a data base can be obtained from dedicated experiments performed in a test facility which is capable of generating some of the aerodynamic and aerothermal conditions wherein plasma-environment issues, including angle of attack effects, can be quantitatively examined in a well-conceived laboratory measurements program.

This report summarizes the experiment design, performance techniques and the results of a test program whose objective was to develop a data base on the interaction of L-band (RF) electromagnetic radiation with the ionized flow field about a reentry vehicle, for purposes of analytic code validation. The experiments were performed in the Calspan 96-inch hypersonic shock tunnel wherein plasma conditions were generated, aerodynamically, in the test vehicle flow field under laminar flow conditions appropriate to high altitude reentry. The plasma induced phase shift and attenuation of the incident RF energy were measured simultaneously at

five vehicle mounted antennas for three different incident angles of irradiation of the test vehicle, about broadside, at selected vehicle orientations so as to include the effects of pitch and yaw (crossflow conditions) on the measurements. The transmission measurement was time multiplexed with a measurement of coupling among antennas on the vehicle with one of the vehicle antennas used as the driven antenna. The reflection coefficient of the driven vehicle antenna was also measured.

This report will present a description of the RF-plasma interaction effects measurements program including the experiment design, the measured electron number density profiles in the vehicle flow field and the surface heat transfer rate distributions.

2.0

DESIGN OF THE EXPERIMENTS

The considerations to be addressed in the design of an experimental program to furnish a data base on RF-ionized flow field interaction effects included the selection of appropriate shock tunnel test conditions, the determination of the RF transmission and reflection characteristics that could be provided within the hypersonic test facility, and the selection of the test frequency. Dedicated studies were required to investigate the electromagnetic quality of the test environment afforded by the shock tunnel in order to identify reflection and scattering sources which could interfere (via multipath effects) with the program measurements unless adequately absorbed or screened against. The experiment design was based on a previously developed test vehicle geometry and antenna configuration, model instrumentation and microwave system necessary to provide the RF propagation requirements and the recording of the RF-plasma interaction effects.

Major elements of this test program (the test vehicle and portions of the microwave instrumentation and calibration procedures) were developed in a previous program and have been described in detail in Reference 1. The modifications incorporated for the experiments of the present program will be described in this report. A schematic of the experimental arrangement employed in all the program measurements is shown in Figure 1. This figure will serve as a convenient reference in the following discussions of the various elements of the experiment design. Figures 2 and 3 show photocopies of the 96" HST driven tube, test chamber, and driver section.

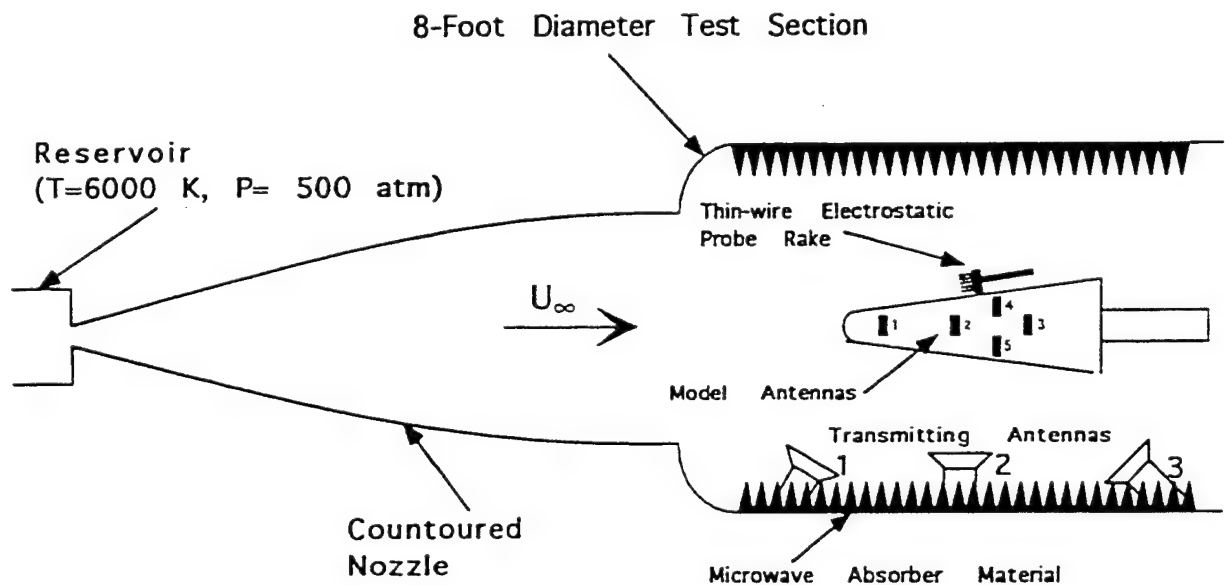


Figure 1 Schematic Of The Experimental Arrangement Used For The Hypersonic Shock Tunnel Tests

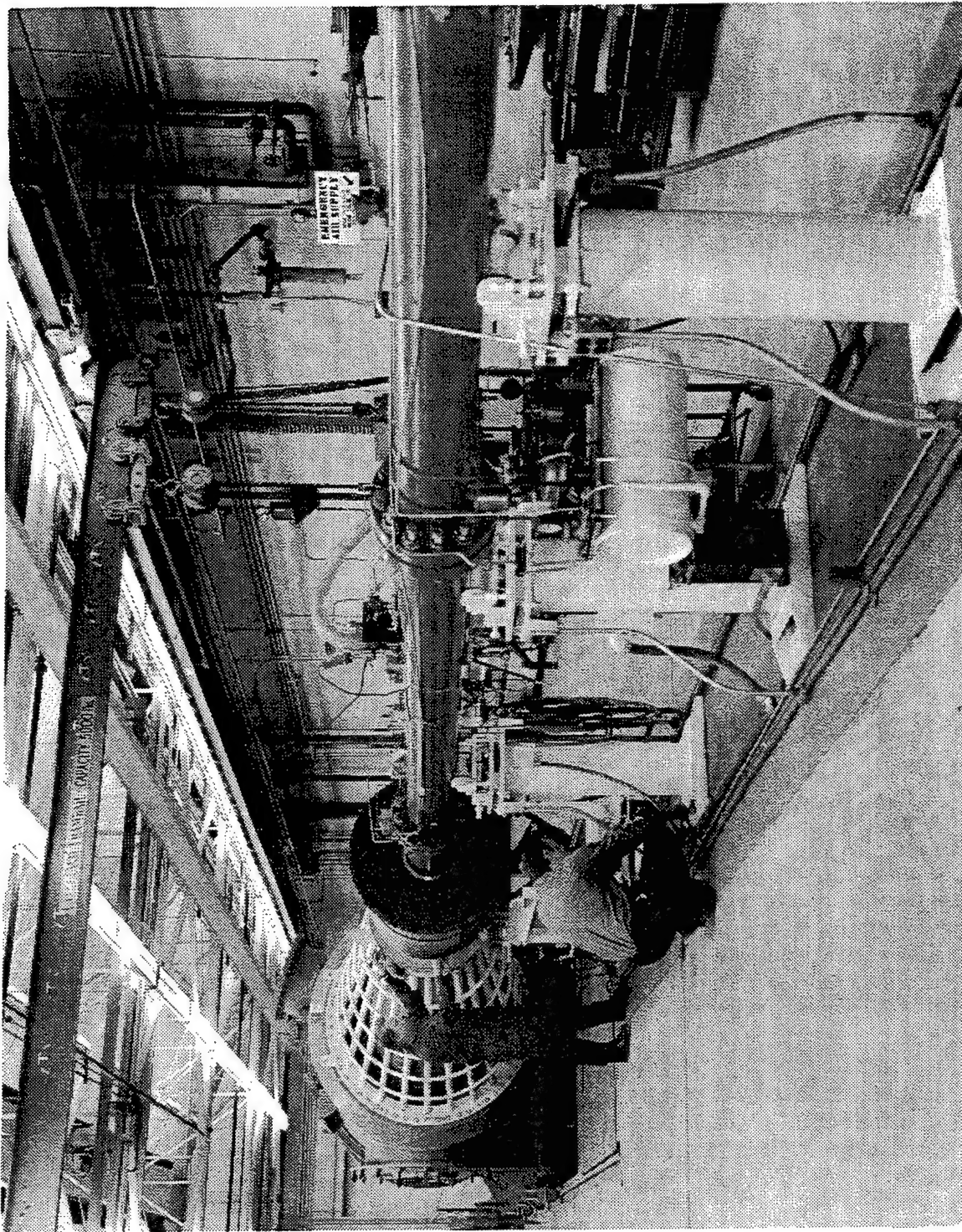


Figure 2 Photograph of the Driven Tube and Test Section of the 96" Hypersonic Shock Tunnel

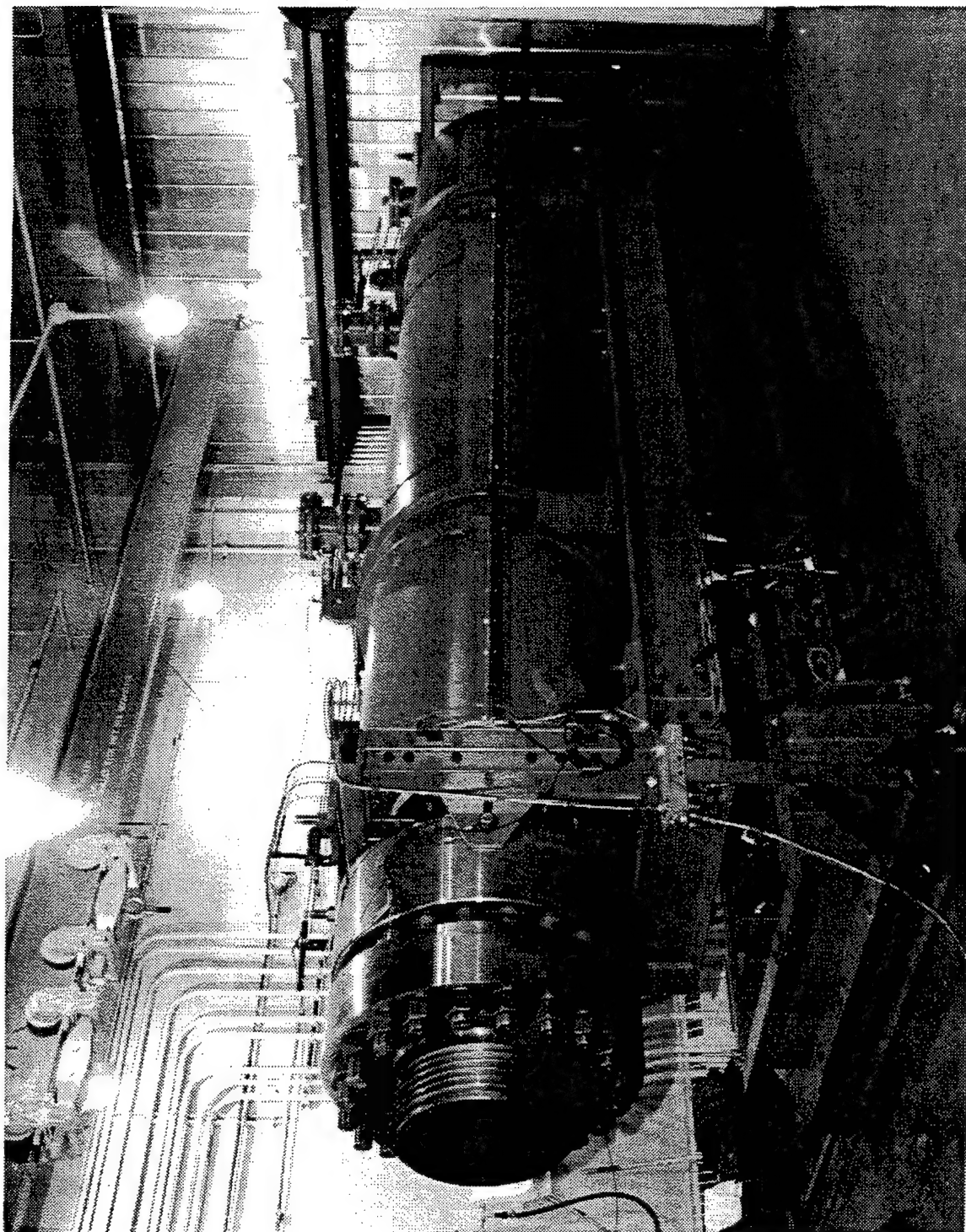


Figure 3 Photograph of the Driver Section of the 96" Hypersonic Shock Tunnel

2.1 Analysis Of Electromagnetic (Em) Tunnel Environment For Testing At L-Band

Testing at L-band illumination of the test vehicle at broadside and angles about broadside requires transmit antennas to be located at distances beyond the far-field of the antennas. Analyses were performed of the electromagnetic environment which could be provided in the shock tunnel for this configuration. Two installation sites were considered :

1. installation in the eight foot diameter test section of the shock tunnel, which requires absorber material to be placed around the inside surface to reduce reflections from the steel walls, and

2. installation in a previously-designed cylindrical dielectric test section which could be placed between the nozzle exit plane and the test section; the problem here, however, is that the cylindrical dielectric test section was designed for use with this shock tunnel prior to its upgrade and would require reinforcement to withstand the increased recoil loads of the upgraded facility. It is estimated that six 2.8" diameter steel rods would have had to be placed at 60 degree intervals around the test section to absorb the recoil load. The EM reflection from the dielectric test section and scattering from the metal rods had to be estimated.

The analyses indicated that both installations could provide a low reflection environment of better than -50 dB with the test section installation expected to be slightly better. Thus the test section installation site was selected for the L-Band tests.

Two types of absorber material were considered for the inside of the test section:

- a) broadband 8" thickness pyramidal absorber which has a reflection coefficient of -30 dB at 1 GHz and -37 dB at 3 GHz; expected reflection coefficient at 1.575 GHz is -33 dB and

- b) a 2.25" thickness laminated absorber which has a reflection coefficient of less than -20 dB above 1.3 GHz.

The laminated absorber was considered because it would be easier to install in the test section than the pyramidal absorber. It was thought possible to reduce the reflection coefficient below -20 dB by installing the absorber on canted planes. The canted planes would cause the reflected signal to be directed away from the incident angle such that more than one bounce from the absorber would occur thus reducing the reflection via a double bounce.

Analysis showed however that the reflectivity could be reduced only by about 3 to 5 dB for a source at the axis of the tunnel. This is due to the relatively large wavelength with respect to the size of the test section environment.

Based on this result it was decided that the 8" thick pyramidal absorber with a reflection coefficient of -33 dB is preferred for installation in the test section. The most stressing EM requirement is provision of a low enough reflection coefficient such that coupling measurements between antennas on the model would not be affected. An analysis for this configuration was performed.

The absorber was installed in two foot square flat panels around the inside of the test section. The distance of the panels from the antennas on the test vehicle was about three feet. Consider one of the flat panels as a large metal plate. Using image theory, the reflected signal from the metallic flat plate would be -35 dB below the transmitted signal. This would be reduced to -68 dB by the reflection coefficient of the absorber.

Around the periphery of the cylindrical test section, about one-half of the absorber panels (corresponding to a 180 degree sector) would be illuminated by the transmit antenna and the reflections from all of the panels must be added. The 180 degree sector requires 7 panels. The reflections would not all arrive in phase because of the different path lengths to the absorber. Based on a random phase assumption, the reflected power is increased by about 8.5 dB (in the worst case, all reflections arriving in phase, the reflected power is increased by 17 dB).

Thus it is expected that the coupling level between antennas caused by the absorber lined test section will be about -59.5 dB. Assuming the antenna coupling in free-space is -30 dB, a typical value, the error due to the test environment would be 29.5 dB below the expected value. This corresponds to a maximum 3.1 volt error in coupled voltage amplitude (+/- 0.3 dB error) and a maximum +/-1.7 degree phase error.

Other sources of reflection were to be anticipated from exterior walls and floor, and from the steel shock tunnel test section walls and sundry support structures. A dedicated survey of the entire experimental configuration with respect to multipath phenomena and absorber placement was therefore considered an important part of these experiment design tasks. These investigations were subsequently performed with the dielectric nozzle installed on the shock tunnel as part of the RF environmental checkout efforts discussed in Section 2.3.

2.2 Investigation Of The Electromagnetic Environment Within The Shock Tunnel

Prior to the start of the shock tunnel test program, checks of the EM environment at the location of the test vehicle were performed. The microwave absorber panels and the 3 sets of transmit horn antennas were installed in the test section interior. Each antenna set comprises 4 horns, each of 6-inch square aperture, mounted on a metal frame which is attached to the test section wall via hinges, allowing each of the antenna sets to be swung in the horizontal plane. This provides for flexibility in adjusting the pointing angle of each antenna sets' boresight so that scattering effects can be minimized. The antennas comprising each set can further be moved relative to one another to effect changes in the location of pattern nulls relative to the boresight direction.

The 8"x 24" x 24" sheets of pyramidal absorber material were glued to a number of 1/2-inch thick plywood panels, each about 2 ft x 6 ft in size. These in turn were screwed to brackets which were welded to the interior test section walls. These panels then effectively circumferentially surrounded the model location over an axial length of order 6 feet. In addition, the end of the 28 ft long test section was completely covered with microwave absorber. The checkout procedures verified that the environment was suitable for the test measurements. A sketch of the checkout arrangement is shown in Figure 1. Figure 4 shows a photograph of the absorber material installed in the shock tunnel chamber.

As indicated in Figure 5, a receiver waveguide antenna was attached to the shaft of a linear displacement transducer and moved axially along the test section centerline at the model location. Figure 6 shows a photograph of the receiver waveguide antenna. An XY plotter recorded both antenna axial position and received signal for propagation from each of the three transmit antenna locations. Many such traverses were performed following changes in both microwave absorber placement and in the pointing angle of each transmit antenna so as to define the pointing angle affording minimum evidence of scattered returns.

An illustrative record is shown in Figure 7. The feature of importance in such records is the magnitude of the peak to peak ripple. This is very small in the traces for the upstream and broadside antennas (number 1 and 2) and is < 1 dB for antenna 3 which is pointing in the upstream direction towards the nozzle exit plane with its steel end flange as a potential scattering source.

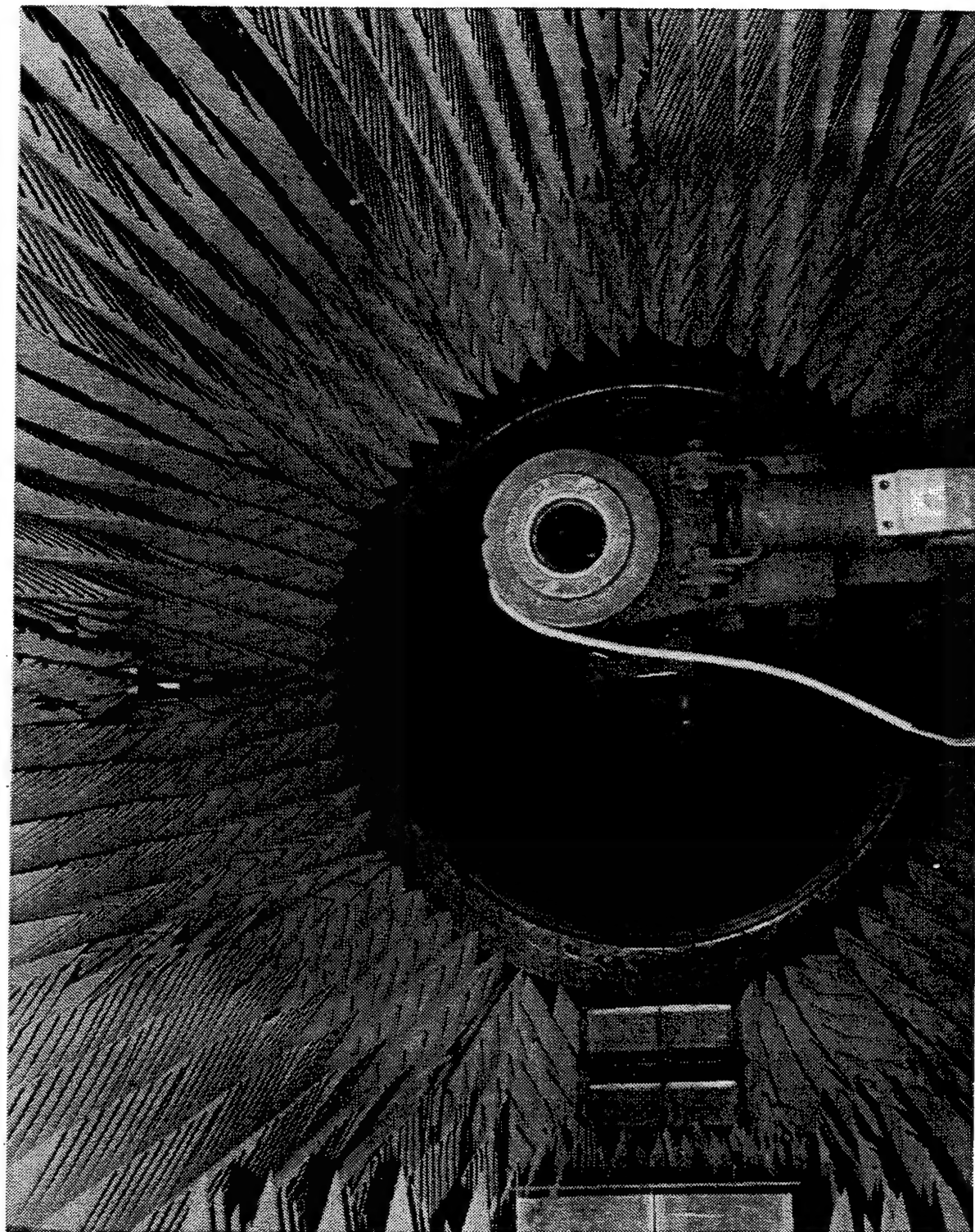


Figure 4 Photograph of the Microwave Absorber Material Installed in the Shock Tunnel Test

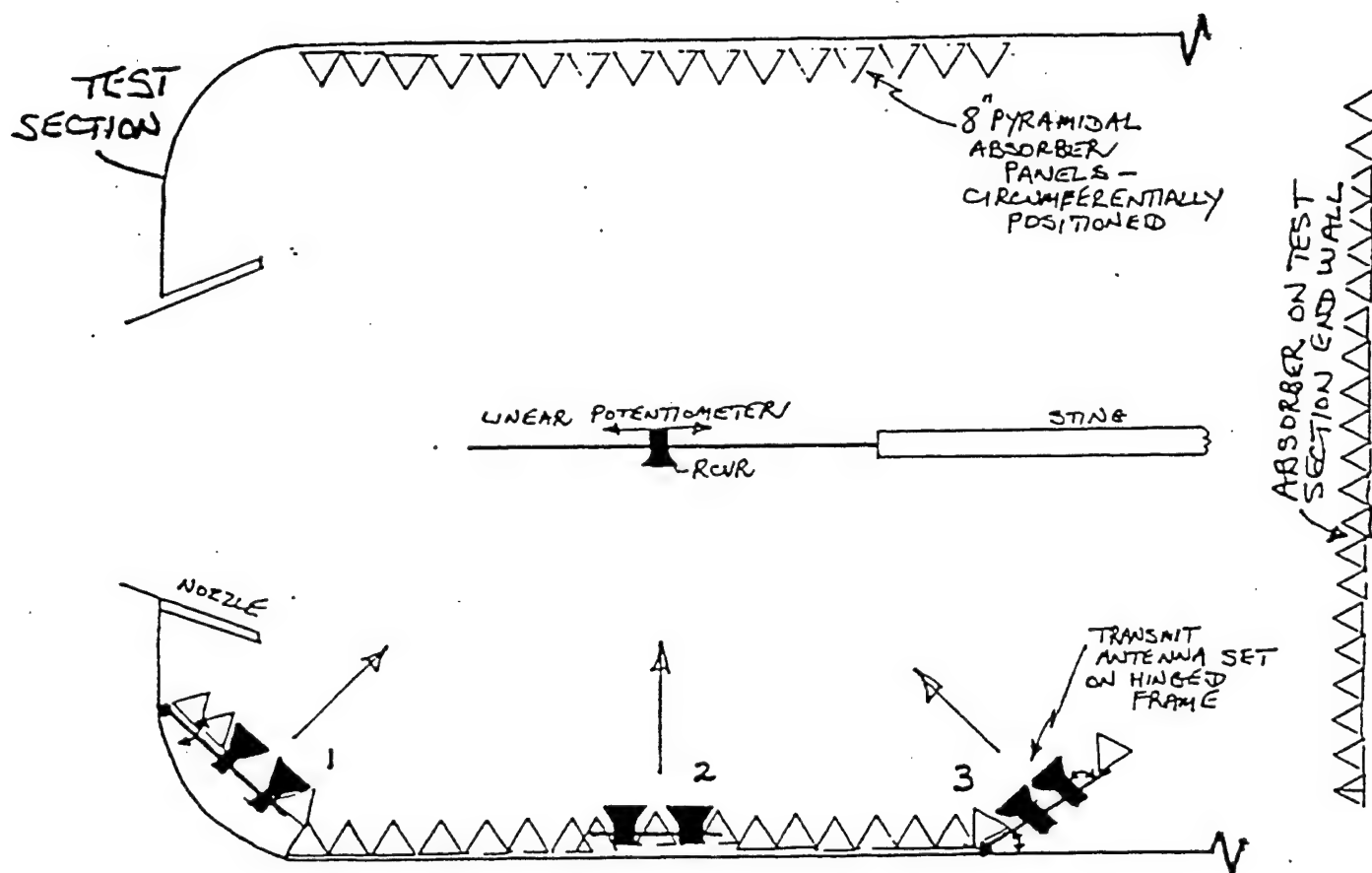


Figure 5 Sketch of the Electromagnetic Environment Test Equipment

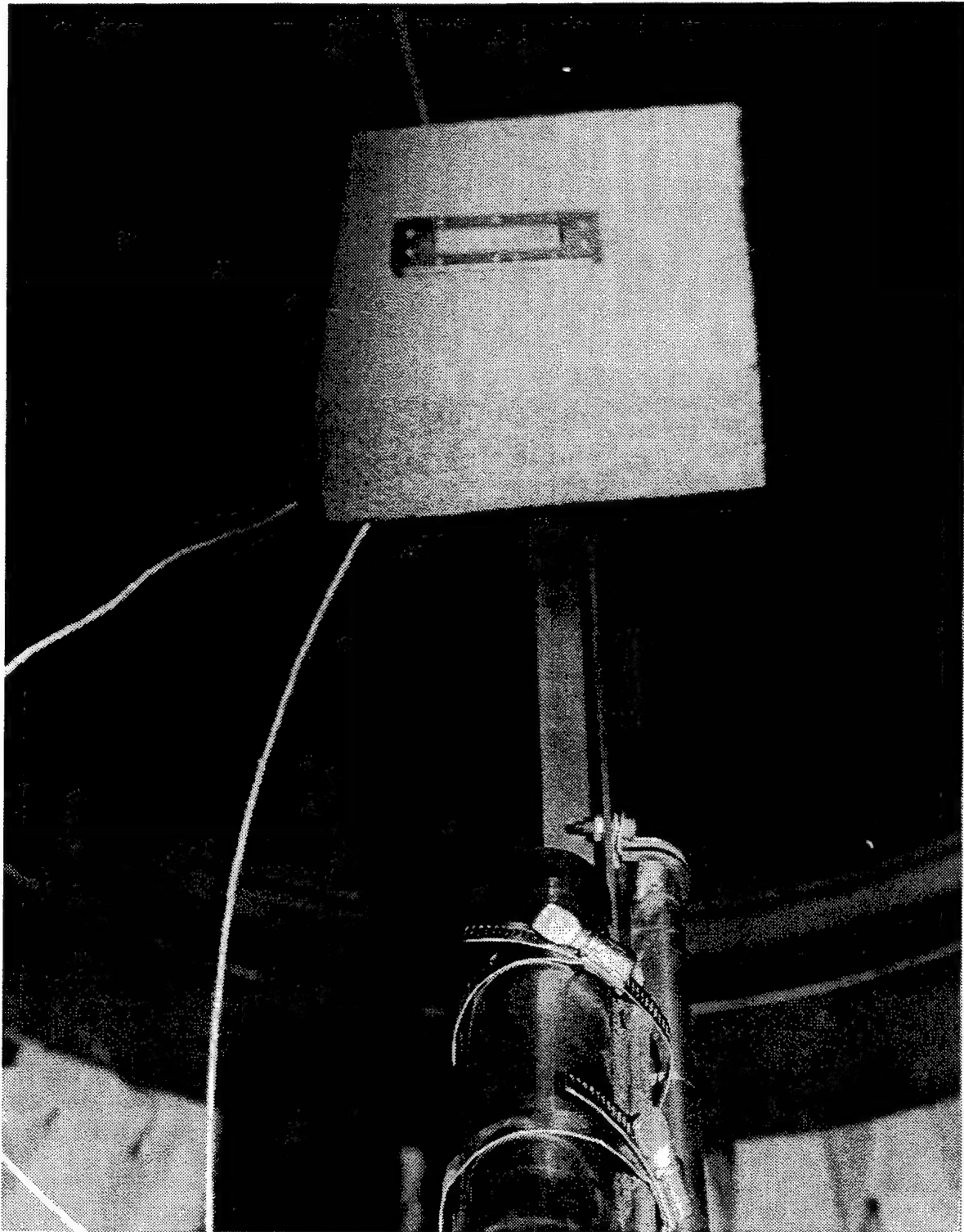
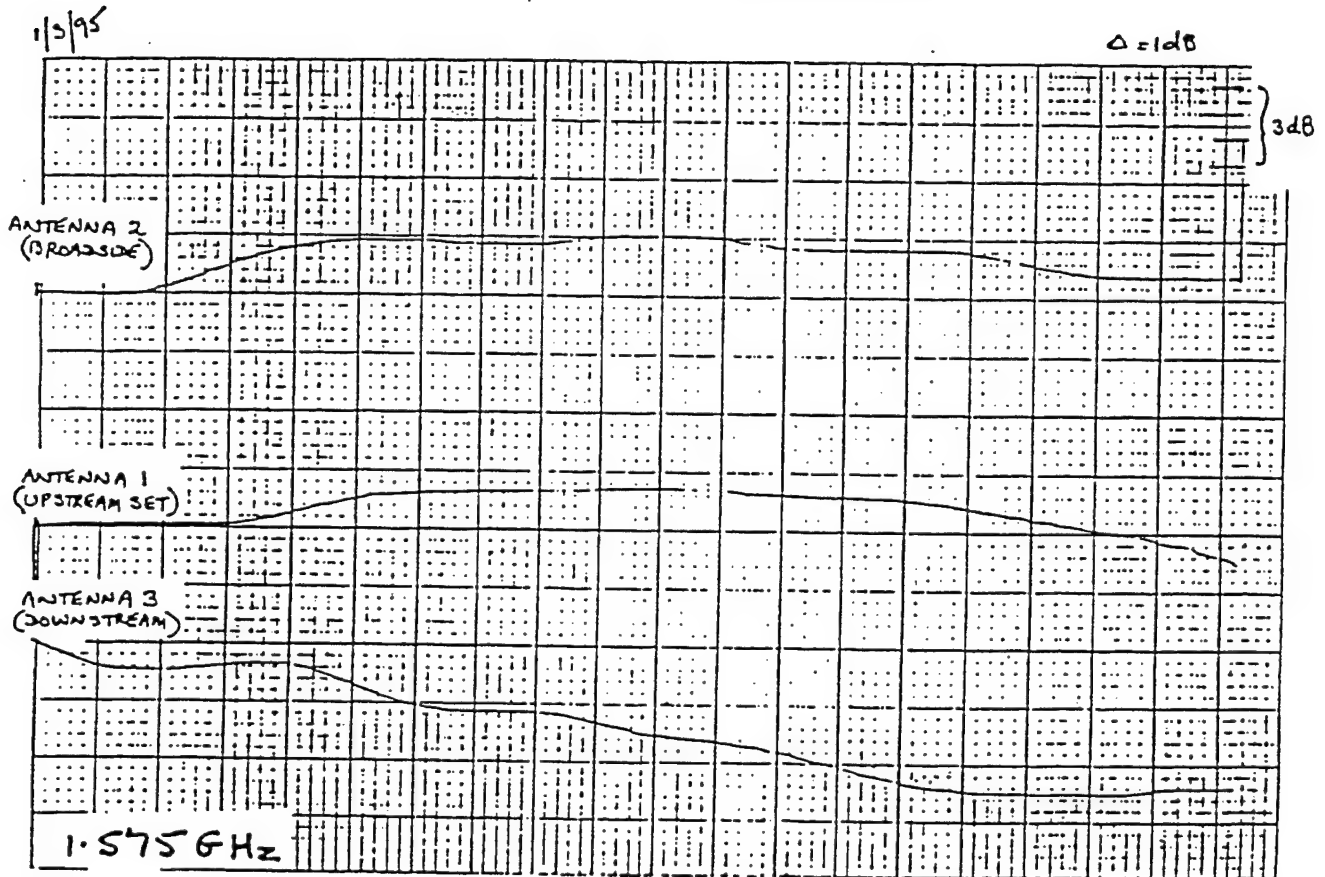


Figure 6 Photograph of the Receiver Waveguide Antenna for the EM Environment Tests



RECEIVED SIGNALS FROM WAVEGUIDE ANTENNA TRAVERSES ALONG
TEST SECTION CENTERLINE FOR EACH TRANSMIT ANTENNA LOCATION.
MINIMIZATION OF SCATTERED RETURN EFFECTS IS SATISFACTORY.

Figure 7 Illustrative Record of Received Waveguide Antenna Signal for Minimization of Scattered Return Effects

2.3 Test Model

Previous microwave-plasma interaction studies using the test model (Reference 1) were performed at both S- and X-band, at RF frequencies of 3.3 GHz and 10.4 GHz respectively, with model illumination at shallow line-of-sight angles off the nose. On the basis of blunt body flow-field analysis, the model geometry selected was a spherically-blunted cone of nose radius 1.7 inches and after body semicone angle of 7.8 degrees.

A design drawing of the model is shown in Figure 8. The overall length of the spherically-blunted cone is 36 inches, with the spherical nose readily interchangeable with a sharp conical nose for the performance of important (tare) RF measurements without the presence of a bow shock generated plasma. The base of the model was also rounded in order to minimize base scattering effects. Figure 9 shows a photograph of the model.

The model was supported in the shock tunnel test section by a specially-designed crank-angle sting which was installed in the tunnel sector mount. The sector mount is vibration-isolated from the shock tunnel and remained in the zero angle of attack position, on the tunnel centerline, throughout all the experiments. All model orientations were effected via the selection of pin placement in holes in the support sting which permitted a choice of crank angles of 2° , 6° , and 13° . The sting could be rolled within the sector mount so that the crank angle was pure pitch, pure yaw, or a combination of both. The selected angle, however, always represented the angle of attack.

2.3.1 Test Model Antenna Configuration

Five antennas had been installed on the model for the (S and X-band) test frequencies used on the previous program. The S and X-band antenna arrangements were located on opposite sides of the model. The S-band antennas were modified as described below, by loading them with dielectric, for operation at L-band (see Figure 9).

The five L-band antennas on the model are dielectrically filled open-ended waveguides, fed with a coax to waveguide transition and semi-rigid coax connected to bulkhead connectors at the base of the model. The antennas installed on the model and used on a previous program employed WR-229 waveguide which has a cutoff frequency of 2.579 GHz. The waveguides were previously filled with a low dielectric constant syntactic foam. Removal of the foam and use of a low-loss dielectric with a dielectric constant of 5 reduces the cutoff frequency to 1.153 GHz, below the test frequency of 1.575 GHz. Emerson Cumming

STYCAST HiK dielectric (dielectric constant = 5, loss tangent = 0.002) was selected for this purpose. The waveguides were filled with the HiK dielectric, installed on the model and the antenna apertures were finished flush with the surface of the conical shaped model.

The antennas on the model were oriented with their long dimensions in the circumferential direction, an orientation which provides maximum antenna beamwidth from the near nose-on to the near tail-on direction. However, this orientation also maximizes the signal resulting from scattering from the tip and base of the model. The former could be a consideration in the sharp-nose measurements. The latter should be minimal however, because of the rounded base geometry. To reduce the potential influence of tip scattering phenomena, the antenna array was located near the center of the model. [Antenna location considerations were supported for S-band operation by analyses performed by TRW⁵.]

Three of the five L-band antennas are located in a linear array extending along the length of the vehicle. The other two are placed 45 degrees away from the linear array (both plus and minus) in azimuth and at an axial plane midway between the center and aft L-band antennas, to form a cruciform arrangement (see Figures 8,9).

2.3.2 Model Instrumentation

The model was instrumented to measure both surface pressure and heat transfer rate distributions along the model surface. Plasma electron temperature and number density measurements were also made in the blunt-body flowfield using a rake of thin-wire electrostatic probes. Accelerometers were also installed within the model as an important monitor for any deleterious model movements due to tunnel-firing recoil loads or nozzle-start impact air loads on the model.

2.3.3 Surface Instrumentation

The test model had a total of 26 heat transfer gauges and 20 high frequency pressure transducers. The instrumentation locations are shown as a schematic in Figure 10. The hemispherical nose has 5 pressure stations including one at the stagnation point. The nose section also has 5 co-axial thermocouple type heat transfer gauges. The remainder of the heat transfer gauges along the surface of the test vehicle are the standard Calspan fabricated thin-film-type heat transfer gauges. The model surface also include 6 flush-mounted circular-section current-collecting probes. The probes could be used to record a characteristic similar to the thin wire probes with a swept voltage ramp, however, in this experiment a constant bias voltage was used.

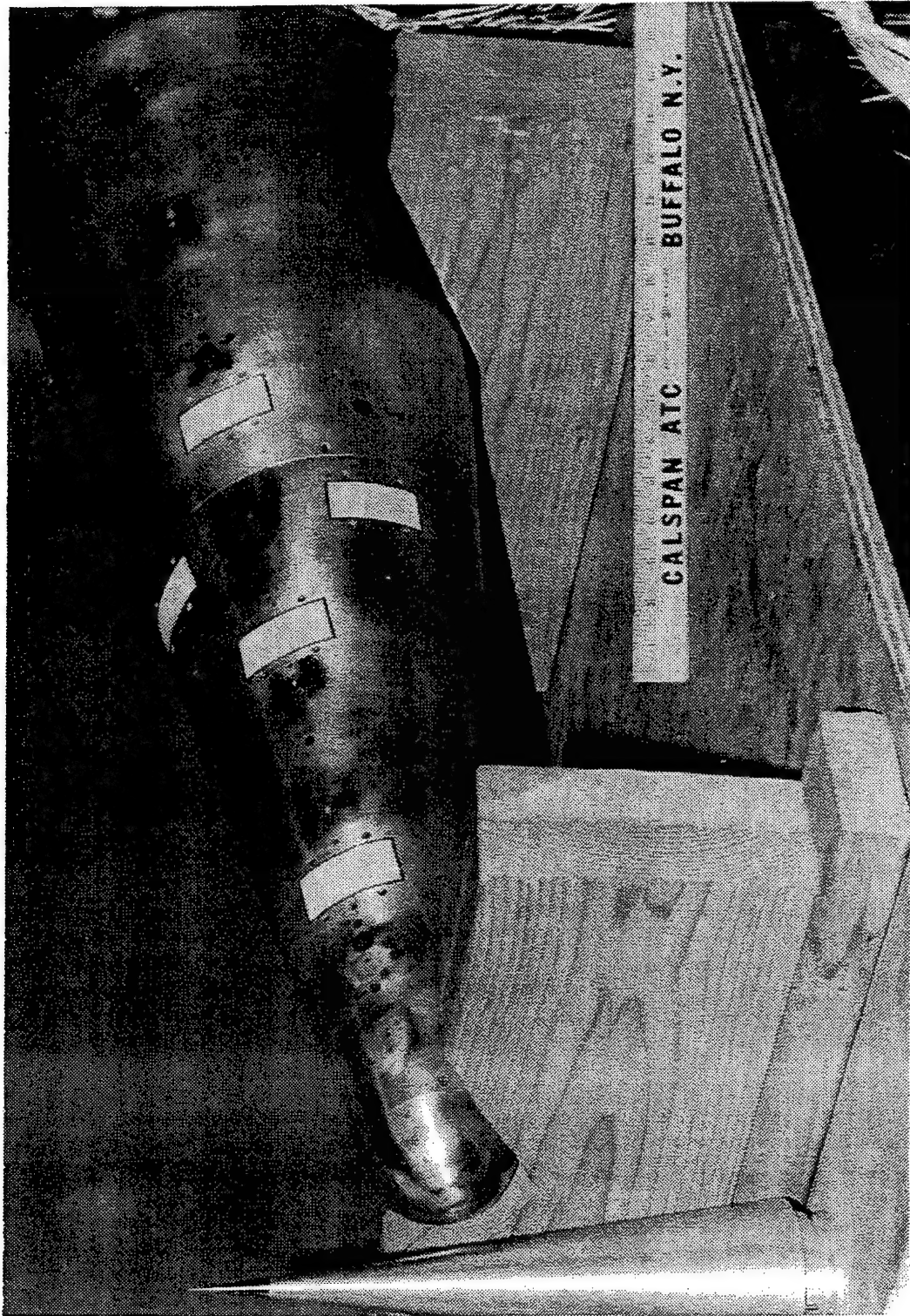


Figure 9 Photograph of the Vehicle Test Model

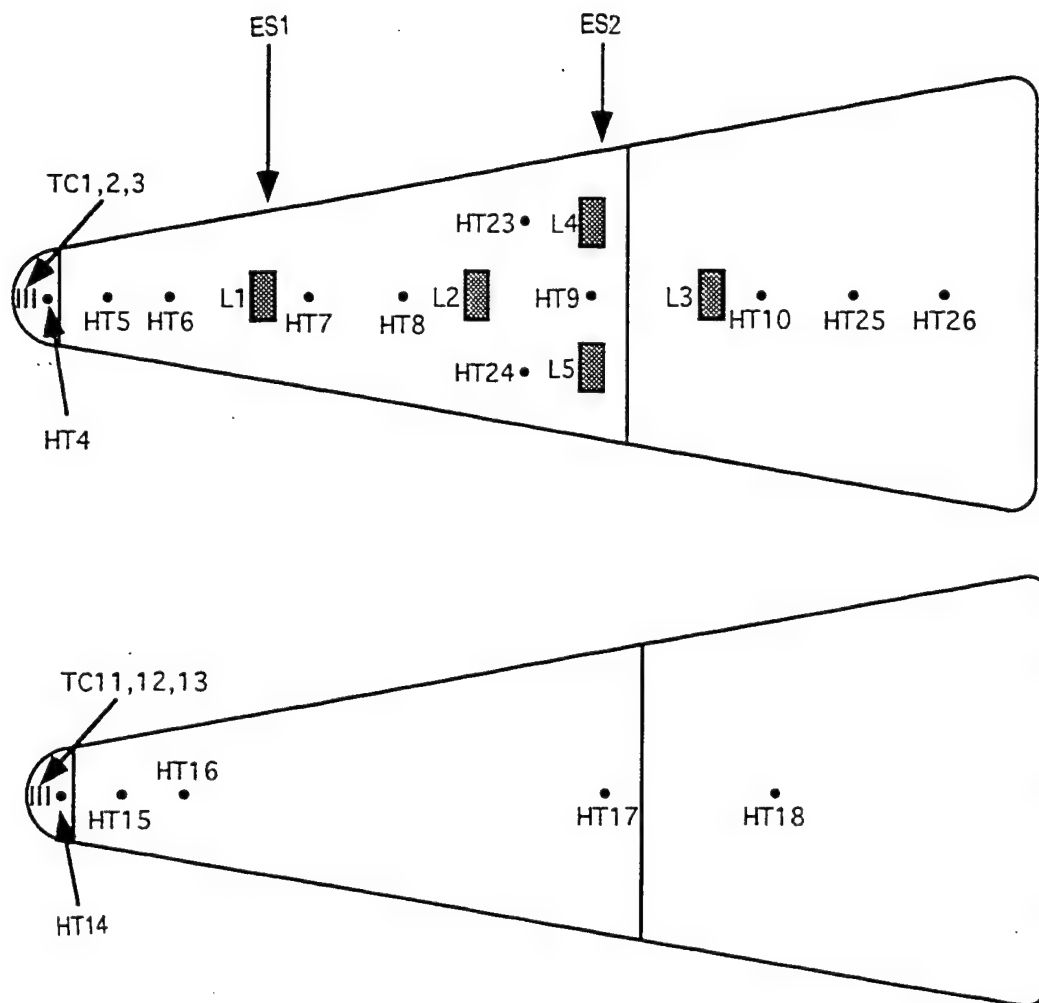


Figure 10 Schematic of the Surface Instrumentation

2.3.4 Thin Wire Electrostatic Probes

Thin wire voltage swept electrostatic probes were used to measure the electron temperature and number density in the shock layer and boundary layer regions of the test vehicle flowfield. Each probe consists of a short length of tungsten wire approximately 0.003 inches in diameter with a length to diameter ratio of approximately 80. The probes are oriented so that they are aligned with the local flow direction. In operation, the voltage applied to the probes is swept from -5 to +3 volts to record both the ion-collecting and retarding field regions of the probe characteristic. Under suitable conditions of collision frequency, the current-voltage behavior in these regions provide both the ion number density and the electron temperature, respectively. The choice of wire size affects the important ratios of probe size to electron neutral and ion neutral mean free paths which will in turn determine whether free molecular, transitional, or collisional sheath considerations will have to be invoked for the reduction of the probe data. The selection of the test conditions for this experimental research program enabled the application of the collisionless free molecular probe data reduction techniques.

A probe rake consisting of 5 probes was employed for this program. Figure 11 is a photograph of this instrument. The rake was positioned so as not to interfere with the RF measurements during a particular test run. Essentially, probe data were recorded on the opposite side of the vehicle test model from the RF interaction measurements. The probe rake was interchanged from two axial positions during the course of the testing phase of the program to provide data at a forward location, ES-1, (Antenna 1 position) and a rearward, ES-2, (mid-point of Antenna 2 and 3) location (see Figure 8).

The voltage ramp was applied simultaneously to the probes for a 100 microsecond duration four times during the test period of a particular test run which was synchronized with the steady flow conditions.

2.4 Microwave System Design

2.4.1 Antenna Design For Installation In The Shock Tunnel

Various designs were investigated for the L-band antennas which were installed inside the dump tank and which illuminated the five antennas on the model. This antenna had to provide the following characteristics:

1. horizontal polarization to match the antennas on the model,

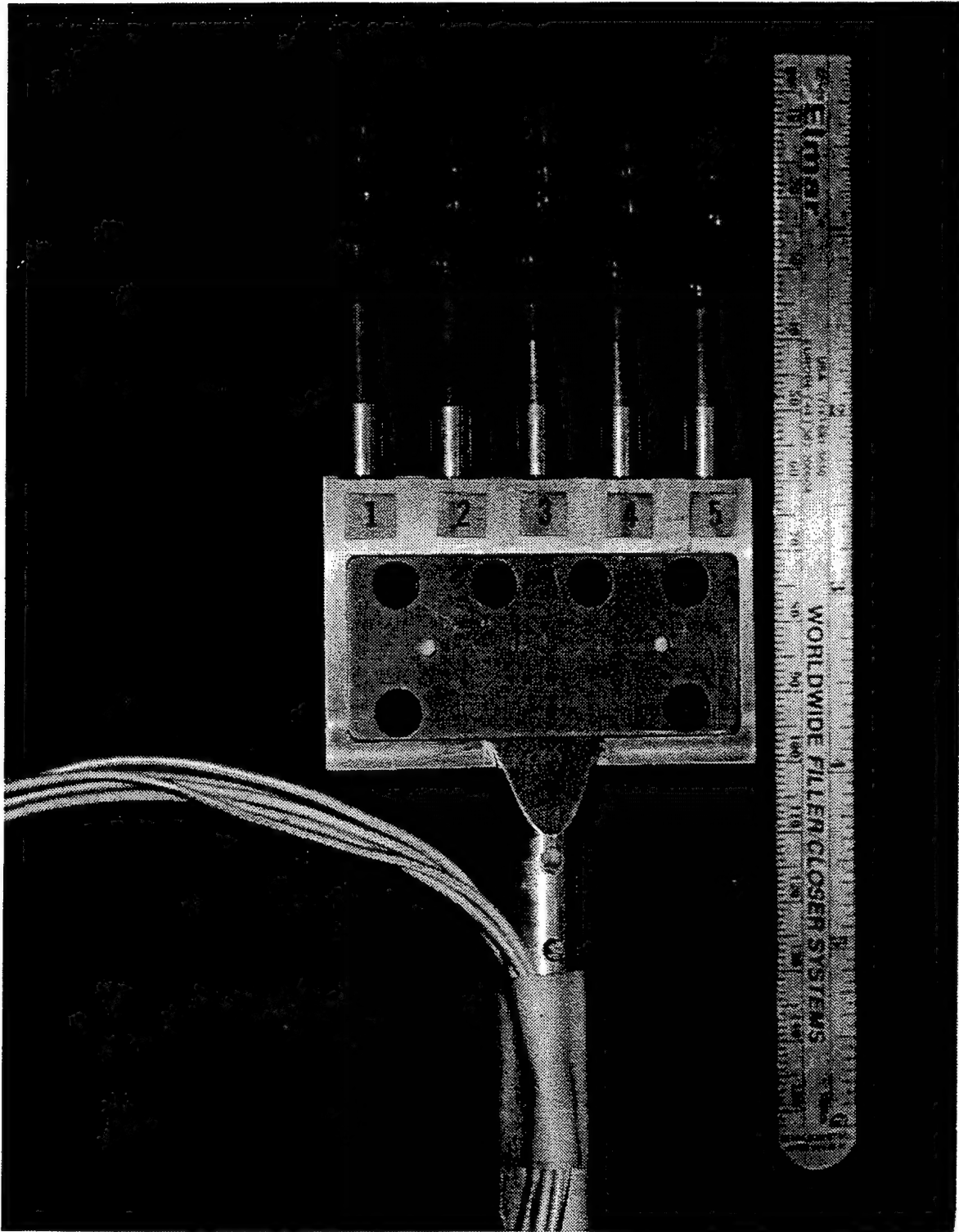


Figure 11 Photograph of the Thin-Wire Electrostatic Probe Rake

2. a length of less than about one foot such that the antenna is shielded from the shock and the reflected shock waves in the dump tank,

3. able to be located to provide a range of incidence angles to the model extending to about ± 45 degrees,

4. aperture dimension of about 1 foot to provide a far-field distance of 3.2 feet, which is about the distance from the model to the broadside antenna; beamwidth would be about 35 degrees.

In order to perform all three of the aspect angle uplink measurements during the course of a single shock tunnel test, the use of multiplexed antennas was required. The multiplexing required that the symmetry in the off-broadside aspect angles be sacrificed, i.e. it was not feasible to perform the uplink measurements without a change in the test model position. The prime advantage to the multiplexing arrangement is that all the aspect angle (and coupling) data are recorded at the same tunnel test condition. The configuration of the antennas and model inside the shock tunnel were investigated for illumination angles of 0 degrees (broadside), +37 degrees forward and -51 degrees aft with respect to broadside. The layout and number of absorber panels to be mounted on the inside of the test section was determined to minimize reflections and provide a near free-space test condition. The degree to which free-space conditions can be achieved inside the dump tank was described in Section 2.2.

There are other sources of scatter however, which could not be covered with absorber, such as the metallic nozzle exit ring which mounts to the dump tank and the sting on which the model is mounted. To minimize scattering, it is desirable to be able to place pattern nulls of the illuminating antenna at the locations of these objects. Based on configuration drawings of the components inside the test section this required a pattern null at an angle of about 22 degrees from the mainlobe. For the different configurations it was desirable to be able to adjust the null location for the specific layout.

The antenna types considered were a single pyramidal horn (with and without phase correcting lens), an endfire dielectric rod antenna and the selected antenna, which was comprised of an array of four E-plane sectoral horns. Commercially available pyramidal horns and the dielectric rod antenna were too long, in excess of two feet. A shortened horn would require a phase correcting lens in order to obtain a well formed mainlobe. It was decided that a square array of four small E-plane sectoral horns (each with a 6 x 6 inch aperture and 8 inch length) would be the smallest and easiest antenna to implement which would meet the

requirements listed above. The four horns were fed with a four way power divider. This configuration also provided the ability to adjust the location of pattern nulls relative to the mainlobe direction by changing the spacing between horns. This flexibility was useful in minimizing scattering from unshielded metallic objects in the test environment.

2.4.2 Microwave Instrumentation Data Multiplexing

The test frequency for the RF-plasma interaction experiments at L-band was 1.575 GHz. The transmit signal was switched (multiplexed), at a 10 microsecond interval, sequentially to one of the three transmitting horn assemblies, as indicated in Figure 1, located inside the test section during the normal or uplink mode and then to an antenna on the vehicle, during the coupled mode.

The data recorded during the RF measurements are indicated in Volume II of this report. During the test flow period, the plasma-induced phase shift and attenuation of the RF energy were measured at each of the five antennas on the vehicle in the uplink mode (remote transmitter #1, #2, #3 - Figure 1). The RF signal was then switched from the remote transmitter to the center active antenna on the model. In this mode, the complex reflection coefficient of this antenna was measured, in the presence of plasma, as well as the change from free space values of the amplitude and phase of the signals coupled into the other four adjacent antennas on the model. During this coupled mode of operation, the center transmitting antenna also served as the source transmitter for a microwave transmission link (called the interferometer) to horn assembly #2 located on the wall of the test section (Figure 1). The interferometer provided for near broadside LOS measurement of attenuation and phase shift during the coupling measurement period. Thus transmission data is provided (in opposite directions) between horn assembly #2 and vehicle antenna #2 during two of the four 10 microsecond data multiplex periods.

The sequenced switching from uplink to coupled modes and the RF measurement data recording was performed during a 4000 microsecond period which included the 400-500 microsec of plasma test flow over the model.

2.4.3 Microwave Instrumentation Design

A schematic of the L-band microwave system is shown in Figure 12. The connection for the microwave interferometer arrangement exercised during the coupling measurements portion of the experiment is included in the schematic. Part of the microwave

local oscillator signal was mixed with a 70 Mhz signal from a signal generator and the sum signal filtered and amplified to provide the transmit signal. The signal received on each open ended waveguide was mixed with the local oscillator signal to provide an intermediate frequency (IF) of 70 Mhz. Each IF signal was amplified and then input, along with the 70 Mhz from the signal generator, into an I/Q (In- and Quadrature-phase) detector.

Six receivers are provided for the microwave instrumentation system. These are coherent receivers providing I/Q baseband outputs which are sampled and recorded using an analog to digital recorder. The receivers are comprised of front end mixers (1.575 GHz signal input, 70 MHz IF output), 70 MHz IF amplifiers and I/Q detectors with a 70 MHz reference local oscillator input.

The mixers (1.575 GHz) and switches required for normal/coupled mode operation were assembled inside a protective cover and mounted inside the tunnel on the sting just aft of the model. IF mixer signal outputs were routed via coax to the IF amplifiers outside the tunnel.

The IF amplifiers are the same units used during the previous program and these were mounted on a plate and installed just outside the test section. The I/Q detectors, procured from Mini-Circuits, had satisfactory performance but leakage of the 70 MHz local oscillator out of the I/Q ports, as expected, required low-pass filters to be used to pass the baseband signals and attenuate the 70 MHz IF. A three-stage Butterworth filter was implemented for this purpose. The I/Q detector components were installed on circuit boards.

During the shock tunnel experiments, a check was carried out before each experiment to determine the reference values of the I and Q levels from which amplitude and phase are calculated. During the experiment, the variations of the I and Q signals are recorded and the amplitude and phase changes readily computed. It is noted that phase is only determined within 2° , hence the total phase change during the experiment may be in error by an unknown number of wavelengths. However, the relative phase change for the antennas is known.

Data were recorded by means of a LeCroy 6810 Waveform Recorder system. This unit had 16 channels with 12-bit resolution and was operated at a sampling rate of 1 MHz. Switching of the transmit signal occurred among the three horn assemblies and to the coupled mode every 10 data samples, i.e. every 10 microseconds.

3.0 MODEL ANTENNA MEASUREMENTS AND CALIBRATION PROCEDURES

In order to provide for the performance of the important antenna feed network, reflectometer and receiver calibration measurements during the experiments, special waveguide extensions in the form of saddles, reference waveguide shorts and a coax to waveguide coupler had been fabricated during a previous program (Reference 1). The saddles were machined to fit the conical curvature of the model and mate with the antenna apertures at the model surface. Because of the conical geometry, separate saddles were required for the different antenna locations on the model. For operation at L-band, the saddles, reference shorts and coax to waveguide coupler were loaded with the same dielectric as used in the antennas on the vehicle.

The saddles provided an extension to a flat waveguide flange over which reference loads or a waveguide-coax coupler could be placed for calibration purposes. Four reference shorted loads with reflection coefficients separated in phase by about 90 degrees were used to calibrate the reflectometer. After the reference waveguide loads and antenna saddles were filled with dielectric the mating surfaces were machined flush. The four reference load reflection coefficients were determined based on the lengths of the shorted sections of waveguide and the dielectric properties. The dielectric loss, providing a small correction, was included in the calculation.

Receiver calibration was performed by placing the waveguide-coax coupler over the saddles and inserting a reference microwave signal into each of the five antennas on the vehicle. Recording of the receiver output I and Q signals under this test condition provided receiver calibration. Additional calibration procedures were performed to record I/Q detector DC offsets and relative I/Q channel gain.

3.1 Antenna Measurements

Data recorded during shock tunnel tests on propagation loss, antenna reflection coefficient and mutual coupling between antennas is processed to determine these quantities referred to the antenna apertures on the surface of the model. This data processing requires calibration of the antenna feed networks, as well as calibration of the microwave instrumentation (receivers and I/Q detectors) to be performed during tunnel testing.

The reference loads and saddles were used with a network analyzer for measurement of:

a) the free-space reflection coefficients of the five antennas on the model at the aperture plane of the antennas (the S_{ii} , scattering parameters), and

b) the free-space coupling from antenna 2 (the driven antenna) to the other four antennas referred to the aperture planes of the antennas (the S_{2i} , scattering parameters).

Initial tests were performed outdoors at a location free of nearby reflectors. Later tests were performed with the model installed in the shock tunnel just prior to beginning testing in the shock tunnel. The network analyzer was placed at the coaxial connectors in the antenna feed lines at the aft end of the model. The four reference waveguide loads with saddles were placed over the antennas and the four corresponding input reflection coefficients were measured with the network analyzer. From this data, the scattering matrices of the five antenna feed networks, out to the antenna apertures, were determined. Finally, the input reflection coefficients of the five antennas was measured under free-space conditions and this data was reduced, using the antenna feed scattering matrix data, to provide the free-space antenna reflection coefficients referred to the antenna apertures on the surface of the model. If the five antenna apertures are treated as the ports of a five port network, the measured reflection coefficients are the scattering parameters, S_{ii} , of the network. Table 1 provides these scattering parameters.

TABLE 1
MEASURED ANTENNA FREE SPACE REFLECTION COEFFICIENTS
(INPUT SCATTERING PARAMETERS AT ANTENNA APERTURES)

ANTENNA SCATTERING PARAMETER	MAGNITUDE, PHASE (DEG)
S11	0.70, -163
S22	0.81, - 163
S33	0.74, -155
S44	0.87, -150
S55	0.85, -159

It is observed that the magnitude of the antenna reflection coefficient for antenna 1, which is the antenna closest to the nose of the model, is somewhat smaller than for the other antennas. This is believed to be due to the smaller radius of curvature at this antenna location. The reflection coefficients are reasonably consistent and provide a fairly tight grouping when plotted on a Smith Chart.

The coupling from antenna 2 to the other antennas was measured using the network analyzer by driving antenna 2 and measuring the signal coupled to the other antennas. Reduction of these data to the aperture planes makes use of the antenna feed network calibration data obtained during measurement of the antenna reflection coefficients. The reduced data are shown in Table 2.

TABLE 2
MEASURED FREE SPACE ANTENNA COUPLING
(INPUT SCATTERING PARAMETERS AT ANTENNA APERTURES)

ANTENNA SCATTERING PARAMETER	DB, PHASE (DEG)
Antenna 2 to Antenna 1, S21	-26.2, 17
Antenna 2 to Antenna 3, S23	-27.3, 22
Antenna 2 to Antenna 4, S24	-30.9, -133
Antenna 2 to Antenna 5, S25	-30.4, -71

The phase of the coupling coefficients from antenna 2 to antennas 4 and 5 should be the same based on symmetry of the model and the location of antennas. However, the measurement was carefully repeated after the model was installed on the sting in the tunnel test environment with exactly the same result. The source of the phase shift difference has not been resolved. The cut in the model, where it can be separated, and other instrumentation apertures were covered with metallic tape without change in the phase. Microwave absorber was placed over the nose and tail region on the model ruling out reflection from these regions.

It may be that the difference in phase of the coupling coefficient is due to a difference in the metal-to-metal contact of antennas 4 and 5 to the model surface. The waveguide aperture is quite reactive and a difference of this type could affect the way EM surface waves are launched around the conical model surface.

3.2 Calibration Of Microwave Instrumentation

The calibration of the microwave instrumentation made use of the procedures and computer programs developed for a previous program (Reference 1). This procedure did not require the disassembly of the instrumentation at the bulkhead connectors at the aft end of the model and provided a direct means of translating the measured run data to the antenna aperture planes.

3.2.1 Measurement of Antenna Aperture/Mixer Reflection Coefficients

These measurements provided the reflection coefficients looking into the antenna apertures towards the mixers. In the normal (uplink) mode, the reflection coefficient of the five antennas was measured. In the coupled mode, the reflection coefficient of antenna 2 was measured. The necessary instrumentation was located inside the tunnel test section so that the coax-waveguide (coax/WG) adapter could be positioned over any of the five antennas.

The network analyzer was calibrated by placing the reference waveguide loads over the coax/WG adapter and recording the network analyzer output (i.e. dB and degrees), having adjusted the analyzer for 0 dB and 0 degrees with waveguide load #1 (brass shorting plate). This short reading was rechecked at the completion of the reference waveguide load measurements, and the network analyzer calibration was repeated if the short reading had changed.

In normal mode, the saddle and coax/WG adapter was placed over antenna 1, ensuring that all components mated accurately without air gaps, and the network analyzer readings were recorded. This procedure was repeated on all of the other four antennas, rechecking the network analyzer reading for 0 dB, 0 degrees with the reference short over the coax/WG adapter between each antenna measurement. Also, while performing the measurement on antenna 2, the network analyzer reading was also recorded for the system placed in the coupled mode.

3.2.2 Measurement of I/Q Channel Relative Gain

The measurement of the relative gain of the in-phase (I) and quadrature-phase (Q) channels of the antenna and interferometer receivers was performed at the digital outputs. The I channel gain was taken as unity and the gain of the Q channel was determined via processing of the recorded digital data.

A second 70 MHz source was employed for these measurements. In normal mode, monitoring one of the phase detector outputs, the frequency of the second 70 MHz source was adjusted to provide a frequency output between 1 KHz to 7 KHz. The 10 channels connected to the five antennas were then recorded, verifying that at least three full sine waves were recorded. In coupled mode, the channels connected to the interferometers were also recorded, for three or more full sine waves. After processing the sine wave data, the gain of the Q channel relative to the I channel was determined. The gain of the I channel is unity.

3.2.3 Receiver Calibration

The receiver calibration was performed from the antenna apertures on the model to the digital outputs. A reference signal was input into the five antennas and receivers on the model.

The calibration instrumentation was configured especially for these measurements. With the saddle over antenna 1 and the coax/WG adapter over the saddle, the I and Q channels of antenna 1 were recorded. These data recordings were repeated for antennas 2 to 5.

In the processing of the receiver calibration I and Q data for antennas 1 through 5 and the interferometer I and Q data, the channel DC offsets (recorded with zero input signal) were subtracted from the averaged data. The Q-channel average was then multiplied by the appropriate Q-channel gain and the complex receiver calibration numbers were then formed.

3.2.4 Reflectometer Calibration

The reflectometer was calibrated from the antenna 2 aperture to the digital outputs of receiver 2. The calibration instrumentation was again especially configured for these measurements. The antenna 2 saddle was placed over the antenna 2 aperture, the reference waveguide load #1 (shorting plate) then held over the saddle, and a digital sample recorded of the receiver 2 I and Q channels. This procedure was repeated for the reference waveguide loads #2 to #4, with the digital channels transferred to the computer at each step. Finally, the saddle was removed from the antenna 2 aperture, the area around the model cleared, and the antenna 2 free-space reflection coefficient was measured by recording the antenna 2 I and Q channels.

Again, throughout all of these calibration procedures, in the affixing of saddles, reference waveguide loads and the coax/WG adapter it was essential to ensure that all components mated accurately without air gaps.

4.0

NUMERICAL ANALYSIS OF THE MODEL FLOWFIELD

In order to assess the flowfield appropriate to study in a high enthalpy airflow experiment, computations of both the nozzle expansion which generates the test stream, and the flowfield around the model are required. The non-equilibrium effects in the nozzle expansion and the shock-induced effects around the test vehicle are important. Simulating flight conditions at high Mach numbers, such as those used in these experiments, requires a shock tube reservoir condition in which the air is significantly dissociated and ionized. This requires a description of the flow physics from reservoir to test model which would include the effects of the non-equilibrium nozzle expansion, processing of the airflow through the bow shock ahead of the test vehicle and also the expansion back around the conical afterbody of the test vehicle. Figure 13 shows a sketch of the important regions for the computations.

Nozzle flow computations were completed in an effort to generate flow conditions consistent with a high altitude laminar flow simulation. The primary requirement was that these flow conditions be sufficient to generate ionization levels in the test vehicle flow which would be consistent with the measurement of RF interaction effects at L-band. Additionally, the electron number density measurements by use of thin-wire electrostatic probes in the afterbody flowfield dictated a minimum density altitude for the experiment for which the thin-wire probes could be operated under a collisionless sheath condition.

Operation of a shock tube with an incident Mach number of near 9.0 into air at near 1 atm will generate a reflected shock temperature of 6000 K at a reflected shock pressure of 500 atm. This gasdynamic state is the reservoir condition from which the non-equilibrium nozzle expansion generates the freestream. The air in the reservoir is dissociated and partially ionized which requires recombination kinetics for the computation of the non-isentropic expansion through the nozzle. The Calspan contoured D-nozzle was used for these experiments. It has an overall length of 20 ft. and an exit plane diameter of 48 inches. A nozzle throat diameter of 0.964 inches was used to perform the nozzle calculations and for the experiment. The calculations of the nozzle expansion assumed thermodynamic equilibrium for the vibrational and electronic degrees of freedom with the translational temperature while the coupled chemical reactions proceeded with finite rates.

The shock tunnel operating condition selected for the conduct of this experimental research program provide a reservoir condition at approximately 10 MJ/kg enthalpy level which provides a freestream velocity near 4.2 km/sec (14,000 ft/sec) at 42.5 km (140 kft) simulated altitude. This condition provided a sufficiently rarefied condition in order to

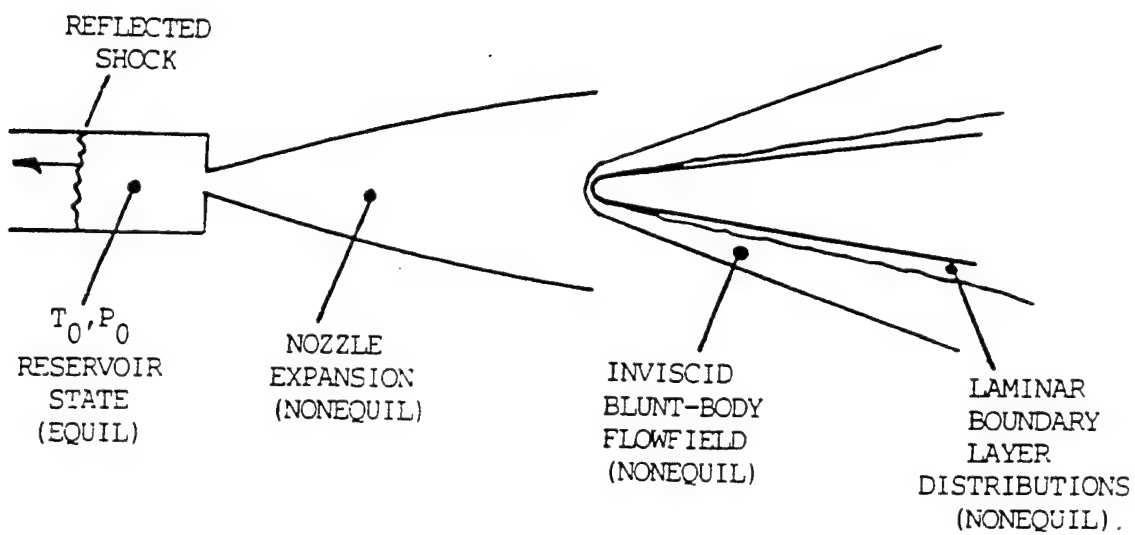


Figure 13 Sketch of the Important Flowfield Regions for the Computations

operate the thin wire-electrostatic probes using data reduction techniques assuming a collisionless sheath approximation. Figure 14 illustrates the species composition through the nozzle expansion in the D-nozzle for the test condition. The equilibrium solution is included for reference. The species concentrations are reported in mass concentration values, moles/gram, which removes the dependence on density from the distribution and also illustrates more clearly the departure from equilibrium for the expansion and also the freezing process of the chemical composition. It is clear that while all of the dissociated nitrogen recombines in the expansion, NO and O are seen to freeze out early in the expansion process (because of the fast shuffle reactions involving nitric oxide).

The bluntbody model flowfield computations exercised in support of a previous program (Ref. 1) comprised both an inviscid flowfield calculation for the gasdynamics and chemistry, matched to a non-equilibrium laminar boundary layer calculation to extend the prescribed inviscid code parameter values to the blunt cone surface. The inviscid numerical calculation involved an inverse method solution for the subsonic-transonic flow region, and a modification of the method of characteristics for the supersonic region. The displacement effect of an ideal gas boundary layer was also incorporated in both the subsonic and supersonic flow region calculations.

This Calspan-developed code (circa 1967) is referred to as the Cuniflow code. The input conditions for the Cuniflow blunt body flowfield computations were the non-equilibrium tunnel freestream flow variables calculated from a non-equilibrium nozzle expansion code also of Calspan origins. This code describes the coupled gasdynamic and finite-rate chemical processes in the nozzle expansion from the reflected shock reservoir conditions.

Current CFD capability at Calspan has been enhanced to include the implementation of the GASP (General Aerodynamic Simulation Program) from Aerosoft, Inc., Blacksburg VA. The following discussion on flowfield conditions were obtained with the GASP code. GASP is a fully conservative cell-centered finite-volume Navier-Stokes solver. A series of solutions were obtained for an axisymmetric slice of the blunt cone body shape with the stagnation streamline being considered as a singular axis. The conic afterbody was modeled as far back as to encompass the locations of all five of the model-bound antennas. The freestream was also specified, as with the Cuniflow calculations, with the stream variables as computed from the quasi-1D non-equilibrium nozzle expansion code. Solutions were obtained for equilibrated internal modes but with finite rate chemistry. The freestream Reynolds number of 550,000 per meter enabled the laminar viscous flux modeling.

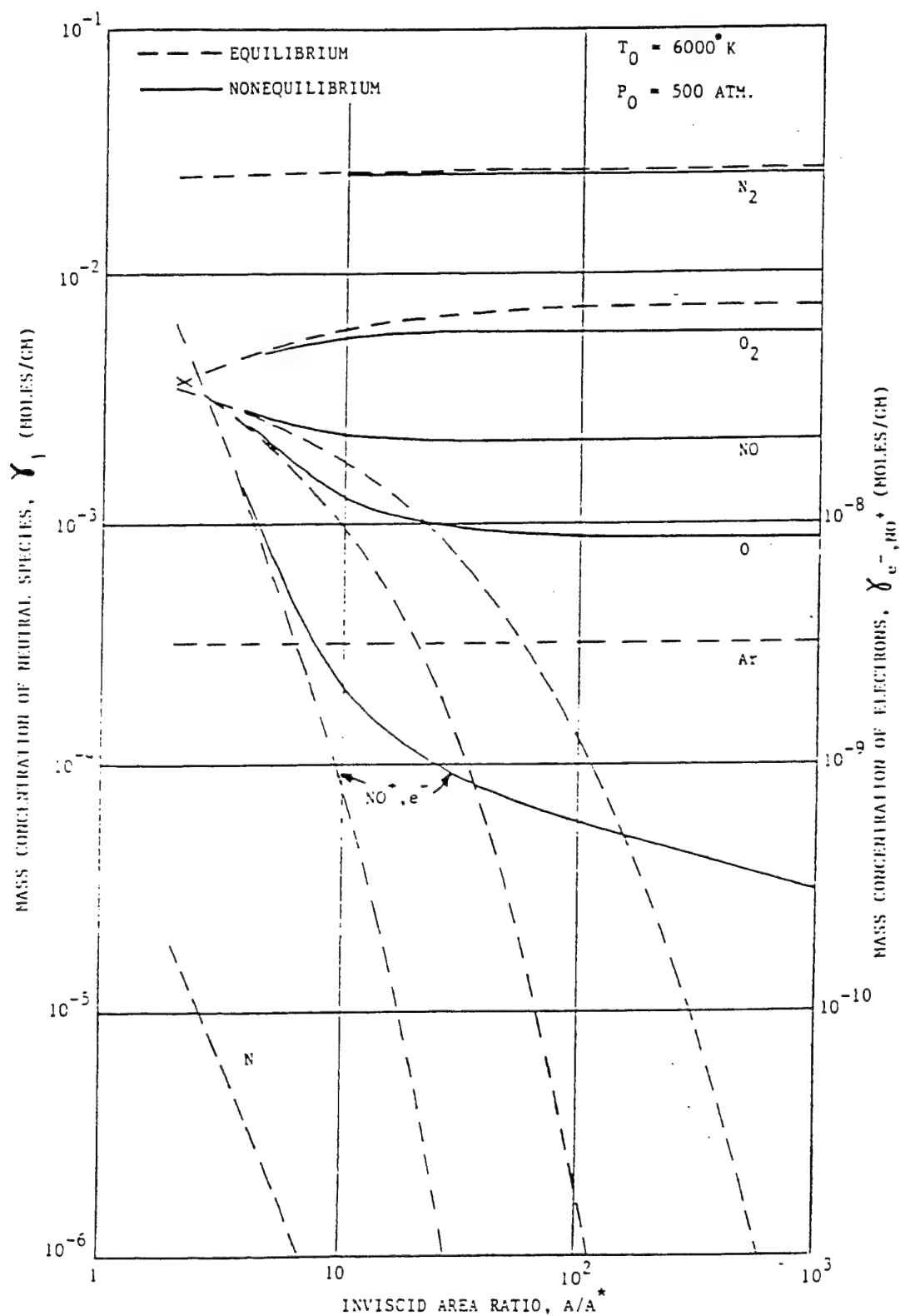


Figure 14 Species Distribution for Airflow Expansion in Hypersonic Nozzle

Comparisons between the Navier-Stokes solutions and the Cuniflow code have been conducted. Navier-Stokes calculations have been conducted with two different kinetics models for comparison. The shock tunnel operating conditions planned for the measurements program would provide a nominal reservoir state of $T_0 = 6000$ K and $P_0 = 500$ atm with expansion from the reservoir state through a nozzle throat diameter of $d^* = 0.964$ inches. These conditions provided a freestream velocity of 13850 ft/sec at an equivalent density altitude of about 140 kft.

This test condition is compatible with the use of swept voltage electrostatic probes for the quantitative measurement of the local plasma conditions in the flowfield. This plasma state should also provide significant interaction effects at L-Band.

The calculated freestream conditions at the nozzle exit plane are :

$$T = 510 \text{ K}$$

$$\rho = 2.9 \times 10^{-6} \text{ gm/cm}^3$$

$$P = 0.06 \text{ psia}$$

$$U = 13,850 \text{ ft/sec}$$

$$M = 9.34$$

Together with the non-equilibrium freestream gas composition, these variables provided the input for the GASP calculation of the body flowfield at zero angle-of-attack for the test vehicle geometry. The Calspan revised kinetics model was used for the calculations, however a small study was conducted using a model developed by Park (in the GASP code library) as well. This study established the Calspan revised model as an appropriate model, however some of the computations employing the Park model are include in the Figures.

The calculated flowfield parameter values are show in Figures 15 through 17. These include profiles at the antenna 1, 2, and 3 locations which are the three in-line antennas. It can be seen that the Cuniflow computation is in agreement with the Navier-Stokes solutions. Additionally, the Park kinetics model makes little difference when compared with the Calspan Model. Figure 18 shows the computed species mole fractions for the L1 position, which is a location over the forward most antenna approximately 7.8 inches from the nose of the test vehicle along the surface. The last Figure in this section, Figure 19 shows the calculated surface pressure and heat transfer predictions. In the next section it can be seen that these are in good agreement with the measured pressure and surface heat transfer distributions along the surface of the test vehicle.

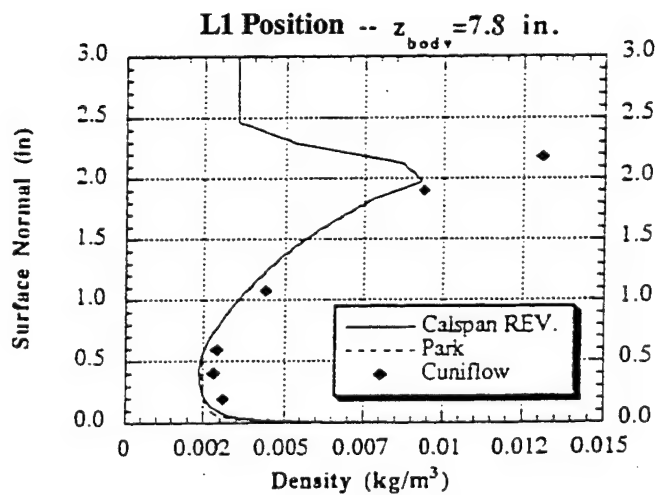
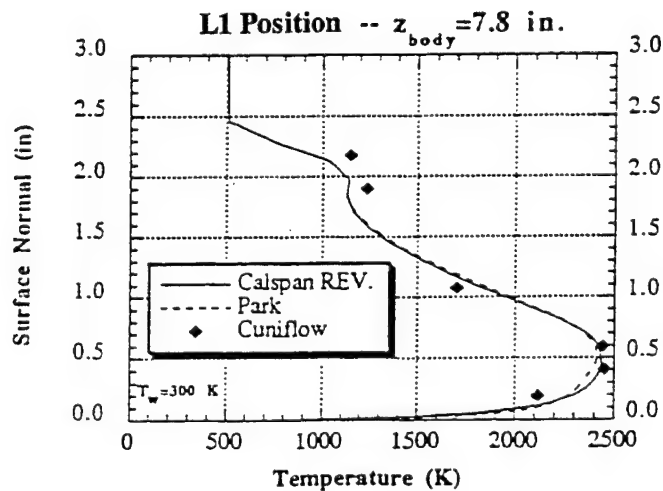
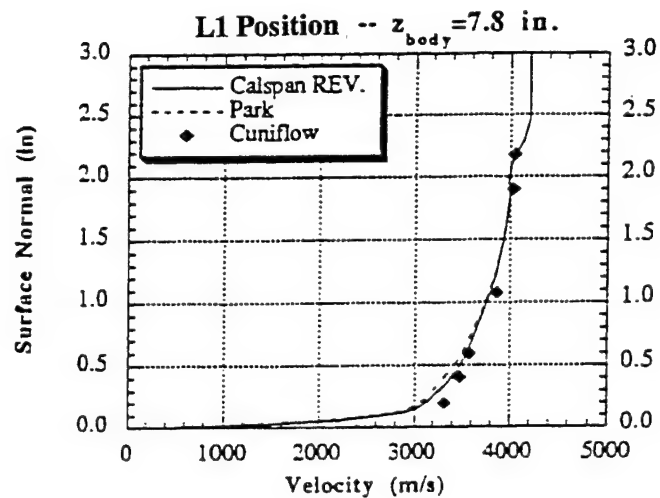
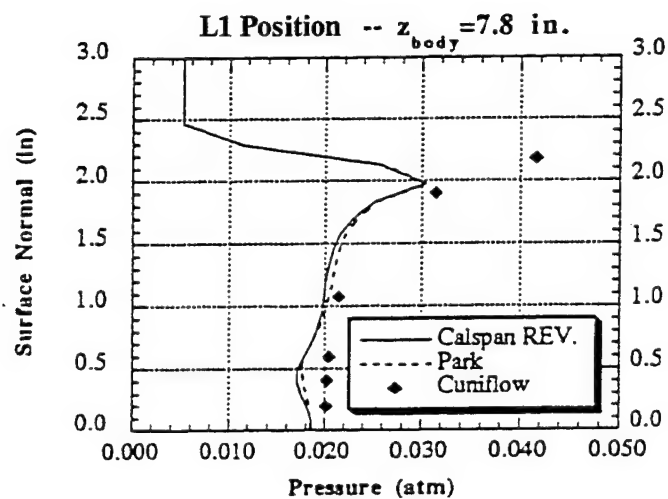


Figure 15 Flowfield Gasdynamic Parameter Distributions Normal to the L1 Antenna Aperture

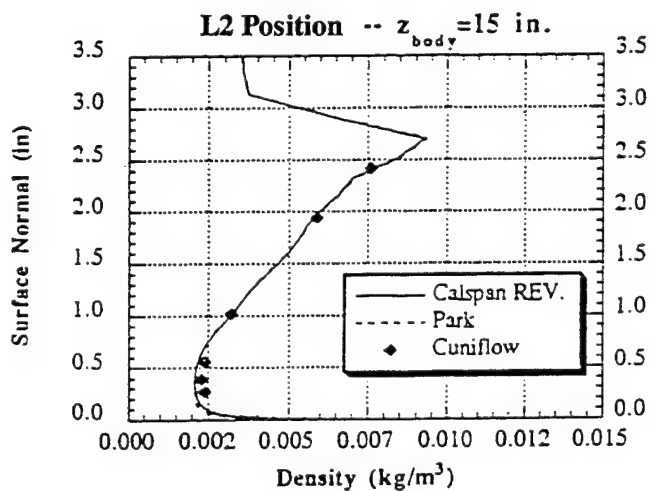
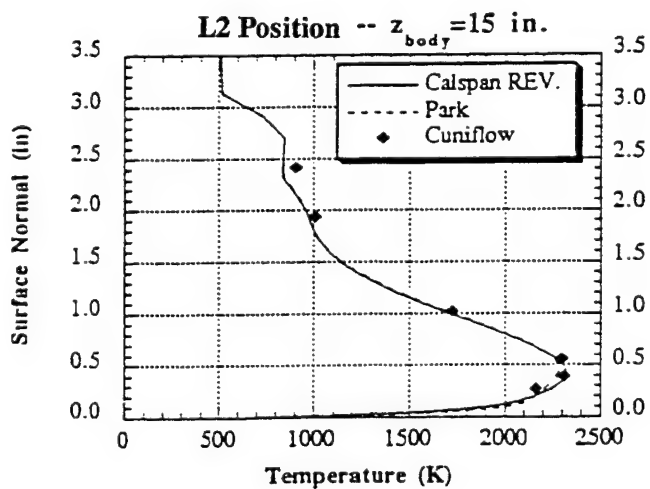
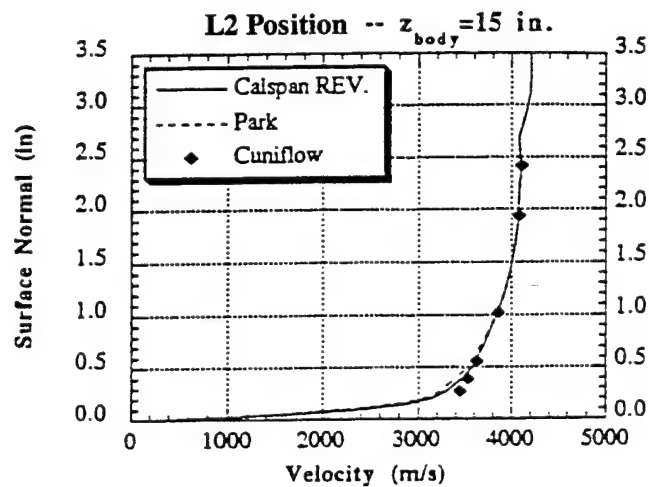
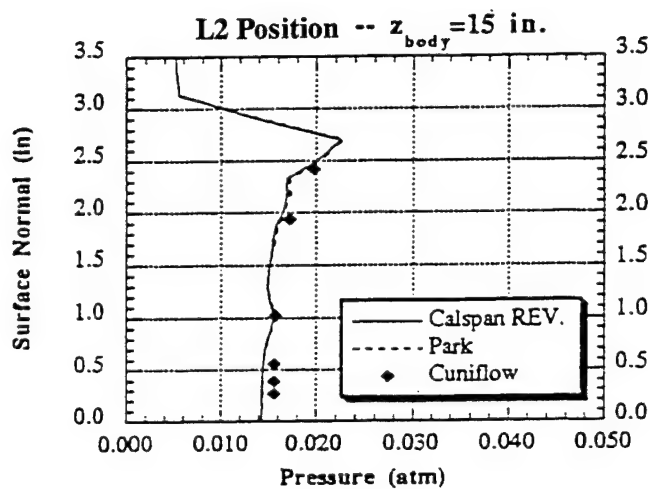


Figure 16 Flowfield Gasdynamic Parameter Distributions Normal to the L2 Antenna Aperture

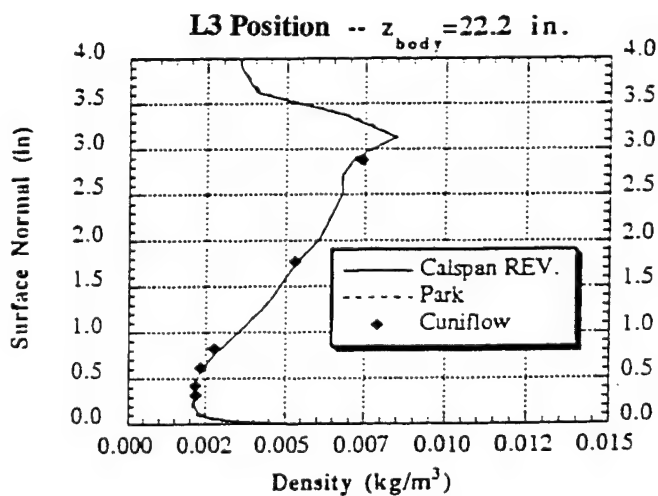
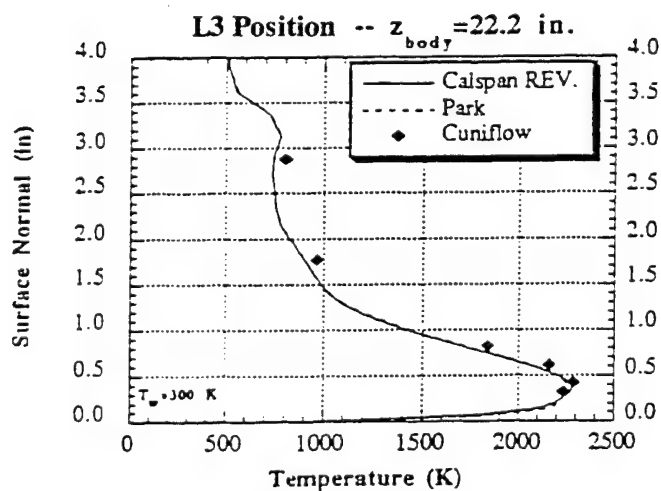
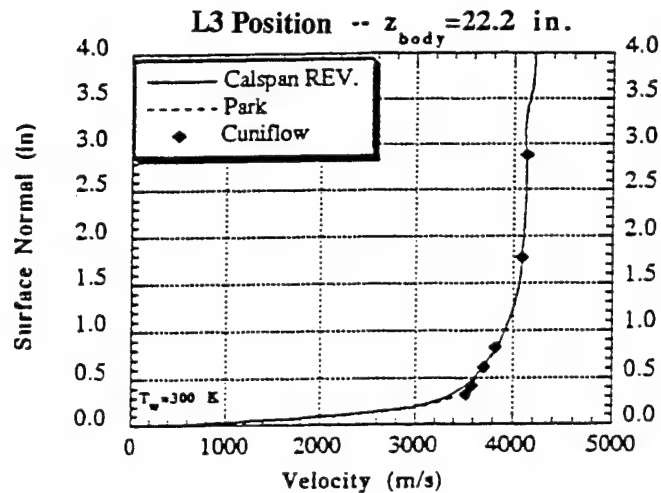
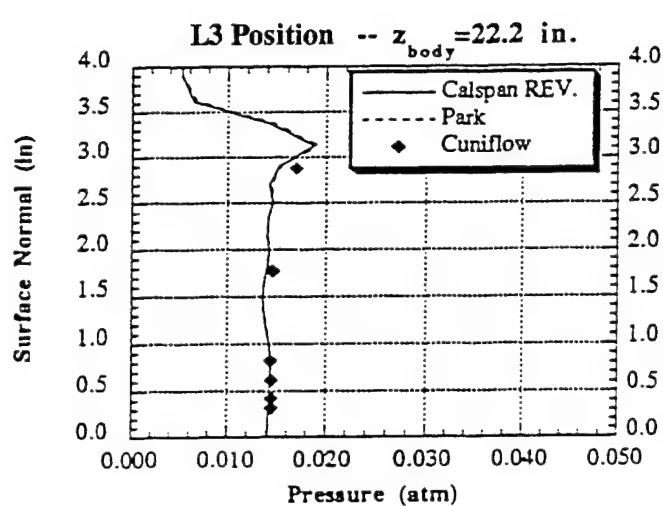


Figure 17 Flowfield Gasdynamic Parameter Distributions Normal to the L3 Antenna Aperture

L1 Position -- $z_{\text{body}} = 7.8$ in.
 Calspan Revised Chemistry

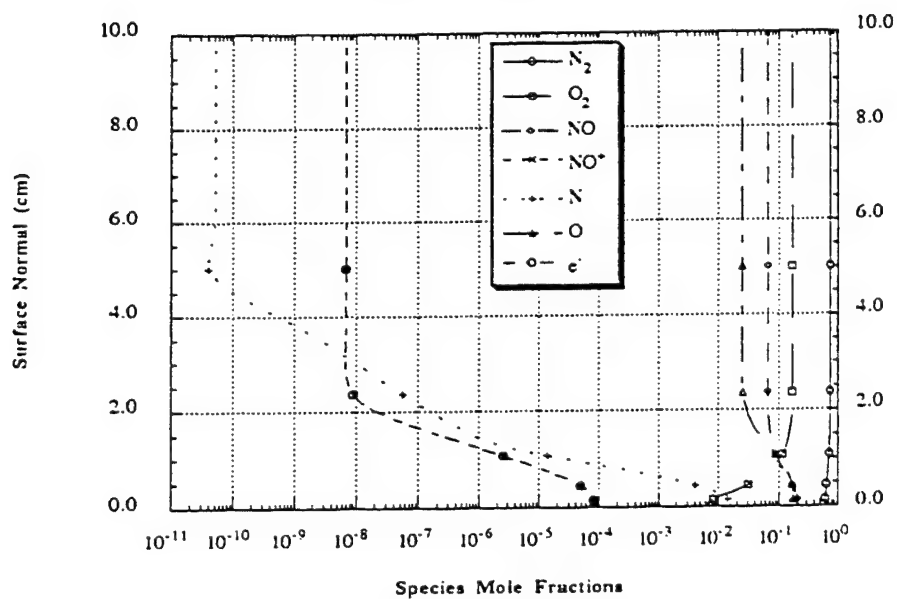


Figure 18 Flowfield Species Mole Fraction Distributions Normal to Antenna 1, L1 Aperture

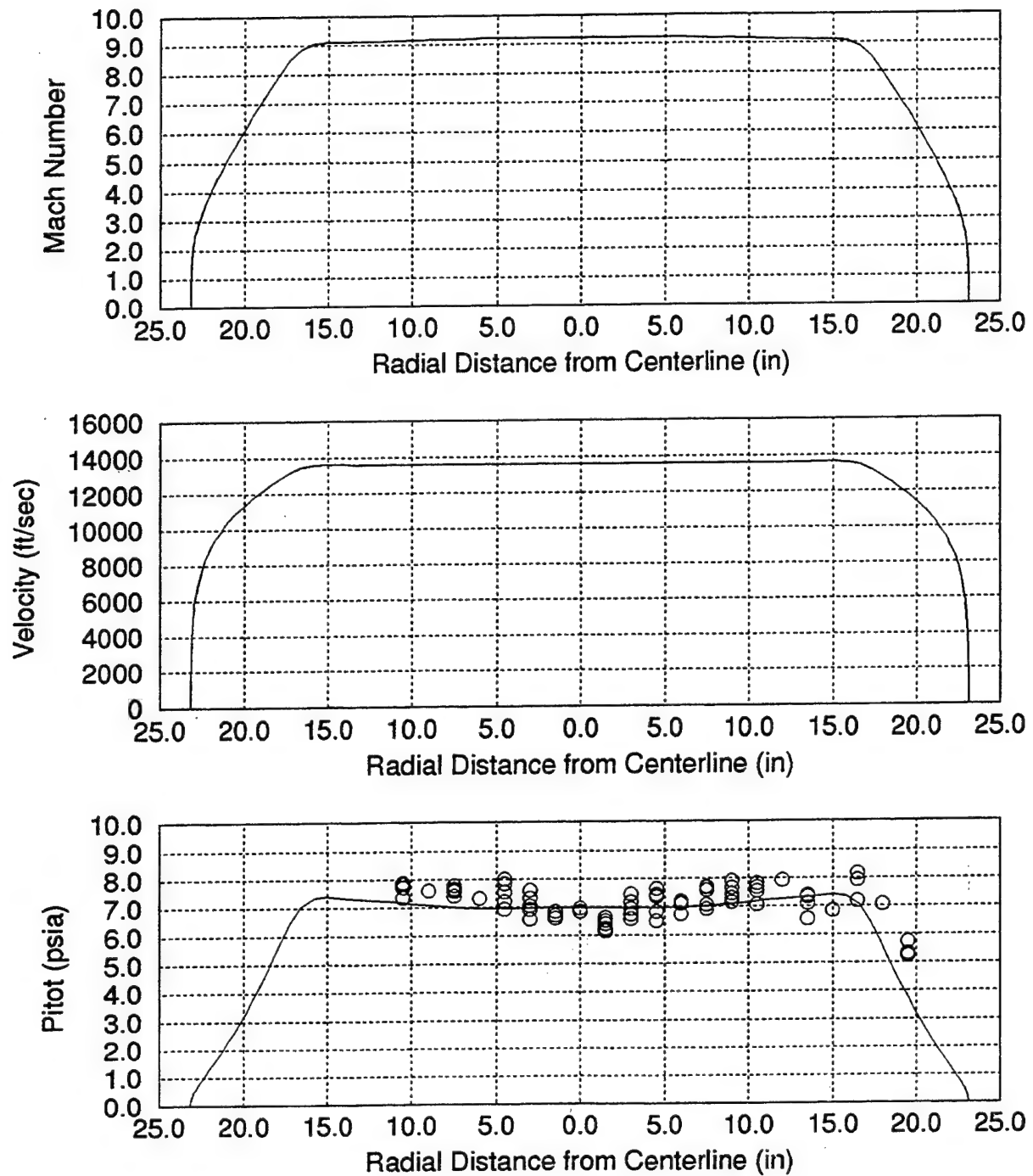


Figure 19 Freestream Flowfield Pitot Measurements with Navier-Stokes Prediction

5.0

RESULTS

The entire program employed the same test vehicle which was described in detail in Section 2.0. A photograph of this test model is shown in Figure 9. A total of 33 test runs were made in the shock tunnel test program. The matrix is shown in Figure 18. The matrix includes variation of angle of attack with several combinations of pitch and yaw. Also, included was a single test with a sharp nose to give a baseline for the absence of significant RF interaction effects due to the finite plasma component of the non-equilibrium freestream. Four basic types of measurements systems were employed. The first and largest is the RF system which includes uplink from three lines-of-sight to the five model antennas, mutual coupling from Antenna 2 on the model to the other four vehicle bound antennas, and a line-of-sight interferometer from Antenna 2 on the vehicle to the broadside tunnel wall-mounted antenna. This system is described in detail in Section 2.0. The second major measurement system included the thin-wire electrostatic probe rakes and surface mounted electrostatic probes. The electrostatic probes consisted of a 5-probe rake used to measure electron number densities at the forward and mid-way between the center and aft antenna locations. Additionally, a three probe rake was located in the aft-wake region of the model flow. These rakes are shown in the photograph in Figure 8. A suite of aerothermal surface instrumentation was located along a ray extending from the nose of the model to the rear antenna location. These instruments included 20 pressure transducers and an array of co-axial and thin-film heat transfer gauges. Fourth, the radiation in the blunt-nose region of the hemispherical nose was measured radiometrically and spectrally with an (OMA) optical multi-channel analyzer. The results from this later set of data are presented in Appendix D of this report.

5.1

Test Stream Diagnostics and Condition

In addition to the test matrix described above, a series of airflow tests were conducted to describe the freestream quantities and quality. Figure 20 is a photograph of a highly instrumented rake which was used for these tests. The rake instrumentation included: stagnation heat transfer probes, Pitot pressure probes, 3" diameter hemisphere probes with heat transfer gages on the surface, radiation measurements from the hemisphere probes, and a line-of-sight laser-diode water absorption experiment in order to determine arrival of driver gas. In addition to the airflow series, a Navier-Stokes computation of the nozzle expansion was calculated from the reservoir (driven tube) to the freestream core flow. These results are plotted with Pitot pressure values from several of the airflow tests in Figure 21. Repeatability of the test point is considered to be quite good as can be seen from these measurements of the Pitot

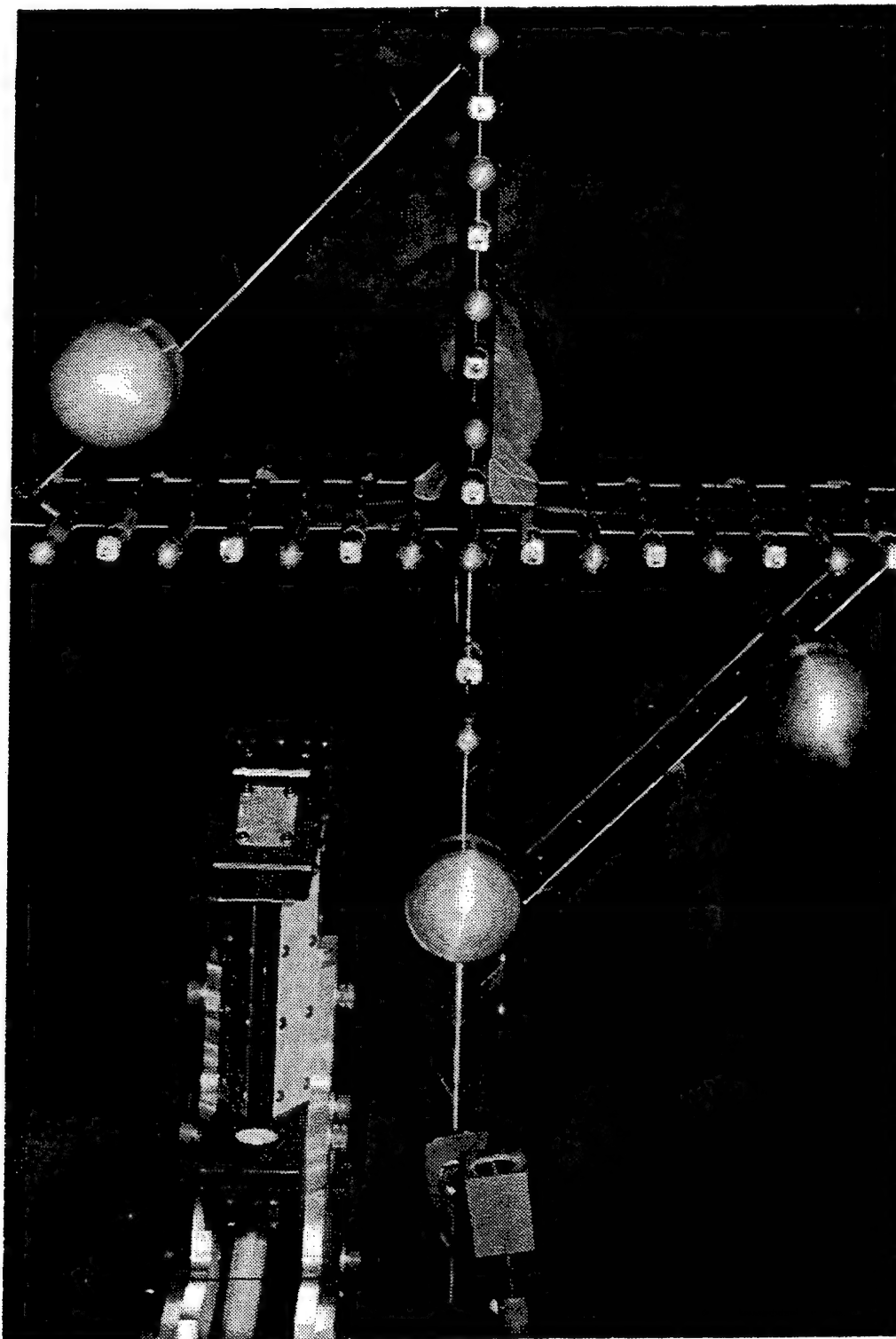


Figure 20 Photograph of the Highly Instrumented Flowfield Survey Rake

CONDITION = (25 RUNS)

PARAMETER	MEAN		STD. DEV.	%
Mi	8.6960E+00	+/-	4.757E-02	0.55
Po	7.5215E+03	+/-	1.755E+02	2.33
Ho	1.0618E+08	+/-	1.417E+06	1.33
To	1.0856E+04	+/-	8.802E+01	0.81
Minf	9.3298E+00	+/-	2.585E-02	0.28
Uinf	1.3875E+04	+/-	8.532E+01	0.61
Tinf	9.1813E+02	+/-	1.552E+01	1.69
Pinf	6.2579E-02	+/-	1.381E-03	2.21
Qinf	3.7753E+00	+/-	8.056E-02	2.13
Rhoinf	5.6487E-06	+/-	1.471E-07	2.60
Muinf	5.6549E-07	+/-	6.458E-09	1.14
Re	1.3864E+05	+/-	4.017E+03	2.90
Gamma	1.3868E+00	+/-	7.450E-04	0.05
Vbarinf	1.7263E-02	+/-	2.295E-04	1.33
Pitot	6.9652E+00	+/-	1.486E-01	2.13
Qo(F-R)	3.2051E+02	+/-	5.043E+00	1.57
Twall	5.3086E+02	+/-	4.597E+00	0.87
Flow Rate	7.8136E-01	+/-	1.816E-02	2.32

RUNS :	7	8	9	10	11	12	14	15	16	17
	18	19	20	21	22	23	24	25	26	27
	28	30	31	32	33					

Figure 21 Summary of the Freestream Variables for the Test Program

pressure. In addition to the Pitot values, a plot of the calculated exit plane Mach number and velocity profiles are included. The test point which these data correspond to is a simulation of 140 kft. (42.7 km) density-altitude at 13,850 ft/sec (4 km/sec). The mean values for the flowfield variables for the test program are given in Figure 21 along with the related statistics.

During each test run, a measurement of the spectral content of the near UV radiation in the nose region of the test model was made. An Optical Multi-channel analyzer (OMA) was used to gain knowledge of the composition of the flowfield throughout the test flow. A 500-microsecond snapshot of the flow was taken during a given test run. The timing of this window was controlled such that measurements were made during flowfield establishment, during the steady test interval, and during flowfield breakdown for many of the model orientations.. The wavelength region that was investigated was that which includes the OH bandhead near 300 nanometers and a strong copper doublet at 325 nanometers. Additionally, temporal radiometric measurements were made for each run with filters that passed information for NO, OH, Cu, and hydrogen alpha contributions. The results of these measurements are presented and discussed in detail in Appendix D to this report.

5.2 Aerothermal Measurements

A suite of aerothermal instrumentation was on-board the model as was described in Section 2. The primary reason for these instruments is for verification of the flowfield around the model. These data provide a good database for comparison with CFD evaluations of the flowfield. Included with this report is an extensive evaluation of the flowfield at zero degrees angle-of-attack. Figure 22 shows a contour map of the Mach number field around the nose of the vehicle. The pressure data are summarized in a series of Figures which show the measured pressure data versus their location along surface of the model measured from the nose of the test vehicle along a ray. Data for repeat test runs are included in the same plots with the test run numbers indicated. Also, the Navier-Stokes predicted surface pressure field is included on the plot for the zero angle of attack cases. A total of 14 plots are included in Figures 23 through 26 which correspond to the 14 orientations of the test model that were investigated. Figure 27 shows a schematic of the model orientation scheme. Figure 23 shows the data for the 0° angle-of-attack case as well as the +/- 2° and +6° pitch cases. Note that the rays along which the instruments are oriented (see Figure 27) are always in the horizontal plane of the shock tunnel, i.e. the pure pitch plane. This is required since the RF antennas must be aligned with the transmitters on the side wall of the tunnel. Therefore, for the test runs with combinations of pitch and yaw (Figures. 24 and 25) the data are not along convenient axes for interpretation. Also, note that for the cases with pure yaw (Figure 24) the data are oriented to reflect the symmetry in the yaw plane and yield equivalent results from either side of the test model.

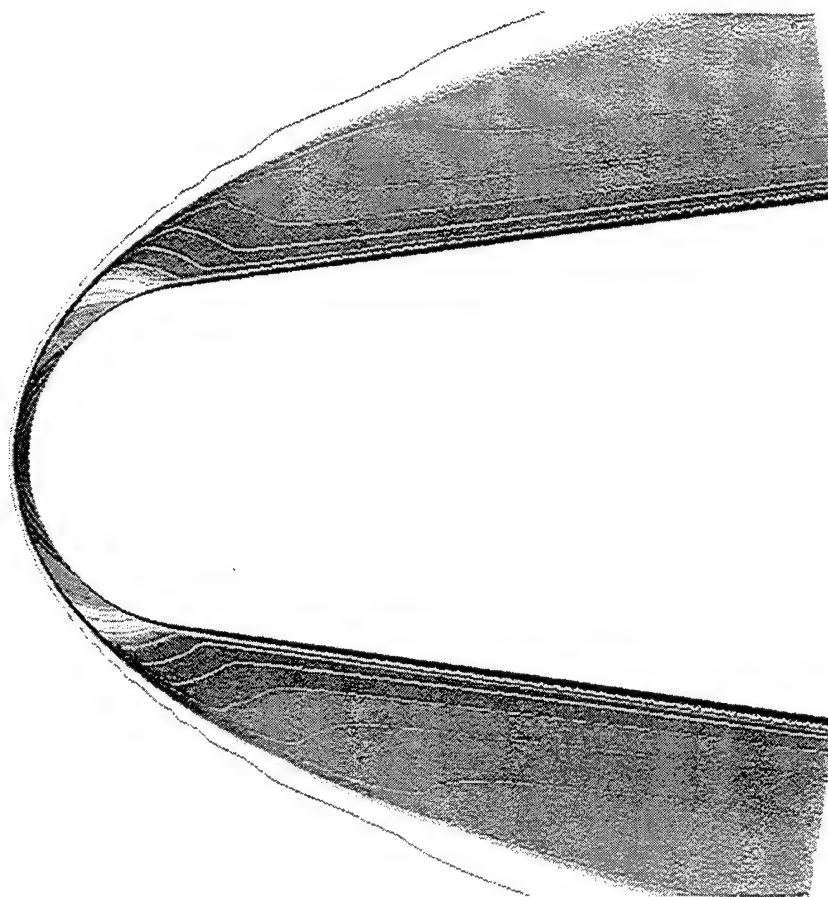


Figure 22 Contour Map of the Flow Around the Nose of Test Model

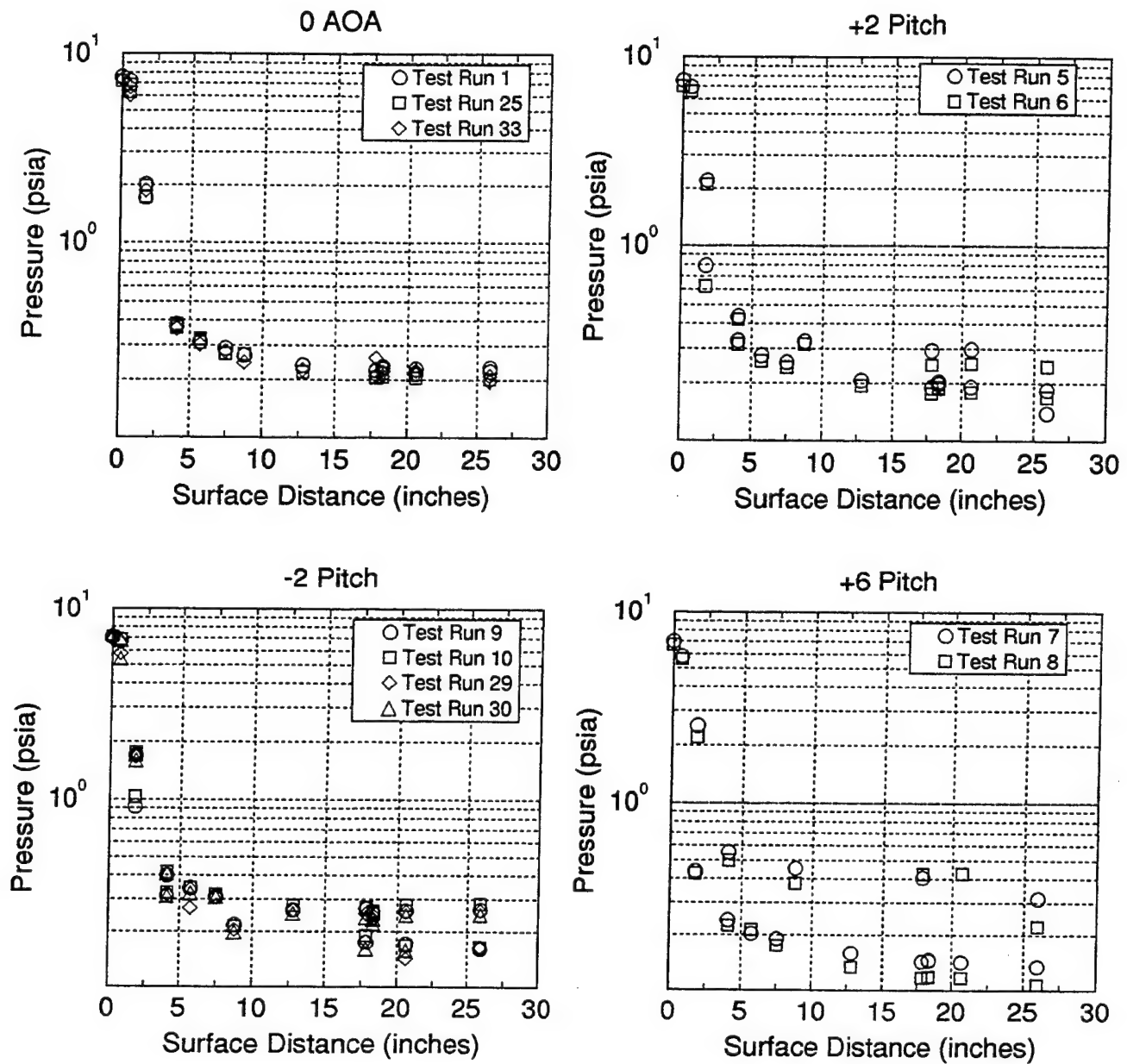


Figure 23 Test Model Surface Pressure Data

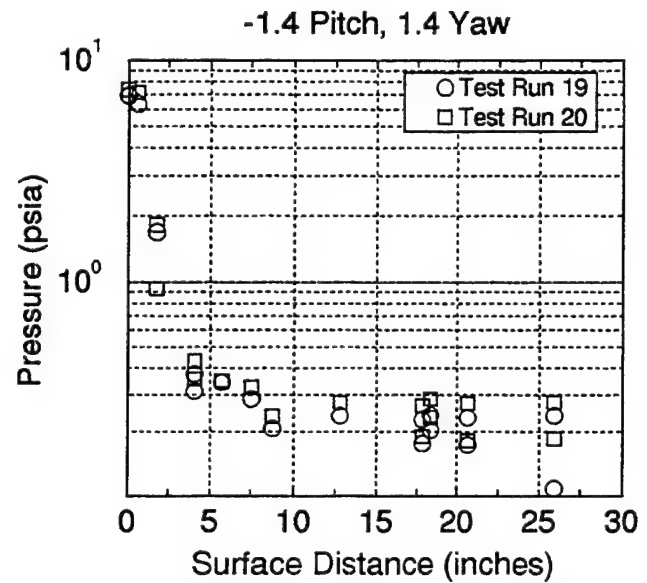
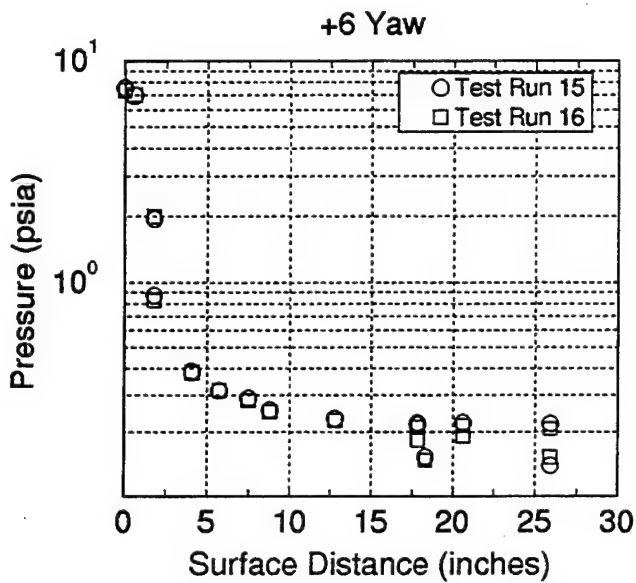
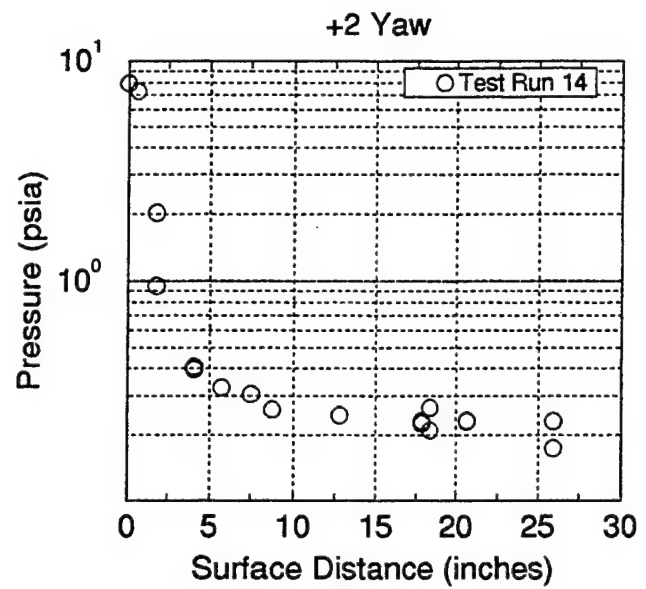
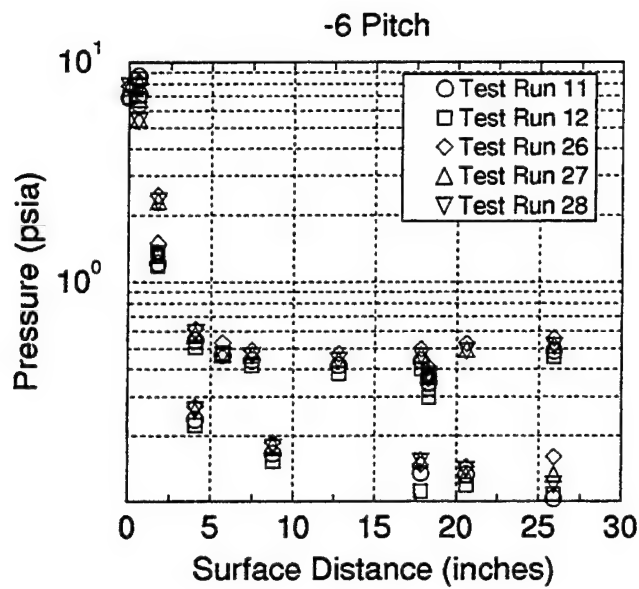


Figure 24 Test Model Surface Pressure Data

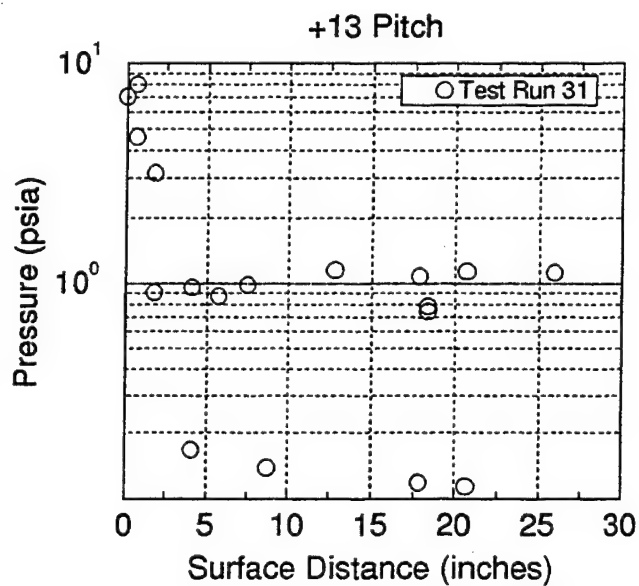
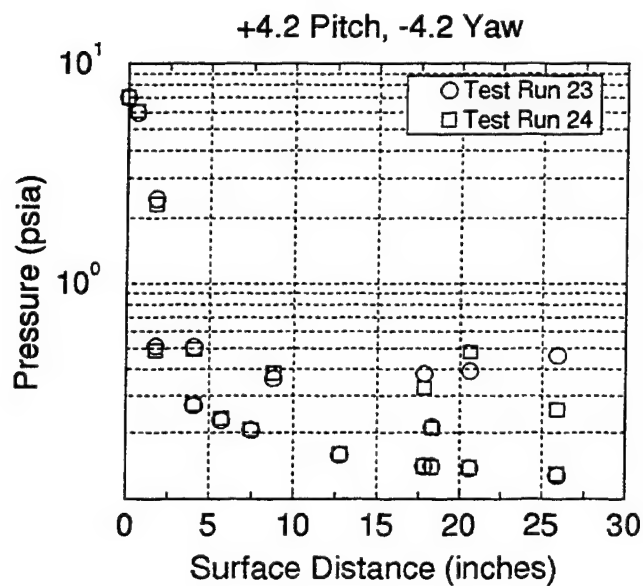
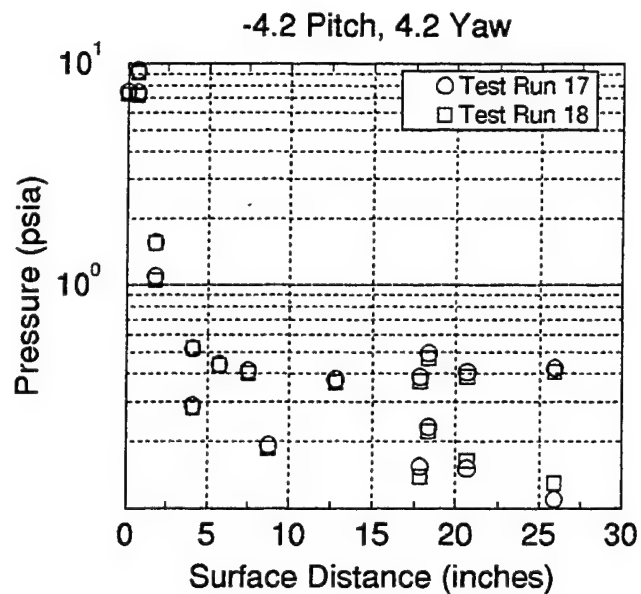
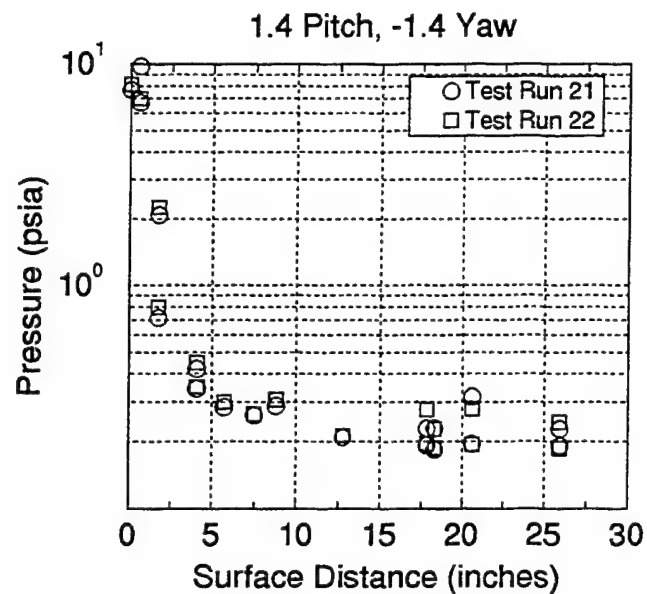


Figure 25 Test Model Surface Pressure Data

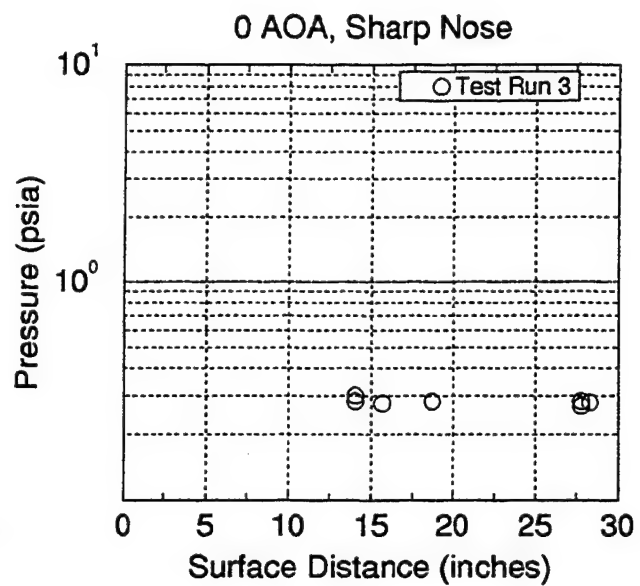
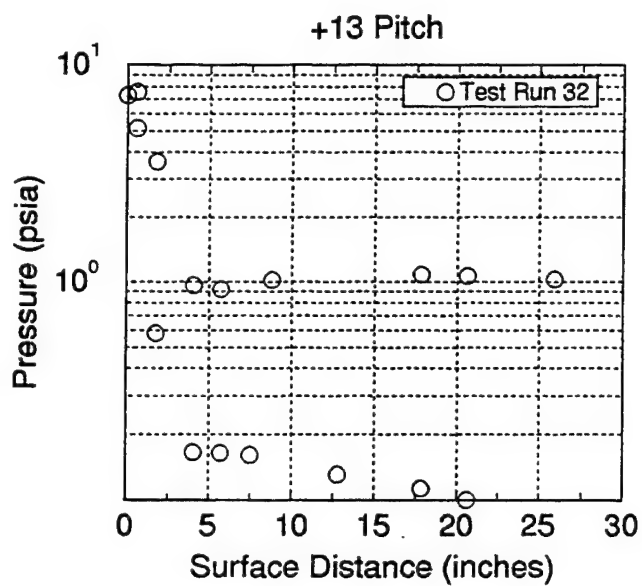


Figure 26 Test Model Surface Pressure Data

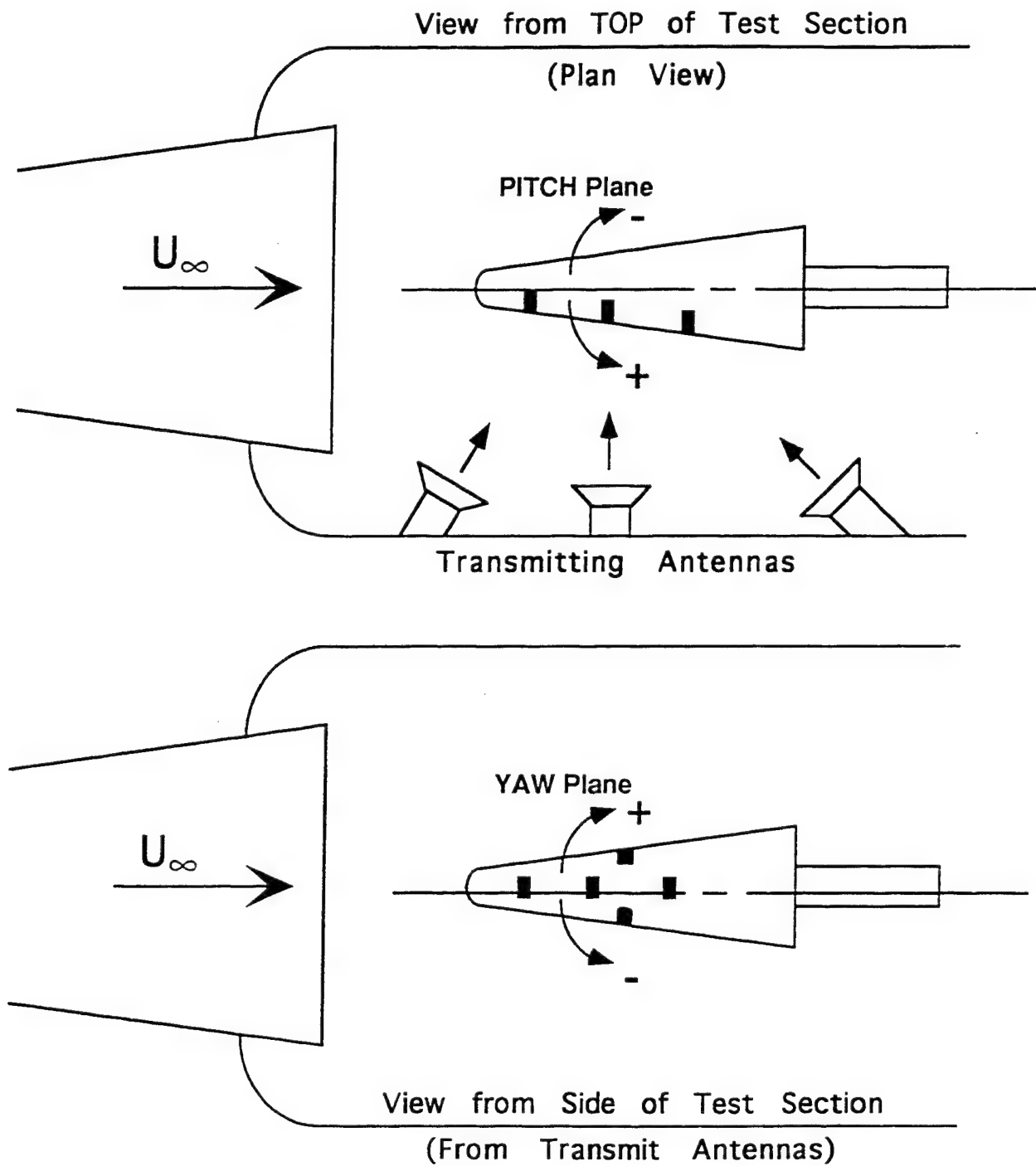


Figure 27 Schematic of the Model Orientation Scheme

Figure 23 shows the pressure data for the 0° AOA case. The data presented in this Figure indicate the results for three separate test runs and show good repeatability of the test flowfield. Additionally, these data agree very well with the Navier-Stokes prediction of the flowfield. Figure 23 also shows the data for the plus and minus two degree cases. The results indicate clearly the differences between the leeward and windward sides of the model and also repeat very well. In general, repeatability of the pressure data was very good and this is illustrated in the remaining pressure data results in Figures 24 and 25.

The surface heat transfer data are presented in a similar manner as the surface pressure data. (See Figures 28 through 31). Wherever possible repeat test runs are incorporated into the same plot to show the consistency in the data set. As with the pressure data, the zero degree angle-of-attack case (Figure 28) is compared with the Navier-Stokes prediction. Except for some disagreement in the near stagnation region the results compare well. The disagreement near the stagnation region was observed in a previous research program as well (Ref. 1). However, the magnitude of the disagreement has been decreased in this experiment. It is not, at this time, clearly understood why this disagreement exists and the author is unable to attribute this completely to one source or the other, i.e. experiment or computation.

5.3 Electron Number Density Measurements

As was described in Section 2, the electron number densities were measured with thin-wire electrostatic probes. These probes were mounted in a five probe rake and data was taken at two stations corresponding to the forward and mid-point between antennas two and three which is the location of antennas four and five. Figure 32 shows the location of the probes in relation to the RF antennas and from the nose of the test model. The process for reducing the electrostatic probe data is described in detail in Appendix C. Essentially, the data were obtained by ramping a voltage linearly from -5 volts to +3 volts over a 100 microsecond time period. Four of these ramps were sequenced during a single test run to ensure that data would be recorded during the steady test interval. During the performance of the tests, the timing of the airflow over the model provided in many cases two of the input ramps during the test period. Some selected profiles are presented here to show the trends and typical profile behavior. The full data set is included in Appendix E.

Figure 33 shows the electron number density profiles for Test Runs 25 and 33. These test runs represent repeat data for the zero degree angle-of-attack case at the forward position identified by ES-1. This position is 7.8 inches (19.8 cm) along the surface from the nose of the test model. These two tests give a good indication of the repeatability of the test

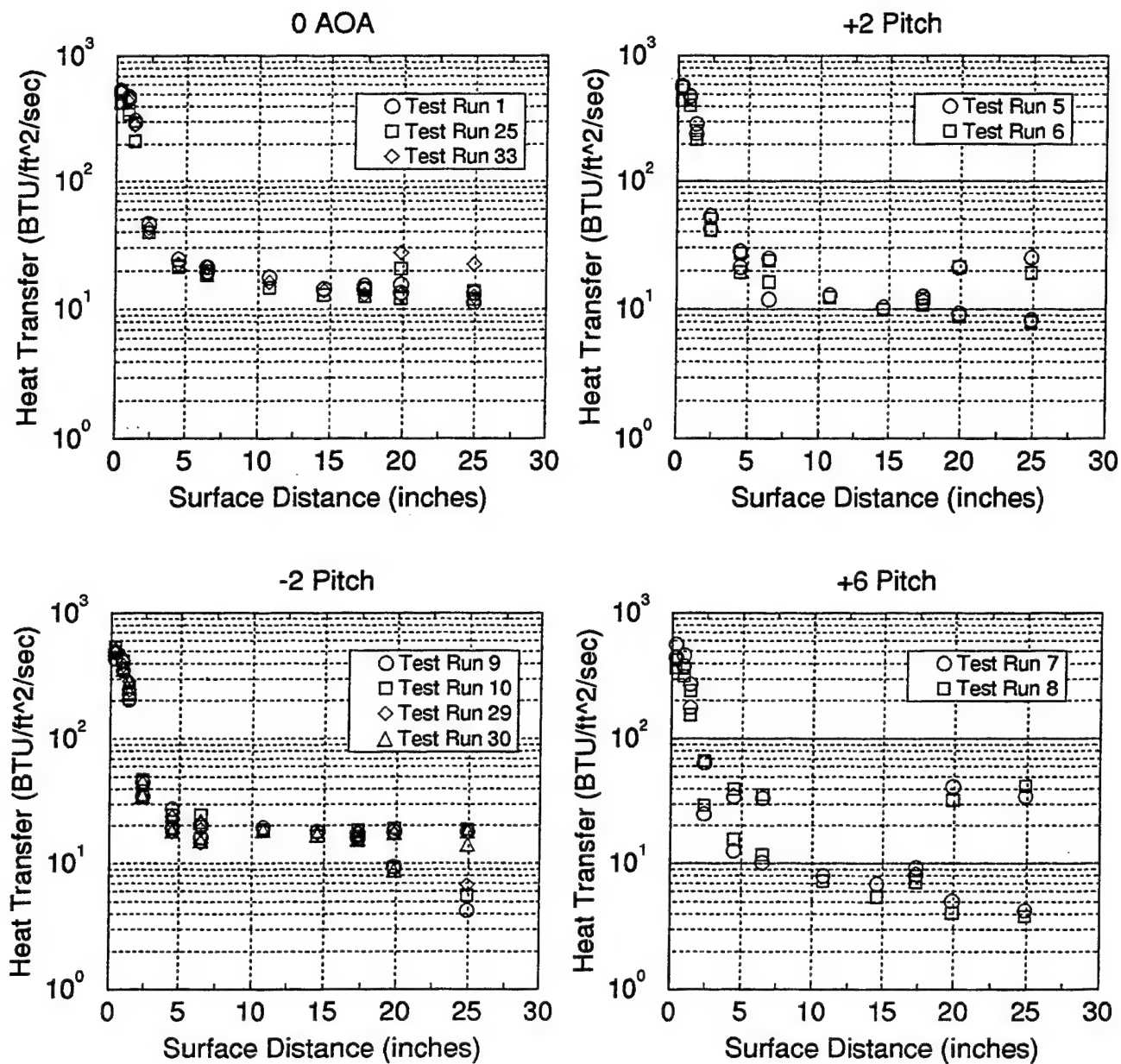


Figure 28 Test Model Surface Heat Transfer Data

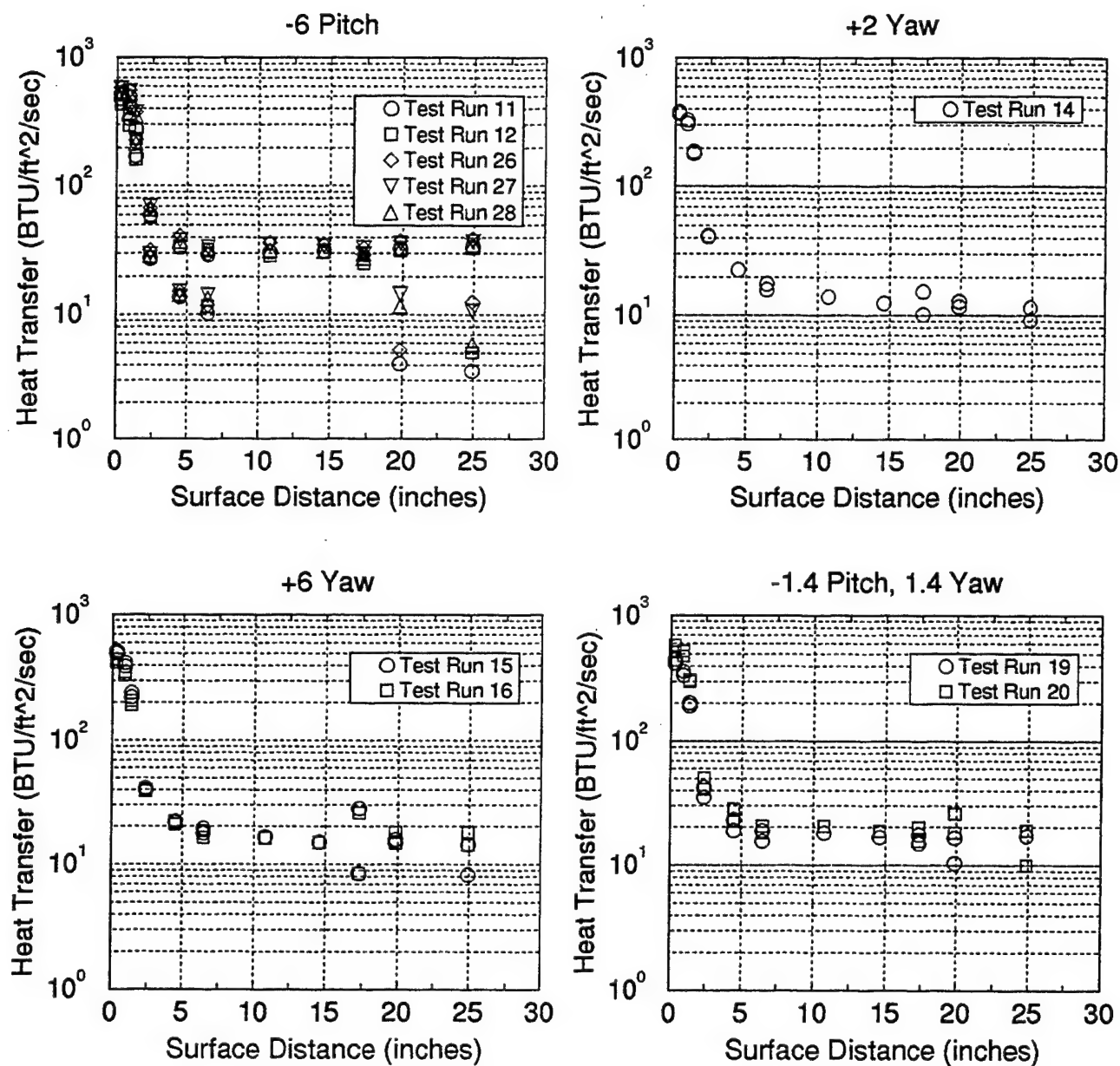


Figure 29 Test Model Surface Heat Transfer Data

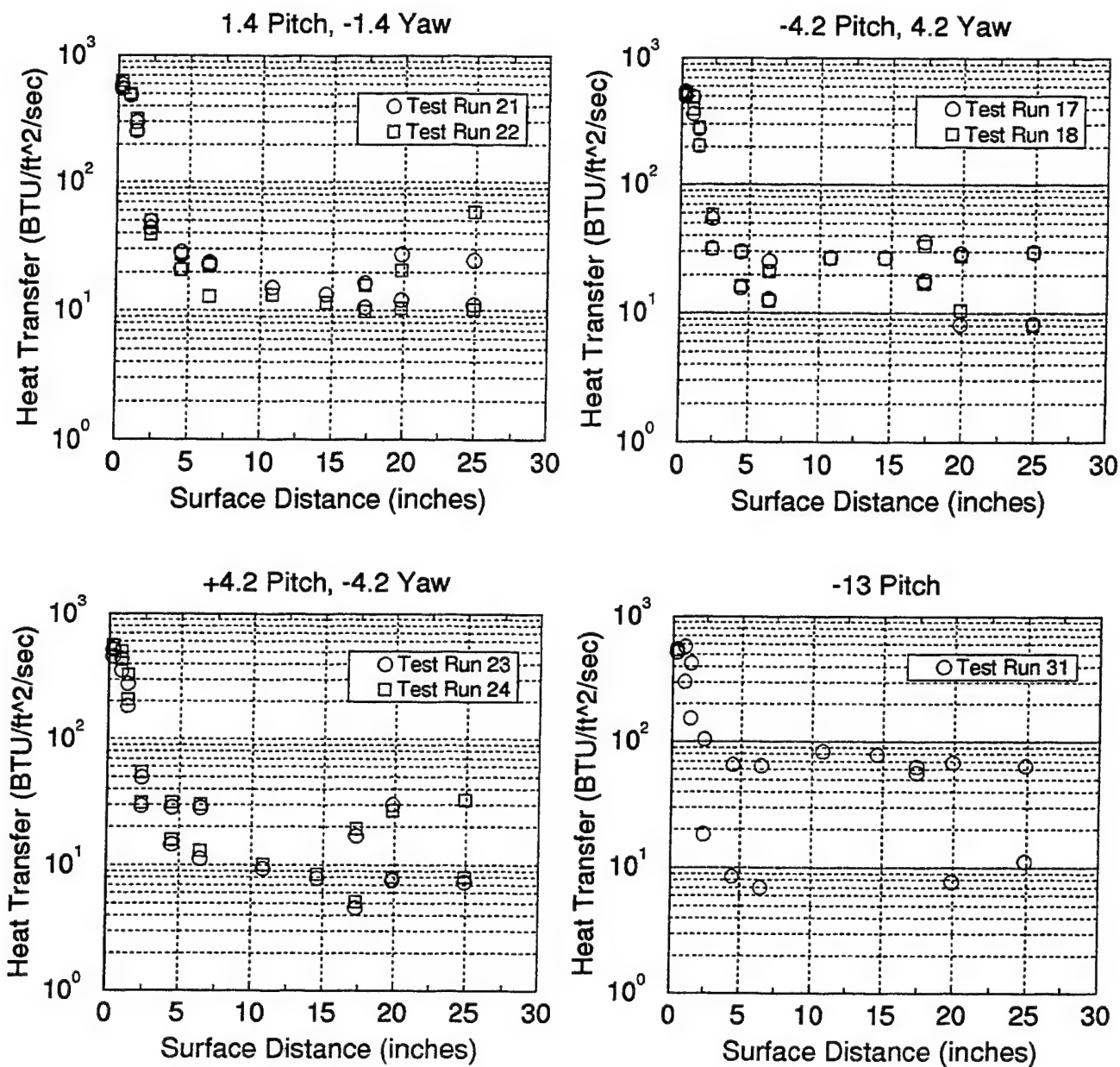


Figure 30 Test Model Surface Heat Transfer Data

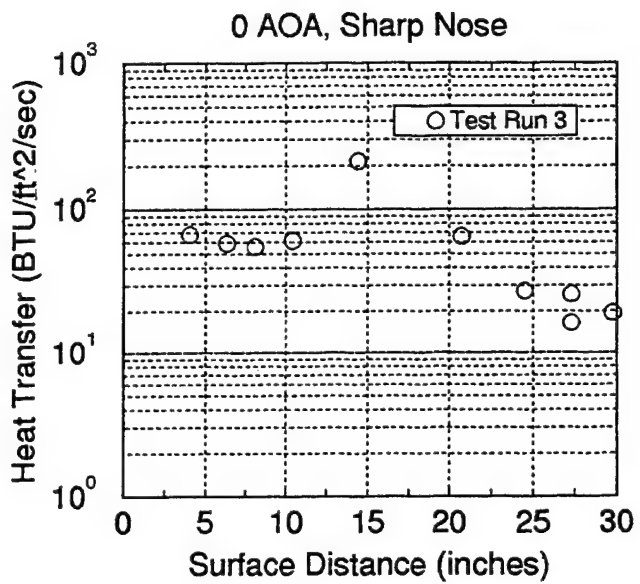
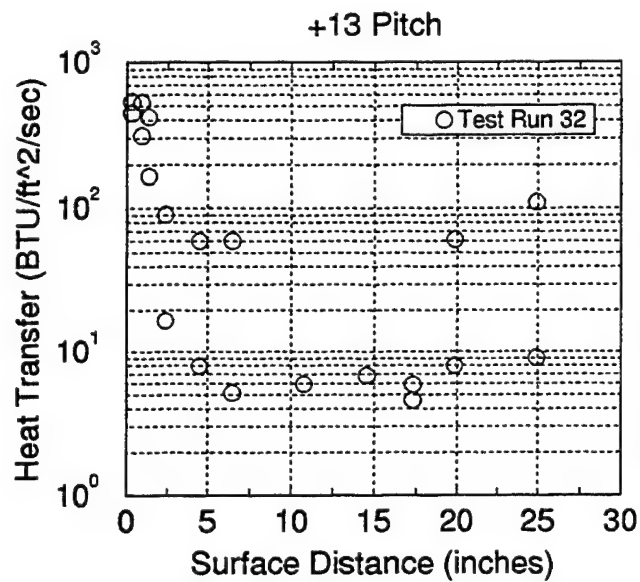


Figure 31 Test Model Surface Heat Transfer Data

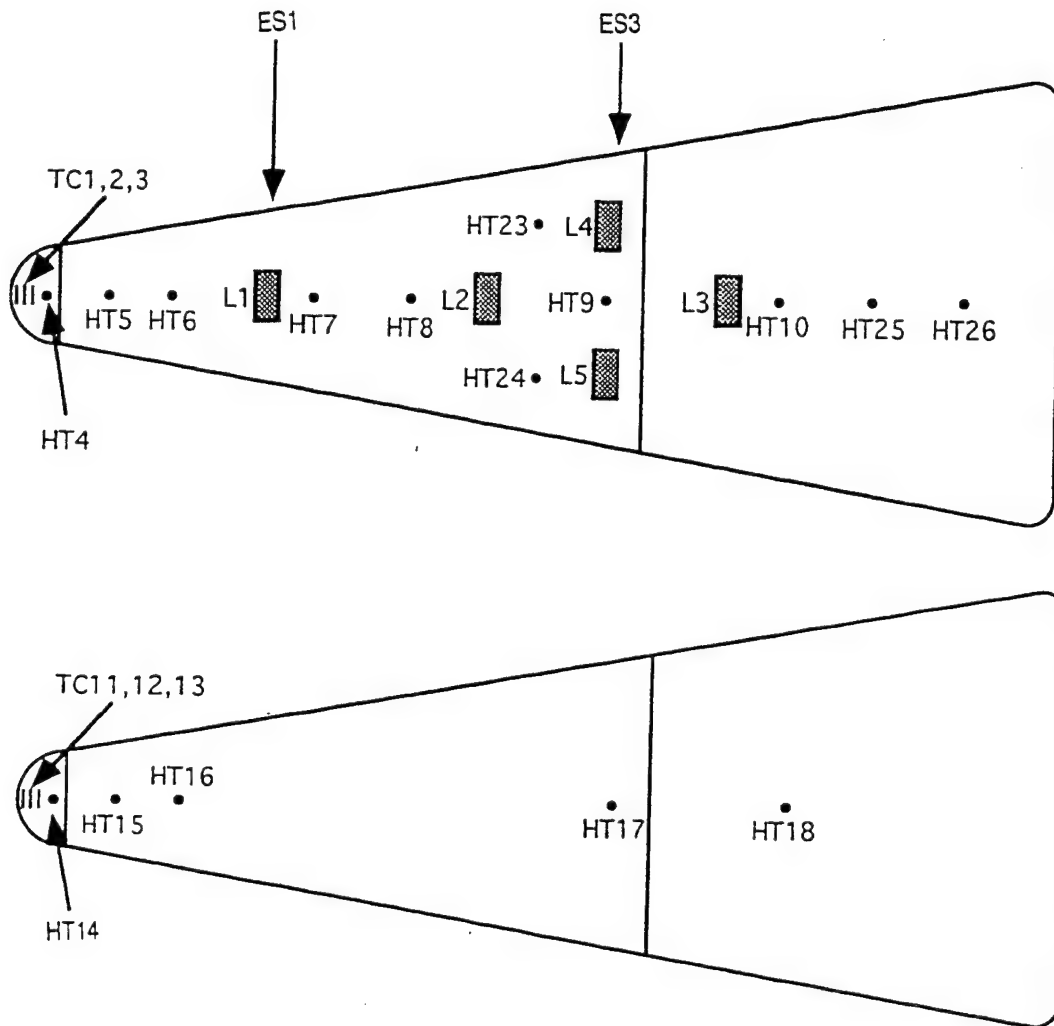


Figure 32 Schematic Showing the Locations of the Heat Transfer Gauges and the L-Band Antennas

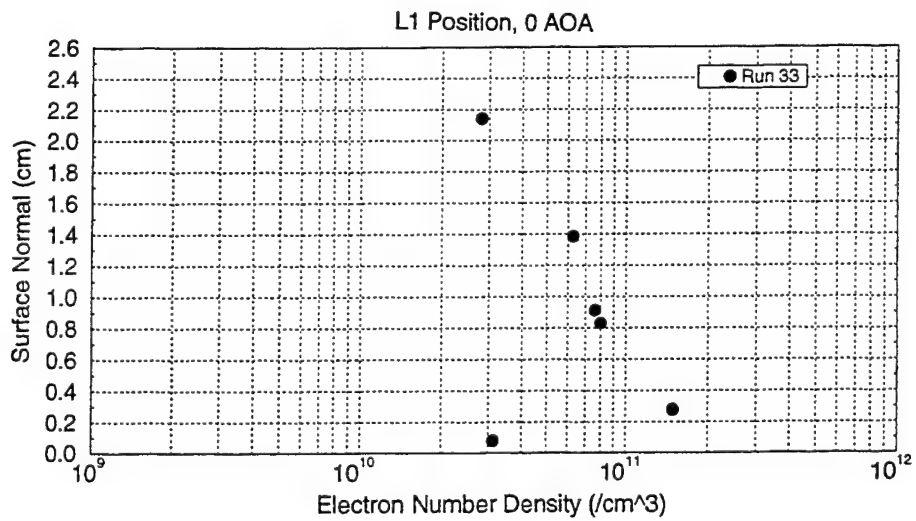
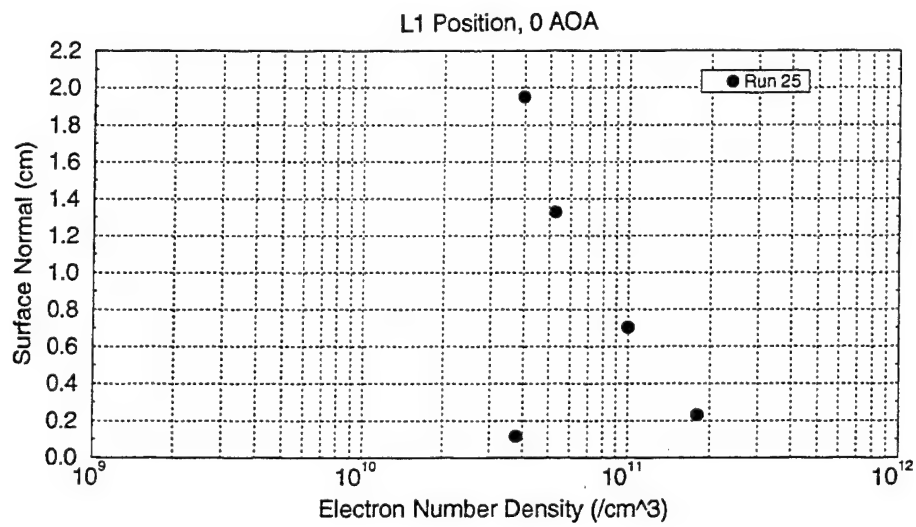
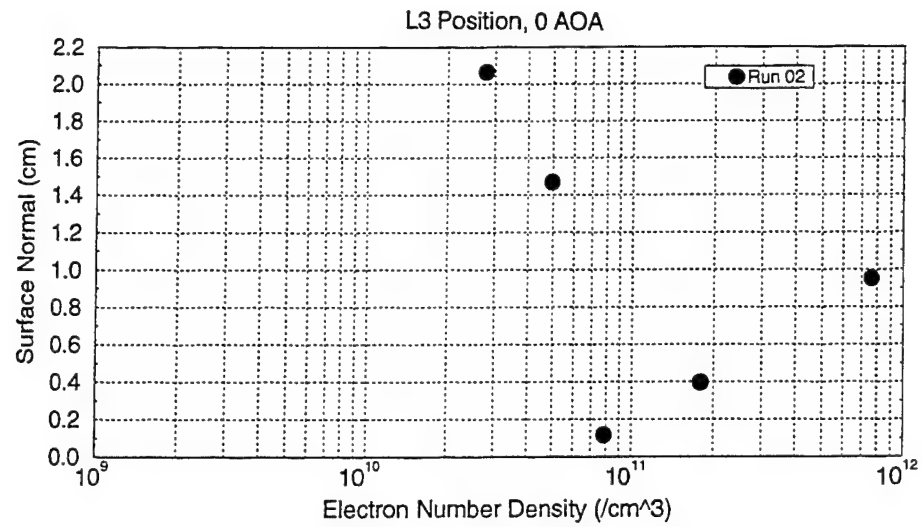


Figure 33 Electron Number Densities for Test Runs 2, 25 and 33 at 0° AOA

flow. The profile shapes from the two runs are nearly the same with the peak number density level located approximately 0.25 cm (0.01 inches) above the model surface at a density level of slightly greater than $1.0 \times 10^{11} \text{ cm}^{-3}$. Test Run 2 also identified in Figure 33 shows the number density data for zero degrees angle-of-attack for the ES-2 position which is located 18.5 inches (47 cm) from the nose of the model. In this case, the data is somewhat sparse, however, the number density levels are nearly the same as in the ES-1 position data with an indication of a thicker plasma layer up to 0.4 cm (0.16 inches) above the model surface.

The following discussion regarding electron number densities at various angles-of-attack follows the convention depicted in Figure 27. Positive pitch indicates electron number densities measured on the windward side of the vehicle and negative pitch relates to leeward measurements. In general, the windward layer is thin relative to the leeward layer and also it is thin in some cases relative to the resolution obtainable with the probe rake used to collect the data. Therefore, in some cases the resolution of the windward data is not sufficient to completely describe the profile shape. Figure 34 shows the windward data collected for the +2 degrees pitch orientation. At the ES-1 position the peak level is approximately $2.5 \times 10^{11} \text{ cm}^{-3}$ and the peak level is decreased back at the ES-2 position to $1.1 \times 10^{11} \text{ cm}^{-3}$. The distance above the surface for the peak level is not very discernible at this position. The +6 degrees pitch or windward data includes two test runs and is shown in Figure 35. At the ES-1 position at peak level slightly less than 10^{11} is indicated. A slightly higher level is shown for the ES-2 position, however the resolution for these profiles is most likely insufficient to describe the layer completely since the thickness of the layer appears to be less than 0.5 cm (0.2 inches). There are two profiles obtained for the +2 degree yaw case. These are shown in Figure 36. The peak levels are shown to be near $2.0 \times 10^{11} \text{ cm}^{-3}$ at about 0.4 cm (0.16 inches) above the surface at the ES-1 position. The peak level decreases slightly back at the ES-2 position and the layer thickens somewhat, however the resolution here is not adequate for a more detailed discussion.

On the leeward side of the model, the plasma sheath is thicker and better defined by the thin-wire probe measurements. Figure 37 shows the data collected for the -2 degrees pitch case. At the ES-1 position, a peak electron number density of $1.1 \times 10^{11} \text{ cm}^{-3}$ at 0.35 cm (0.14 inches) above the surface is observed. Further back along the surface at the ES-2 position, the peak in the profile is seen to have moved out near the 1.0 cm (0.4 inches) level from the surface. The -6 degree pitch data shown in Figure 38 similar peak numbers at slightly greater than $1.0 \times 10^{11} \text{ cm}^{-3}$ at the ES-1 position at 0.4 cm above the surface of the model. Moving back to the ES-2 position indicates a thickening of the layer with the peak number density observed out near 1.0 cm at near the same level of $1.0 \times 10^{11} \text{ cm}^{-3}$ as the ES-1 position.

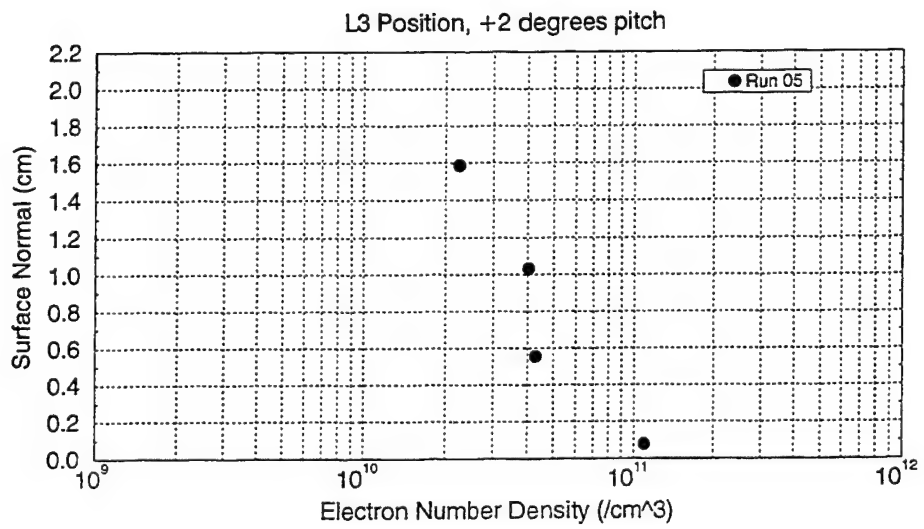
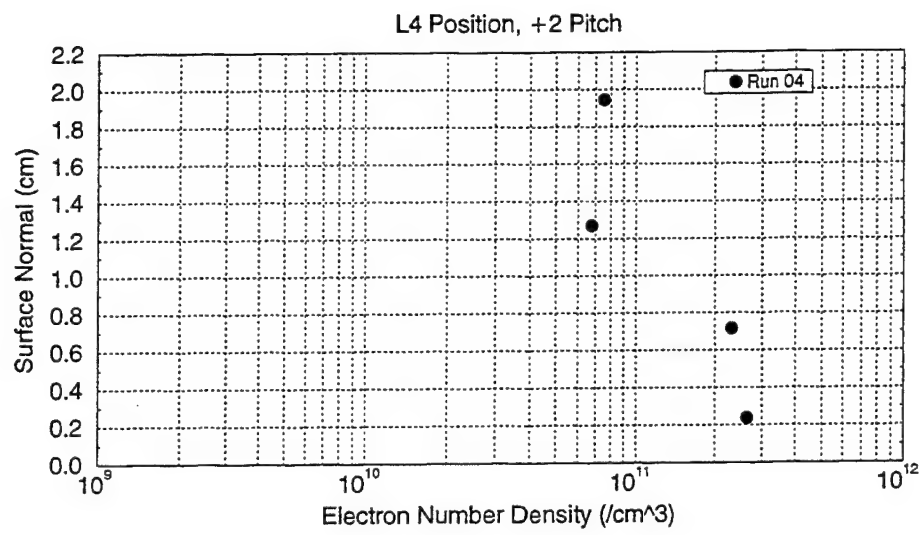


Figure 34 Electron Number Density for the +2° Pitch Test Model Orientation

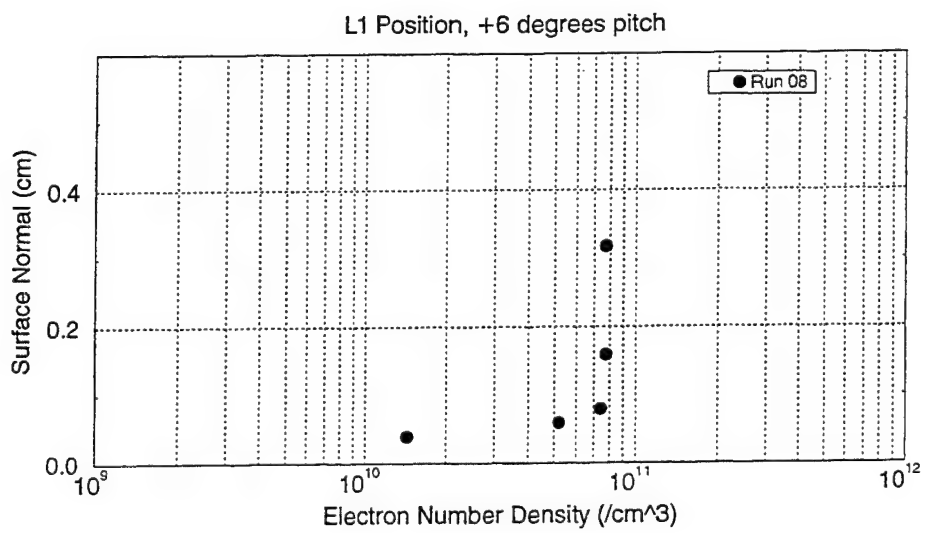
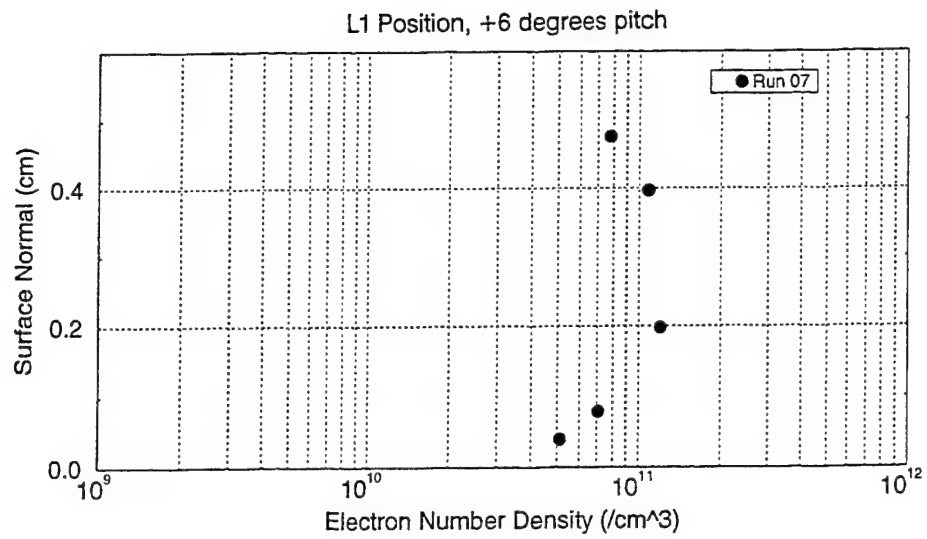


Figure 35 Electron Number Density for the +6° Pitch Test Orientation

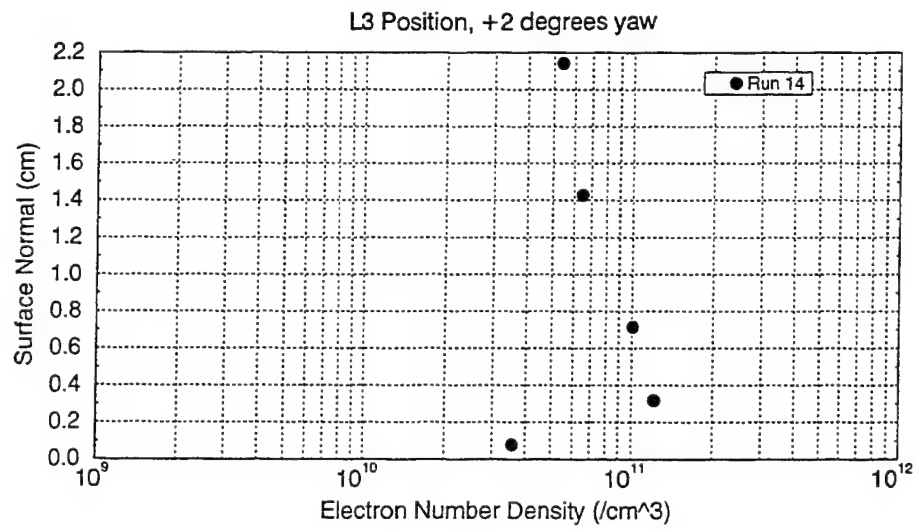
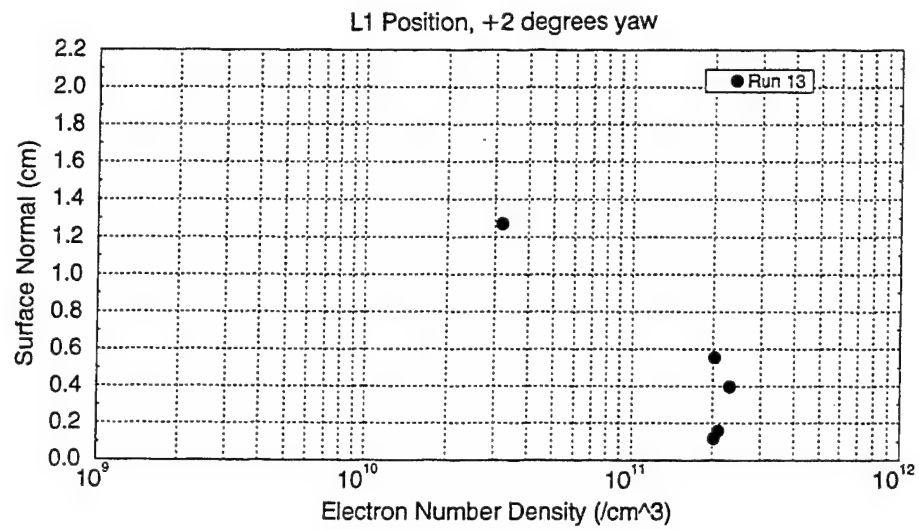


Figure 36 Electron Number Density for the +2°Yaw Test Model Orientation

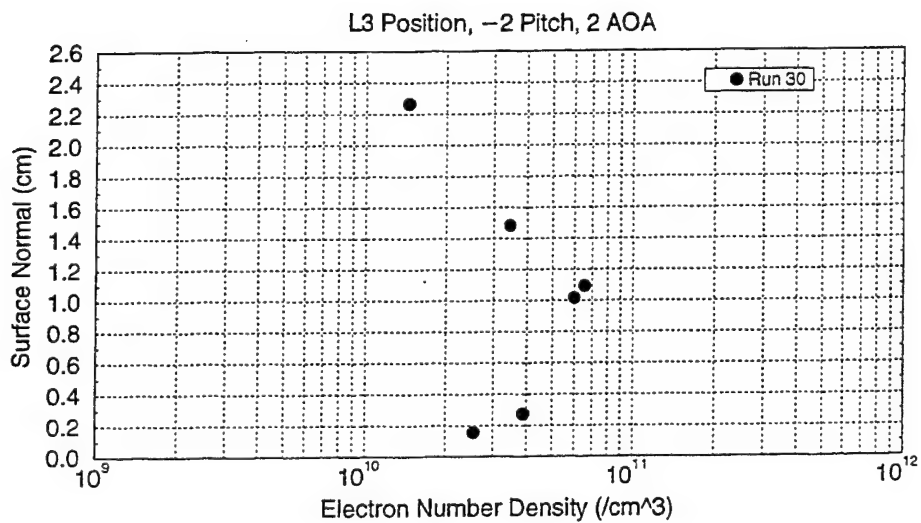
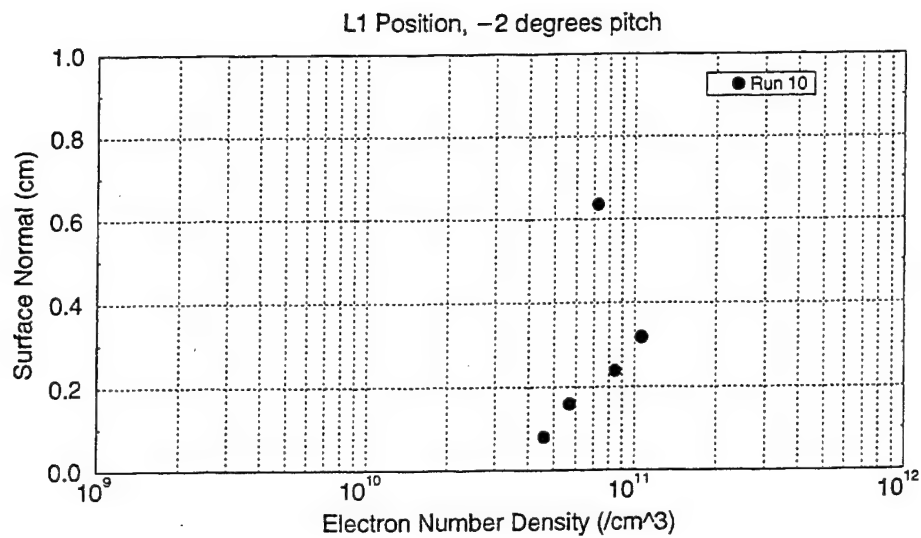


Figure 37 Electron Number Density for the -2° Pitch Test Model Orientation

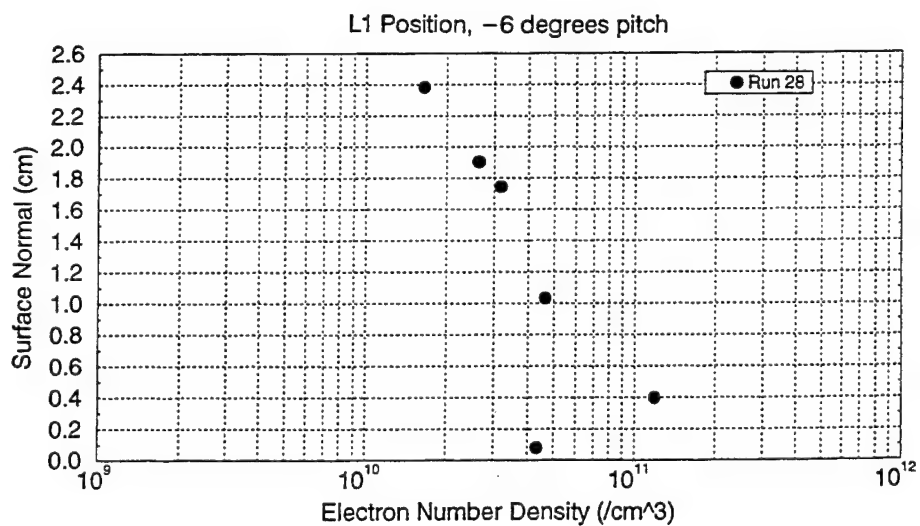
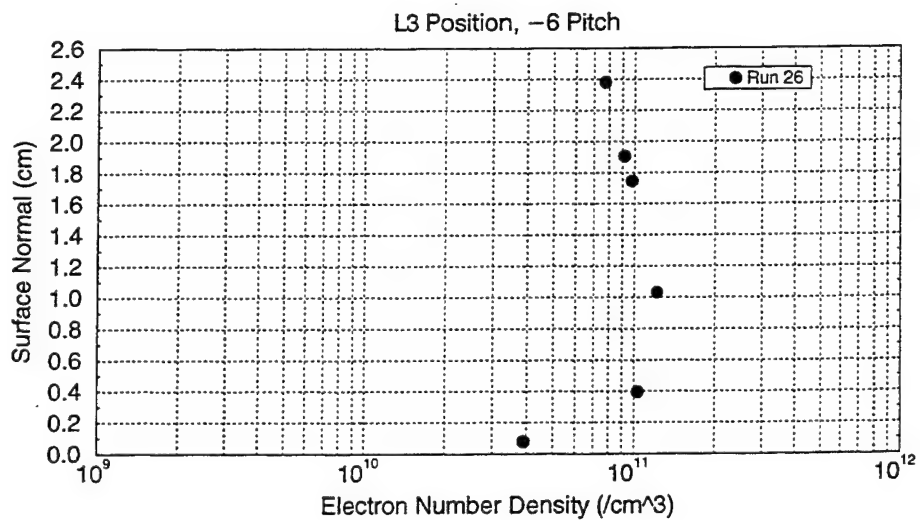
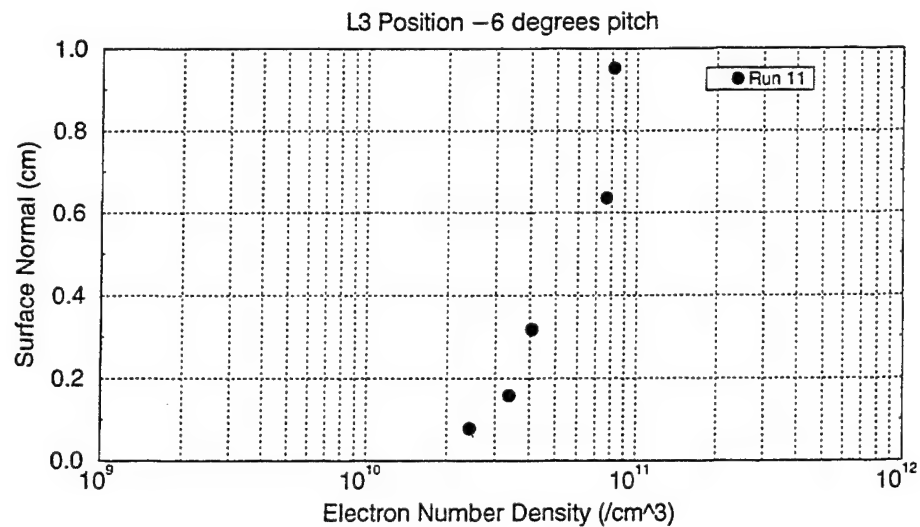


Figure 38 Electron Number Density for the -6°Pitch Test Model Orientation

6.0

SUMMARY AND CONCLUSIONS

A comprehensive shock tunnel program has been performed on the quantitative measurement of RF interactions, at L-band frequency, with the plasma environment about a hypersonic vehicle during reentry. The shock tunnel operating conditions generated a freestream test flow at a velocity of 14,000 ft/sec, at an equivalent density altitude of 140 kft. The measurements, performed under laminar flow conditions, comprise a database on the plasma-induced attenuation and phase shift for near broadside irradiation of the vehicle, at selected vehicle orientations so as to include the effects of crossflow on the measurements. The model was illuminated with RF energy from inside the test chamber of the shock tunnel from three separate transmitters at a forward, broadside, and aft line-of-sight.

During the period of test flow, RF propagation was switched from the remote transmitter (uplink) to the center antenna on the model. In this mode, the complex reflection coefficient of this antenna was measured, as well as the amplitude and phase of the signals coupled from this antenna into the four adjacent antennas. The sequenced switching from uplink to coupled mode was made every 10 microseconds during the approximately 900 microsecond period of test flow.

Careful calibration procedures were employed to remove the effect of all measurement system components, and to reduce the RF data to aperture-plane values. The data therefore represent the change in signal levels from free space values, due only to the effects of flowfield plasma.

Pressure and heat transfer rate distributions were obtained over the model surface during the experiments, and diagnostic measurements of electron number density profiles were also performed, on a non-interference basis with the RF measurements, at different locations in the plasma flowfield, to characterize the plasma profiles appropriate to the different vehicle orientations investigated.

In summary, the RF data base obtained from this measurements program involving simulated reentry flow field plasmas comprises:

- profile measurements which quantify the flow field plasma, and
- measured RF interaction effects (on received signal amplitude and phase, antenna reflection coefficient, antenna coupling) at the aperture planes for different antenna

locations at L-Band frequency for three known line of sight/model orientation geometries which included crossflow effects on the measurements.

The overall experimental objectives were achieved in providing a comprehensive database on the effects of angle of attack of a hypersonic vehicle on the measured electron number density profiles in the shock layer, the measured surface heat transfer rate distributions, and on RF propagation behavior at near broadside aspect angles. At the selected vehicle orientations, which introduced crossflow effects, the data exhibited both good repeatability and consistency. In particular, relative to the zero angle of attack case, all of the data exhibited behaviors which were fully consistent with the responses expected for the change in flowfield environment produced by the changes in vehicle attitude.

Preliminary analyses and comparisons have also indicated that measured electron number density profile levels are in agreement with predicted values. The measured heat transfer levels were also found to be higher than predicted near the stagnation point, but in good agreement with theory otherwise.

The possibility of ionization enhancement due to non-air species in the flow was also examined. Another potential source of enhanced ionization in these high total enthalpy flows could be copper from the nozzle throat. Gradual enlargement of the copper throats did occur during the shock tunnel runs (throats were replaced after a diameter enlargement of about 3%). Stagnation region spectra, recorded by means of an optical multi-channel analyzer indicated that many line or band systems were contributing to the stagnation region radiation. However, it is not believed that any of these contaminant systems afforded any significant contribution to the electron number densities due to air species measured during this program.

It has been shown that the present data (RF, heat transfer, electron number density) exhibit good consistency in their behaviors, relative to the axisymmetric zero angle of attack case, to changes in model orientation with respect to the freestream flow direction. The program measurements provide flow field analysts and RF code developers with a comprehensive database with which to study angle of attack effects on aerothermal distributions, electron number density profiles and near broadside electromagnetic uplink propagation and mutual coupling.

7.0

REFERENCES

1. Boyer, D. W., "Reentry Vehicle Flowfield Plasma Effects, Including Angles of Attack, on RF Uplink Signal Propagation and Mutual Coupling, Calspan Report. No. 7515-4, May 1991.
2. Curtis, J.T., and Strom, C.R., "Computations of the Nonequilibrium Flow of a Viscous, Radiating Fluid About a Blunt Axisymmetric Body", AbPvL-TR-67-40, Vol. 1, June 1967; CAL Report AM-2113-Y-1, January 1967.
3. Blottner, F.G., "Nonequilibrium Laminar Boundary Layer Flow of Ionized Air", AIAA J., 2, 1921, November 1964.
4. Boyer, D.W., "Experimental Studies of Flush-Mounted Electrostatic Probes in Collision-Dominated Hypersonic Ionized Flows", Sandia Laboratories Report SC-CR.-72-3145, July 1972.
5. Saterlie, S.F., "Antenna Window Placement for the Calspan Boresight Model", TRW letter to BMO, F840.SFS.86-034, 18 November 1986, TRW Ballistic Missiles Division, San Bernadino, CA.
6. Boyer, D.W., and Touryan, K.J., "Experimental and Numerical Studies of Flush Electrostatic Probes in Hypersonic Ionized Flows: I. Experiment", AIAA Journal, Vol. 10, No. 12, pp. 1667-1674, December 1972.
7. Boyer, D.W., and Andre, S.N., "Theoretical and Experimental Studies of Microwave Interaction Effects in a Hypersonic Air Plasma", Sandia Laboratories Report SC-CR-723164, October 1972.
8. Saterlie, S.F., "Calspan Boresight Error Data Analysis at X-Band", TRW letter to BMO, F840.SFS.87-033, 10 September 1987, TRW Ballistic Missiles Division, San Bernadino, CA.
9. Saterlie, S.F., "Calspan Broadside Microwave Data Analysis", TRW Interoffice Communication F841.SFS.88-020, 06 June 1988, TRW Ballistic Missiles Division, San Bernadino, CA.
10. Iskra, M., and Chaiken, S., "Comments on Calspan Tasks", TRW Interoffice Communication K342-MAI-88-004, 09 March 1988, TRW Applied Technology Division, Redondo Beach, CA.
11. Wurster, W.H., "Capability for Chemistry and Radiation Studies in the Calspan 96-inch Shock Tunnel", Calspan IR&D Project 87-480 Report, March 1990.
12. Boyer, D.W., "Boresight Error Slope Measurements Program", Calspan Report No. 7515-1, Volume 1, May 1989.
13. Gaydon, A.G., "The Spectroscopy of Flames", John Wiley and Sons, Inc., New York, 1957.

14. Boyer, D.W., "Boresight Error Slope Measurements Program. Aperture-Plane Data for S-Band RF Signal Attenuation, Phase Shift, Antenna Coupling and Reflection Coefficient", Volumes 2 and 3. "Aperture-Plane Data for X-Band Reflection Coefficient", Volume 4, Calspan Report No. 7515-1, May 1989.
15. Boyer, D.W., "Measured Surface Heat Transfer Rate Distributions for Model Attitude Orientations During RF Interaction Experiments", Calspan Report No. 7515-3, October 1990.
16. Fay, J.A., and Riddell, F.R., "Theory of Stagnation Point Heat Transfer in Dissociated Air", J. Aero. Sci. X, 73, February 1958.
17. Cohen, N.B., "Boundary Layer Similar Solutions and Correlation Eqs for Laminar Heat-Transfer Distribution in Equilibrium Air at Velocities up to 41,100 feet per second", NASA TR R-118, 1961.
18. Zoby, E.V., "Approximate Relations for Laminar Heat Transfer and Shear-Stress Functions in Equilibrium Dissociated Air", NASA TN D-4484, April 1968.
19. Kemp, N.H., Rose, P.H., and Detra, R.W., "Laminar Heat Transfer Around Blunt Bodies in Dissociated Air", J. Aero. Sci. X, 421, July 1959.
20. Holden, M.S., et al., "An Experimental Study of Particle-Induced Convective Heating Augmentation", ALAA Paper 76-320, AIAA 9th Fluid and Plasma Dynamics Conf, San Diego, CA, July 14-16, 1976.
21. Holden, M.S., "Studies of Potential Fluid-Mechanical Mechanisms for Enhanced Stagnation-Region Heating", AIAA Paper 85-1002, AIAA 20th Thermophysics Conf., Williamsburg, VA, June 19-21, 1985.
22. Dunbar, L.E., Courtney, J.F., and McMillen, L.D., "Heating Augmentation in Erosive Hypersonic Environments", AIAA J. 13, 908, July 1975.
23. Keyes, J.W., and Hains, F.D., "Analytical and Experimental Studies of Shock Interference Heating in Hypersonic Flows, NASA TN D-7139, May 1973.
24. Boyer, D.W., "Measured Electron Number Density Profiles in the Model Flowfield During RF Interaction Experiments", Calspan Report No. 7515-2, July 1989.
25. Saterlie, S., Glatt, L., Iskra, M., Boyer, D., and Fryer, J., "Ground Test Measurement of Hypersonic Flowfield Plasma Effects", paper presented at AIAA Missile Sciences Conference, Naval Postgraduate School, Monterey, CA, November 13-15, 1990.

APPENDIX A ANTENNA COUPLING DATA REDUCTION TO OBTAIN ANTENNA SCATTERING PARAMETERS

Antenna coupling measurements were performed on the blunt-nose model as part of the bench checkout tests prior to model installation in the shock tunnel test section, as noted in Section 3.1.2. These measurements, like those for antenna reflection coefficient, were made at the bulkhead connectors at the rear of the model using a network analyzer. The network analyzer was calibrated for coupling by connecting the input and output connectors with a barrel connector and setting the network analyzer to 0 dB and 0 degrees. The insertion phase of the barrel connector was determined and the reduced data were corrected for this phase shift.

Figure A1 shows the configuration of the two antenna feed networks, "A" and "B" between the bulkhead connectors and the antenna apertures, coupled by free-space, indicated here as the "a" network. The scattering parameters for the antenna feed networks and the free-space aperture reflection coefficients, $S_{11}(a)$ and $S_{22}(a)$, are known based on the measurements described in Section 3.1.1. Measurements were made of the coupling coefficients at the bulkhead connectors which provided the ratio VEAS/VINC as shown in Figure A1. The scattering parameter $S_{12}(a)$ is the scattering parameter defining the coupling between the two antennas referred to the antenna apertures. The following analysis then permits the determination of these parameters from the measured data. The equations referred to in the discussion are shown in Table A1.

The Antenna "A" feed network is the driven antenna and the incident voltage is input at port 1 of this network. Eq (1) is based on the definition of scattering parameters, and Eqs (2) and (3) are definitions. Eq (3) uses the free space antenna "A" reflection coefficient. Substituting Eqs (2) and (3) into Eq (1) results in Eq (4).

*NOTE 1: Eq (3) is a simplification of the 5-port "a" network scattering parameter Eqs and assumes the aperture coupling between antennas is small. The largest coupling is less than -20 dB and thus Eq (3) is accurate to better than 1%.

*NOTE 2: At the antenna "B" feed network it is assumed that the network analyzer is well matched and thus the incident voltage at (B) is zero, as given by Eq (5). Eqs (6) and (7) result from the scattering Eqs for the "B" network using Eq (5), Eq (8) is a definition and Eq (9) results from Eqs (6) and (8).

Eq (10) is one of the scattering Eqs for the "a" network using the relationships for the scattering variables of the "a" network in terms of the "A" and "B" networks as given in Table A1. Eq (11) is obtained by substituting Eq (7) into Eq (10), and Eq (12) by solving Eq (11) for the desired scattering parameters. Finally, Eq (13) results after substituting Eqs (4) and (9) into Eq (12). Note that this Eq satisfies reciprocity in that if the driven and measured ports are reversed, the same Eq applies. Eq (13) was used to determine the scattering parameters from the measured data.

The self-reflection coefficients of the antennas, the main diagonal, were entered using the measured and reduced free-space antenna reflection coefficient data from these bench tests (Sec. 3.1.1, Table 1). The data are reasonably consistent except for the L-band coupling from antennas 1, 2 and 3 to antennas 4 and 5 which is expected to be the same based on symmetry.

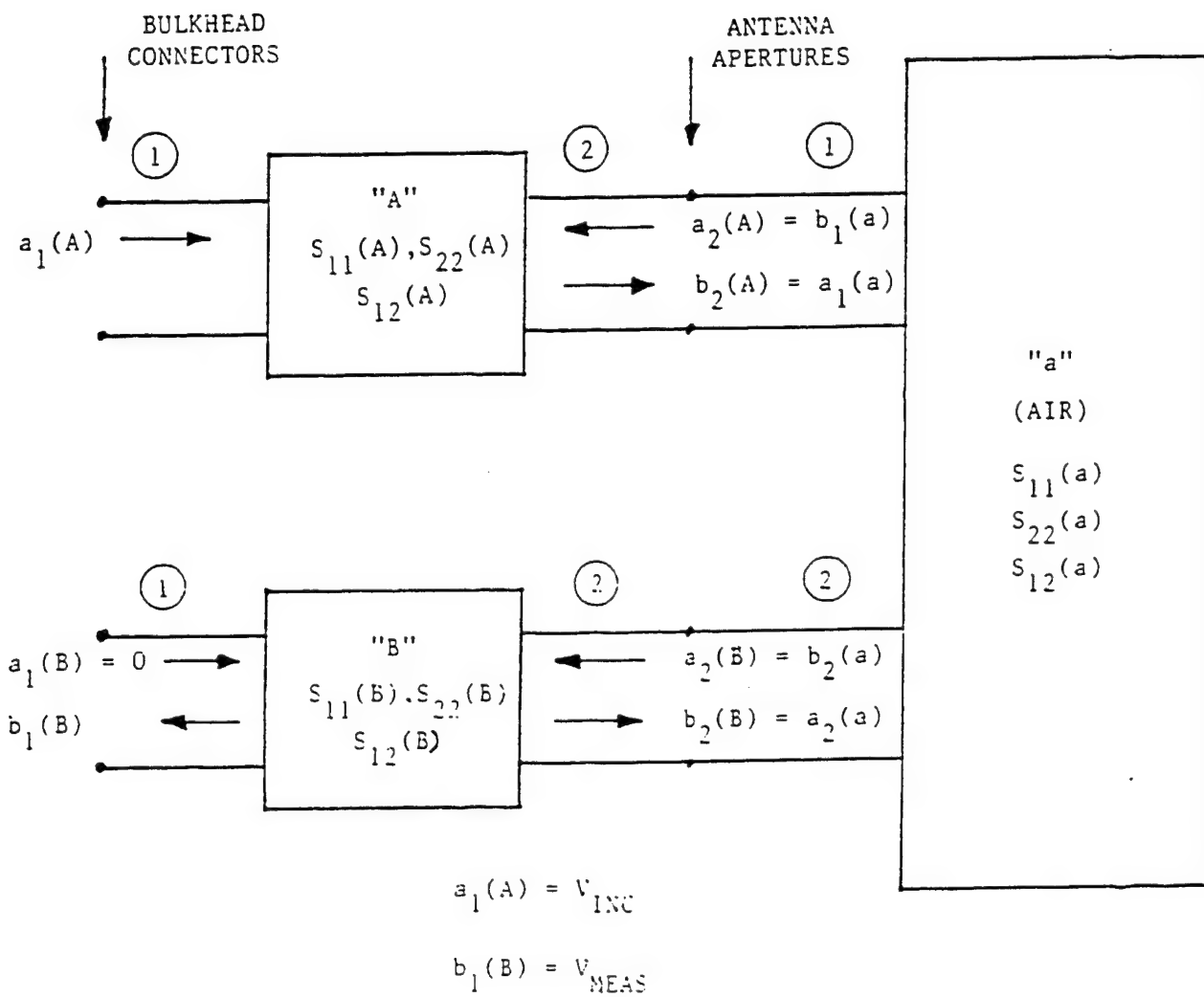


Figure A1 Antenna Coupling Configuration and Symbol Definition

Table A1
Scattering Matrix Equations for Mutual Coupling

“A” Network

$$b_2(A) = S_{12}(A) a_1(A) + S_{22}(A) a_2(A) \quad (1)$$

$$a_1(A) = V_{INC} \quad (2)$$

$$a_2(A) = S_{11}(A) b_2(A) \quad \text{Note 1 (3)}$$

$$\therefore b_2(A) = V_{INC} \frac{S_{12}(A)}{(1 - S_{22}(A)S_{11}(a))} \quad (4)$$

“B” Network

$$a_1(B) = 0 \quad \text{Note 2 (5)}$$

$$b_1(B) = S_{12}(B) a_2(B) \quad (6)$$

$$b_2(B) = S_{22}(B) a_2(B) \quad (7)$$

$$b_1(B) = V_{MEAS} \quad (8)$$

$$\therefore a_2(B) = \frac{V_{MEAS}}{S_{12}(B)} \quad (9)$$

“a” Network

$$a_2(B) = S_{22}(a) b_2(B) + S_{12}(a) b_2(A) \quad (10)$$

$$a_2(B) = S_{22}(a) S_{22}(B) a_2(B) + S_{12}(a) b_2(A) \quad (11)$$

$$S_{12}(a) = \frac{a_2(B)}{b_2(A)} (1 - S_{22}(B) S_{22}(a)) \quad (12)$$

$$S_{12}(a) = \frac{(1 - S_{22}(B) S_{22}(a))(1 - S_{22}(A) S_{11}(a))}{S_{12}(B) S_{12}(A)} \frac{(V_{MEAS})}{(V_{INC})} \quad (13)$$

APPENDIX B CONVERSION OF SHOCK TUNNEL RUN DATA TO ANTENNA APERTURE PLANES

During the shock tunnel RF experiments, received signals (I and Q components) were measured to determine:

- (a) Normal mode; the received signal amplitude and phase with an external transmit signal at about a 10° angle of arrival relative to the tunnel axis,
- (b) Coupled mode; the reflection coefficient at one antenna (antenna 2) by transmitting from antenna 2 and using a reflectometer in the feed line to the antenna, and
- (c) Coupled mode; the coupling between antenna 2 and other antennas by transmitting from antenna 2 and recording the received signals at the other antennas.

The correction factors, using the calibration procedure described in Section 3.2, required to translate the measured run data to the antenna aperture planes, are briefly discussed below.

Normal Mode

The antenna aperture voltage at the aperture plane, V_{ant} , in terms of the incident voltage on the aperture plane, V_i , and the reflection coefficient looking into the aperture, R_{ant} , is

$$V_{ant} = V_i \cdot (1 + R_{ant}) \quad (1)$$

In the original calibration procedure, R_{ant} , was determined from the scattering parameters of the antenna feed networks and reflection coefficients looking into the mixers (i.e., from measurements made at the bulkhead connectors).

In the revised calibration procedure, R_{ant} was measured directly using a network analyzer, the saddles over the antenna apertures, and a coax/WG adapter. The network analyzer was calibrated at the output flange of the coax/WG adapter using the reference waveguide loads. The instrumentation system remained connected thus including the mixer reflection coefficients in the measurement.

The receiver calibration was performed from the antenna apertures by feeding a reference signal into the antenna apertures from a well matched source and calibrating the

receivers to a constant gain for this signal. The relation of the measured voltages to the incident voltages is

$$V_{\text{meas}} = C \cdot V_i \quad (2)$$

where C is a constant voltage scaling factor for all antennas. Dropping the scaling factor C , the translation of the measured voltage for antenna i to the antenna aperture plane is provided by

$$V_{\text{ant}}(i) = (1 + R_{\text{ant}}(i)) \cdot V_{\text{meas}}(i) \quad (3)$$

Coupled Mode - Reflection Coefficient

Antenna 2 was used as a transmit antenna in the coupled mode. A directional coupler monitored the reflected signal from antenna 2 which was used to determine the reflection coefficient. Receivers on the other four antennas provided measures of the coupled signal which were reduced to provide coupling coefficients.

The end-to-end calibration of the reflectometer was performed by placing the reference waveguide loads over the antenna 2 aperture and recording the receiver 2 coupled-mode digital output. The incident voltage was monitored on a second receiver during the calibration procedure. With these data, the reflectometer correction factors $X1(R)$, $X2(R)$ and $X3(R)$ could be determined, where

$$R_a(2) = \frac{R(2) - X_2(R)}{X_1(R) - X_3(R) \cdot R(2)} \quad (4)$$

$R_a(2)$ is the reflection coefficient for antenna 2 at the aperture and $R(2)$ is the uncorrected reflection coefficient measured by the reflectometer and is proportional to the measured voltage at the receiver output connected to the reflectometer. That is

$$R(2) = V(2) \cdot C(R) \quad (5)$$

where $V(2)$ is the measured voltage in the coupled mode of the antenna 2 reflectometer, after including receiver calibration factors. $C(R)$ is a scaling constant determined by the measured initial voltage $V(2)$, defined as V_{ins} , just prior to (within a millisecond) the test run.

During this initial period data channels are recording, having been triggered by passage of the incident shock wave in the driven tube. Nozzle flow has not yet started, however, hence no plasma conditions exist around the model and the antenna is radiating under free-space conditions. The reflection coefficient of the antenna during this initial period is thus the free-space coefficient, which is measured during antenna calibration. The constant $C(R)$ is determined such that the free-space antenna aperture reflection coefficient, defined as $R(\text{fs})$, is

obtained during the initial part of the run. This procedure is required because the incident voltage varies slowly over time, which causes the reflected voltage to vary also. During the short millisecond period of a run, however, the incident voltage is constant.

The scaling constant was determined using

$$R(m) = \frac{X_2(R) + X_1(R) \cdot R(fs)}{1 + X_3(R) \cdot R(fs)} \quad (6)$$

and

$$C(R) = \frac{R(m)}{V_{init}} \quad (7)$$

where V_{init} is the receiver output voltage just prior to the test flow in the shock tunnel.

Coupled Mode - Coupling Between Antennas

The coupling between antennas was measured in the coupled mode by transmitting from antenna 2 and recording the received signal (I and Q components) at the other four antennas. There are different types of coupling which can be defined (as for the gain of an amplifier). The procedure used herein defines the coupling in terms of the ratio of aperture voltages of the receive antenna relative to the transmit antenna. Thus the coupling coefficient between receive antenna i and transmit antenna 2 is defined as

$$A(i,2) = V_{ant(i)} / V_{ant(2)} \quad (8)$$

where the voltages are at the aperture planes of the antennas. Just prior to the test, the environment is in a free-space condition and the coupling is the free-space coupling. The change in coupling relative to free-space conditions is an important parameter relative to plasma effects and is given by the ratio of the coupling during the test, $A(i,2,test)$, to the free-space coupling, $A(i,2,fs)$. This ratio is defined as

$$C(1,2) = \frac{A(i,2,test)}{A(1,2,fs)} = \frac{V_{ant(i,test)}}{V_{ant(i,fs)}} \cdot \frac{V_{ant(2,fs)}}{V_{ant(2,test)}} \quad (9)$$

The free-space condition is observed immediately prior to airflow over the model. The transmit signal is constant over the duration of a test run, as observed by the instrumentation, and thus slow variation in the incident signal will not affect the ratio defined in Eq (9).

The antenna 2 aperture voltage is

$$V_{\text{ant}}(2) = V_r(2) \cdot (1 + R_a(2)) \quad (10)$$

where $V_r(2)$ is the voltage from the source incident on the antenna 2 aperture and $R_a(2)$ is the measured reflection coefficient of antenna 2. Using the scattering parameters of the network feeding antenna 2, the $V_{\text{ant}}(2)$ can be written as

$$V_{\text{ant}}(2) = \frac{1 + R_a(2)}{1 - S_{22} \cdot R_a(2)} \cdot [S_{12} \cdot V_i(1)] \quad (11)$$

where S_{22} is the reflection coefficient at the antenna 2 aperture looking towards the source.

The network feeding antenna 2 is well isolated at the source and reflections from antenna 2 do not affect the incident voltage, $V_i(1)$. The scattering parameter S_{12} is constant during any run. Thus the term in square brackets in Eq (11) is constant during a run and factors out in forming the coupling relative to free-space.

The reflection coefficient at the antenna 2 aperture looking toward the source in the coupled mode, S_{22} , is measured during the calibration procedure.

The reduction of the run data to determine the antenna coupling relative to free-space uses Eqs (3) and (9), and the relation expressing $V_{\text{ant}}(2)$ in terms of $V_i(1)$,

$$V_{\text{ant}}(2) = \frac{S_{12} \cdot (1 + R_a(2))}{1 - S_{22} \cdot R_a(2)} \cdot V_i(1) \quad (12)$$

APPENDIX C THIN-WIRE, SWEEPED-VOLTAGE PROBE MEASUREMENTS OF ELECTRON NUMBER DENSITIES IN PLASMA FLOW FIELDS

The point determination of the electron number density, n_e , and temperature, T_e , in a moving plasma is an intrusive measurement, performed by means of a swept-voltage, thin-wire probe. Several such probes may be installed in a common rake, each probe aligned with the local flow direction, and positioned at different distances off the vehicle surface so as to measure the number density profile through the boundary layer.

A linear voltage ramp is simultaneously applied to each probe, swept over a voltage range (e.g. -5V to +3V) sufficient to record both the ion current and the electron retarding field regions of the probe characteristic. An illustrative sketch of a complete electrostatic probe characteristic is shown below.

In the interpretation of the probe characteristic, the ion current collected by the probe at a selected (non-dimensional) probe potential is used, in conjunction with the measured electron temperature, to derive the local ion number density corresponding to the collected ion current. Probe data reduction follows the theory of Laframboise (C1) for the case of a collisionless (free-molecular) sheath.

A non-dimensional probe potential, χ_p , is defined by

$$\chi_p = \frac{e}{kT_e} (V_p - V_\infty) \quad (1)$$

which is the dimensionless difference between the probe potential, V_p and the plasma potential, V_∞ . The latter is the potential at which the probe collects both ions and electrons (random currents) without the aid of electric fields. In the Eq for χ_p , e is the electron charge, k is the Boltzmann constant and T_e the electron temperature.

Laframboise's results from the collected ion and electron current densities at negative values of χ_p are written,

$$j_i = en_e \left(\frac{kT_e}{2\pi m_i} \right)^{1/2} i_+ \quad (2)$$

$$j_e = en_e \left(\frac{kT_e}{2\pi m_e} \right)^{1/2} \chi_p \quad (3)$$

where i_+ is a normalization factor representing the increase in the collected ion current over the random kinetic ion flux to the probe at $\chi_p = 0$, i.e. at the plasma potential. The factor i_+ is a function of χ_p , the ratio of the probe radius to Debye length, r_p/λ_D , and the ratio of ion to electron temperatures. The Debye length is given by

$$\lambda_D = \left(\frac{\epsilon_0 kT_e}{n_e e^2} \right)^{1/2} \approx \sqrt{\frac{T_e}{n_e}} 6.9 \text{ cm (cgs)} \quad (4)$$

When the voltage applied to the probe is swept from negative towards positive values, $\chi_p \rightarrow 0$ and the electron current collected by the probes increases rapidly because the higher thermal velocities of the electrons enable them to reach the probe surface in spite of the repelling voltage. This region of the probe characteristic is called the retarding-field region. Differentiating Eq (3),

$$\frac{d \ln j_e}{dV_p} = \frac{e}{kT_e} \quad (5)$$

i.e., the slope of a semi-log plot of retarding-field region probe current vs. probe voltage is e/kT_e , which is the basis for the determination of the electron temperature. Then

$$T_e = \frac{11600}{e/kT_e} \quad (6)$$

The ion number density is obtained from the ion-current portion of the probe characteristic at large negative values of χ_p ($\chi_p > 10$), via Eq (2). The calculation of number density from the measured ion current density is seen to involve m_i , the ion mass, hence the identity, of the collected ion. In a pure-air plasma, this may be assumed to be NO^+ . In reentry vehicle boundary layer flows, alkali-metal contaminant ionization from ablating surfaces can become a predominant free-electron source. In the case of flight diagnostic measurements, therefore, the probe voltage ramp excursion should be extended sufficiently to record the electron-sheathed region of the probe characteristic.

At positive probe potentials, the electron number density, n_e , is measured independently of the nature of the collected ion. Since $n_e = n_i$ for a neutral plasma, this can further afford a means of corroborating the identity of the ion in the flow. Such use of thin-wire electrostatic probes has been studied in shock tunnel flows (C2). Therein, the charged-particle

densities determined from the ion-sheathed and electron-sheathed portions of the probe characteristic were in good agreement with each other, and with independent microwave interferometer measurements.

In relating a χ_p to the corresponding probe potential, V_p , it can be difficult to define the plasma potential, V_∞ , from the probe characteristic with precision. Instead, the non-dimensional probe potentials can be referred to the floating potential, V_f , which is readily identifiable on each probe characteristic as the probe voltage for zero net collected current.

Thus, by equating Eqs (2) and (3) at $\chi = \chi_F$

$$e \chi_F = \left(\frac{m_e}{m_i}\right)^{1/2} i_+ \quad (7)$$

or

$$\chi_F = \frac{e}{kT_e} (V_F - V_\infty) = \frac{1}{2} \ln \left(\frac{m_e}{m_i}\right) i_+ \quad (8)$$

Since the effect on χ_F is small, i_+ is taken as unity. Then,

$$\chi_p = \frac{e}{kT_e} (V_p - V_F) + \chi_F \quad (9)$$

and

$$V_p = \frac{\chi_p - \ln(m_e/m_i)^{1/2}}{e/kT_e} + V_F \quad (10)$$

$$= \frac{\chi_p + 5.4}{e/kT_e} + V_F \quad (11)$$

for the NO^+ ion.

The ion number density cannot be obtained directly from Eq (2) because i_+ depends on r_p/λ_D which is also dependent on number density. The determination of the number density using the theory of Laframboise (C1) has followed the method of Sonin (C3) which eliminates the need for an iterative calculation. From Eq (2)

$$n_e i_+ = \frac{1}{e} \left(\frac{2\pi m_i}{kT_e}\right)^{1/2} j_i \quad (12)$$

which, following substitution for n_e in terms of the Debye length, Eq (4), can be written

$$\left(\frac{r_p}{\lambda_D}\right)^2 i_+ = \frac{r_p^2}{\epsilon_0} \left(\frac{2\pi m_i}{e}\right)^{1/2} \left(\frac{e}{kT_e}\right)^{3/2} j_i \quad (13)$$

where ϵ_0 is the vacuum permittivity (8.854×10^{-12} farad m^{-1}). As noted by Sonin, this expression is not explicitly dependent on the number density. In terms of the quantities measured using the electrostatic probes, where $j_i = I_i/2\pi\Gamma_p\lambda_D$, Eq (13) can be rewritten as

$$\left(\frac{r_p}{\lambda_D}\right)^2 i_+ = \frac{1}{\epsilon_0} \left(\frac{m_i}{2\pi e}\right)^{1/2} \frac{r_p}{l_p} \left(\frac{e}{kT_e}\right)^{3/2} I_i \quad (14)$$

$$= 25.1 \frac{r_p}{l_p} \left(\frac{e}{kT_e}\right)^{3/2} I_i \quad (15)$$

for the NO^+ ion, where I_i is the ion current (in μA) at large negative r .

From computed values of $\Gamma_p/\lambda_D^2 i_+$, the corresponding values of i_+ for given I_i are obtained from a plot of Laframboise's results (C1) for the case $T_i/T_e = 1.0$. The value of i_+ is, in fact, not very sensitive to the value for T_i/T_e (C1). Therefore, once e/kT_e is determined from the probe characteristic (Eq (5)), the probe potential corresponding to the selected negative χ_p is evaluated from Eq (11). The value of $\Gamma_p/\lambda_D^2 i_+$ is calculated using Eq (15) and the corresponding value of i_+ is obtained from plots of $\Gamma_p/\lambda_D^2 i_+$ vs i_+ at selected χ_p . The ion number density is then determined as

$$n_i = \frac{1}{e^{3/2}} \left(\frac{m_i}{2\pi}\right)^{1/2} \left(\frac{e}{kT_e}\right)^{1/2} \frac{1}{r_p l_p} \frac{I_i}{i_+} \quad (16)$$

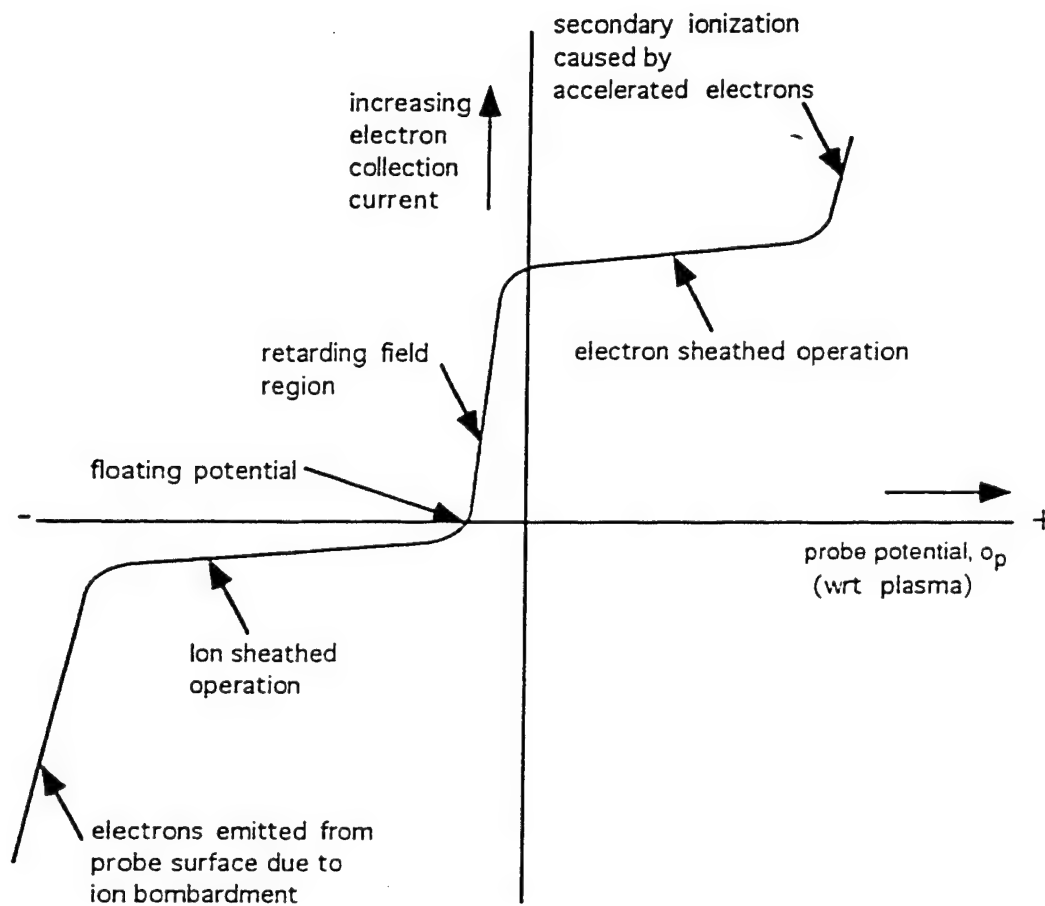
$$n_i = 1.4 \times 10^7 \left(\frac{e}{kT_e}\right)^{1/2} \frac{I_i}{i_+} \frac{1}{r_p l_p} \text{ cm}^{-3} \quad (17)$$

for NO^+ and I_i μA , Γ_p/λ_D in cm^2 .

The slope measurement for the determination of e/kT_e should be made at a point where the ion current is negligible. It has been shown (C3) that the net current to the probe is essentially equal to the electron current when the latter is about twice the ion current collected at large negative χ_p . In the reduction of the electrostatic probe data from these experiments, the ion

currents employed were for probe potentials corresponding to non- χ_p values of -15 and -20. The slope of the semilog I_p vs. V_p plots were then evaluated at probe current at least twice the magnitude of the ion currents measured at the χ_p values. This procedure is illustrated in Figure C-1 for one of the probe locations shown in Figure 26 of the text.

- C1. Laframboise, J.G., Theory of Spherical and Cylindrical Langmuir Probes in a Collisionless, Maxwellian plasma at Rest. UTIAS Report 100, March 1966. Also Proc. Fourth International Symposium on Rarefield Gas Dynamics, Volume 2, p. 22 (1966). Ed. J.H. deLeeuw.
- C2. Dunn, M.G., Use of positively Biased Electrostatic Probes to Obtain Electron Density in Collisionless Flows. AIAA J. 10, 996, August 1972.
- C3. Sonin, A.A., The behavior of Free Molecule Cylindrical Langmuir Probes in Supersonic Flows, and Their Application to the Study of the Blunt Body Stagnation Layer. UTIAS Report 109, August, 1965.



Sketch of the complete probe characteristic
(ion current exaggerated)

Figure C-1 Sketch of the Complete Ion Probe Characteristic

APPENDIX D BOWSHOCK RADIATION STUDY

In addition to the electron density measurements, spectroradiometric and radiometric measurements of the model nose gas cap radiation were obtained. Figure D-1 shows a schematic of the experimental arrangement. A 1 inch diameter quartz lens collects the radiation and transfers it to a 1 mm diameter quartz fiber optic cable. This lens is mounted near the top of the test section approximately 36 inches from the model nose.

On an optical table outside the test section, the fiber optic cable introduces the light as a parallel beam into a housing that distributes the radiation. The first beam splitter directs 90% of the light toward a grating spectrograph and the Optical Multi-channel Analyzer (OMA) detector. The remaining 10% is further divided among 3 photomultiplier tubes (PMT) by two 50/50 beam splitters. Each PMT has an optical filter placed in front of it to define an optical bandpass. For runs 1 through 14, the optical filters defined a bandpass for nitric oxide (NO), the hydroxyl radical (OH), and the alpha line of atomic hydrogen (H_2). For runs 15 through 33 the NO filter was replaced with a filter appropriate for observing copper (Cu) radiation. The NO filter has a full width at half-maximum (FWHM) of 1.64 nm centered at 303.5 nm. This bandpass would include the strong double-headed $NO\beta$ band at 303.5 nm and 304.3 nm. The OH filter has a FWHM of 1.69 nm centered at 307.4 nm. This bandpass encompasses the strong (0,0) bandhead of the 306.4 nm system. The Cu filter has a FWHM of 2.85 nm centered at 326.5 nm. This bandpass includes the atomic resonance lines at 324.8 nm and 327.4 nm. The H_2 filter has a FWHM of 1.05 nm and is centered at 656.4 nm. The H_2 line radiates at 656.3 nm. Since neither NO or H_2 were observed to be strong radiators in the present experiment, their filter bandpasses provided a time history of continuum radiation or of scattered radiation. OH and Cu, however, were found to be the dominant radiators.

The output from the three PMT radiometers are recorded on the Digital Data Acquisition System (DDAS) while the OMA spectra is recorded on a PC. The OMA spectra are integrated over a 0.5 msec interval which is indicated by a pulse recorded on DDAS. This integration time can be chosen to occur anywhere during the test, but the usual period was during steady-state test time.

The field-of-view (FOV) defined by the collection optics was a circular spot about 0.9 inches in diameter. The model projected a shadow onto this FOV that extended in about 1/4 inch on the diameter. This FOV and its location relative to the model then defines the

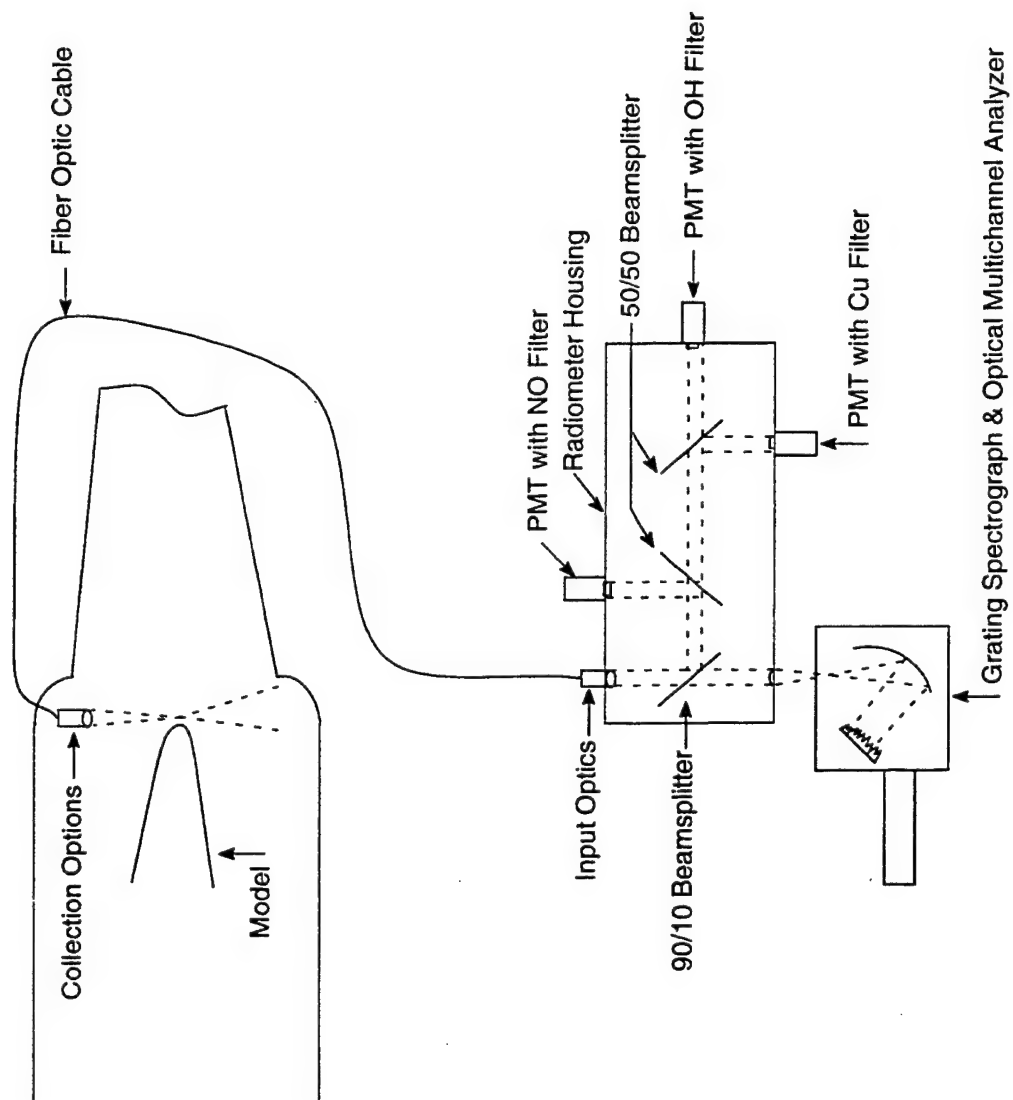


Figure D-1 Experimental Arrangement for Gas Cap Radiation Measurement

radiating volume observed. Assume that the radiating gas extends 3 mm from the surface of the model and that the chord across the FOV defined by the model is 19 mm long. The depth of the radiating gas will be taken to be 12 mm. Thus, the radiating gas presents an area given by

$$A_{\text{RAD}} = 3 \text{ mm} \times 19 \text{ mm} = 57 \text{ mm}^2$$

and a volume of radiators given by

$$V_{\text{RAD}} = 57 \text{ mm}^2 \times 12 \text{ mm} = 684 \text{ mm}^3 = 0.684 \text{ cm}^3$$

The area and volume are simply estimates. There are temperature gradients within the flowfield sampled by the FOV that certainly affect the density of radiators. Perhaps this volume is representative to within a factor of 2.

The PMT based radiometers provide temporal data at a fixed wavelength while the OMA provides spectral data at a fixed time interval. The OMA data will be discussed first followed by the radiometer data.

Before the experiments were begun, the OMA system was calibrated in spectral radiance through the use of a standard tungsten filament lamp and a deuterium irradiance source. The wavelength region calibrated was 280 nm to 340 nm. This calibration procedure has been described previously.

Figure D-2 shows a typical spectrum obtained. Except for the OH molecular band radiation, most features appear atomic in nature. Possible line identifications are noted on the Figure along with arc or flame intensities given by Refs. 1 and 2. These intensities are consistent within a given element but not from one element to another. It appears that Cu, Fe, and Ni are key contributors to the radiation in addition to the OH. The relative intensities of the molecular and atomic radiation change as the model angle of attack is changed.

In an attempt to determine whether CuO was present, the OMA spectral range was adjusted to cover the 530 nm to 640 nm wavelength region. The resulting spectrum is shown in Figure D-3. The spectrum is dominated by the Na doublet.

Na is an ubiquitous contaminant, so its presence is not unexpected. Figure D-4 is a more detailed look at Figure D-3, where the Na signal is now off scale and the underlying radiation is more prominent. The atomic lines appear to be Cu and Fe. Near the wavelength scale is a depiction of where the FeO, CuO, and CuOH molecular radiation would be and its

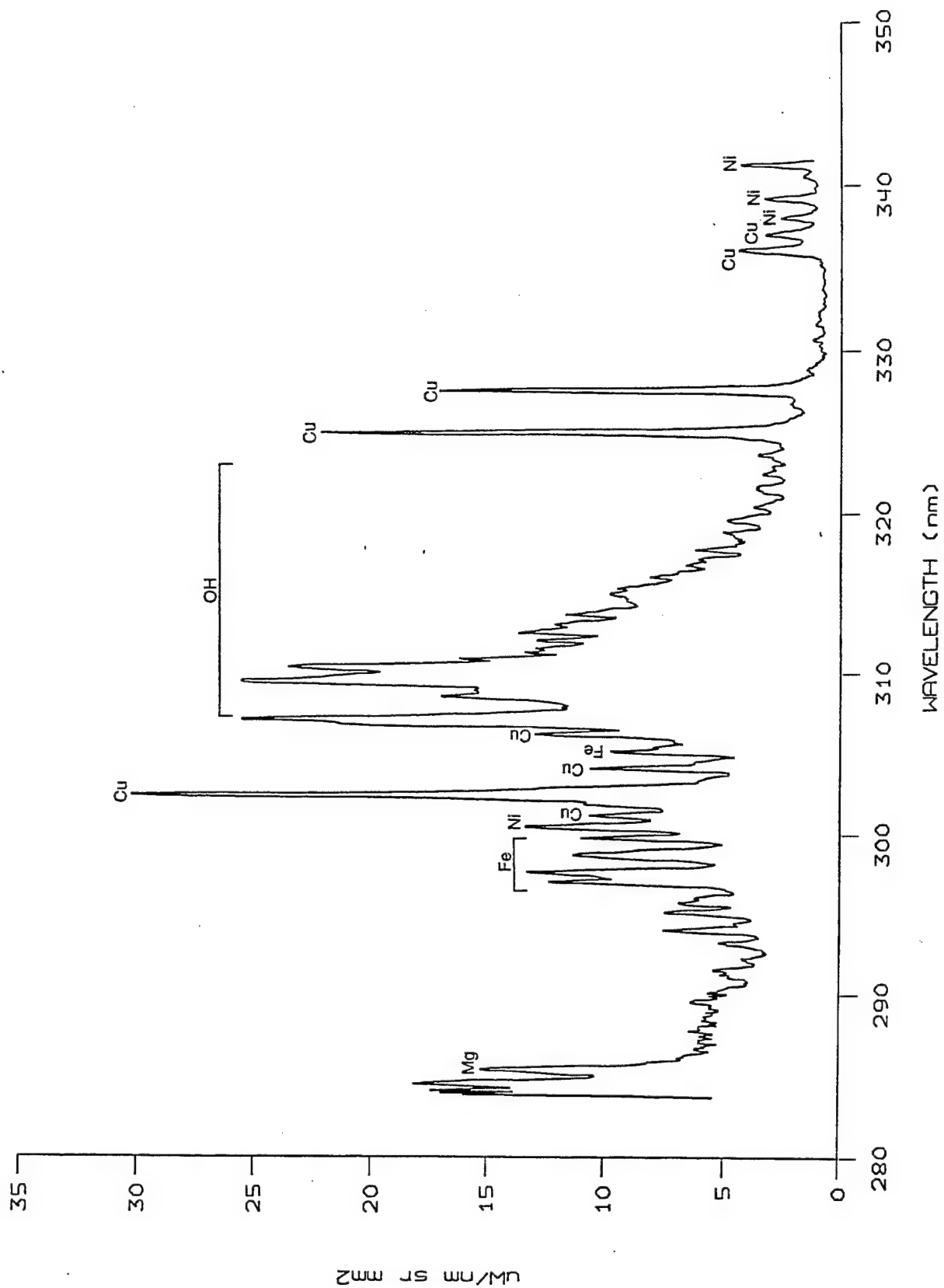


Figure D-2 UV Spectra Illustration OH and Cu, Test Run 12

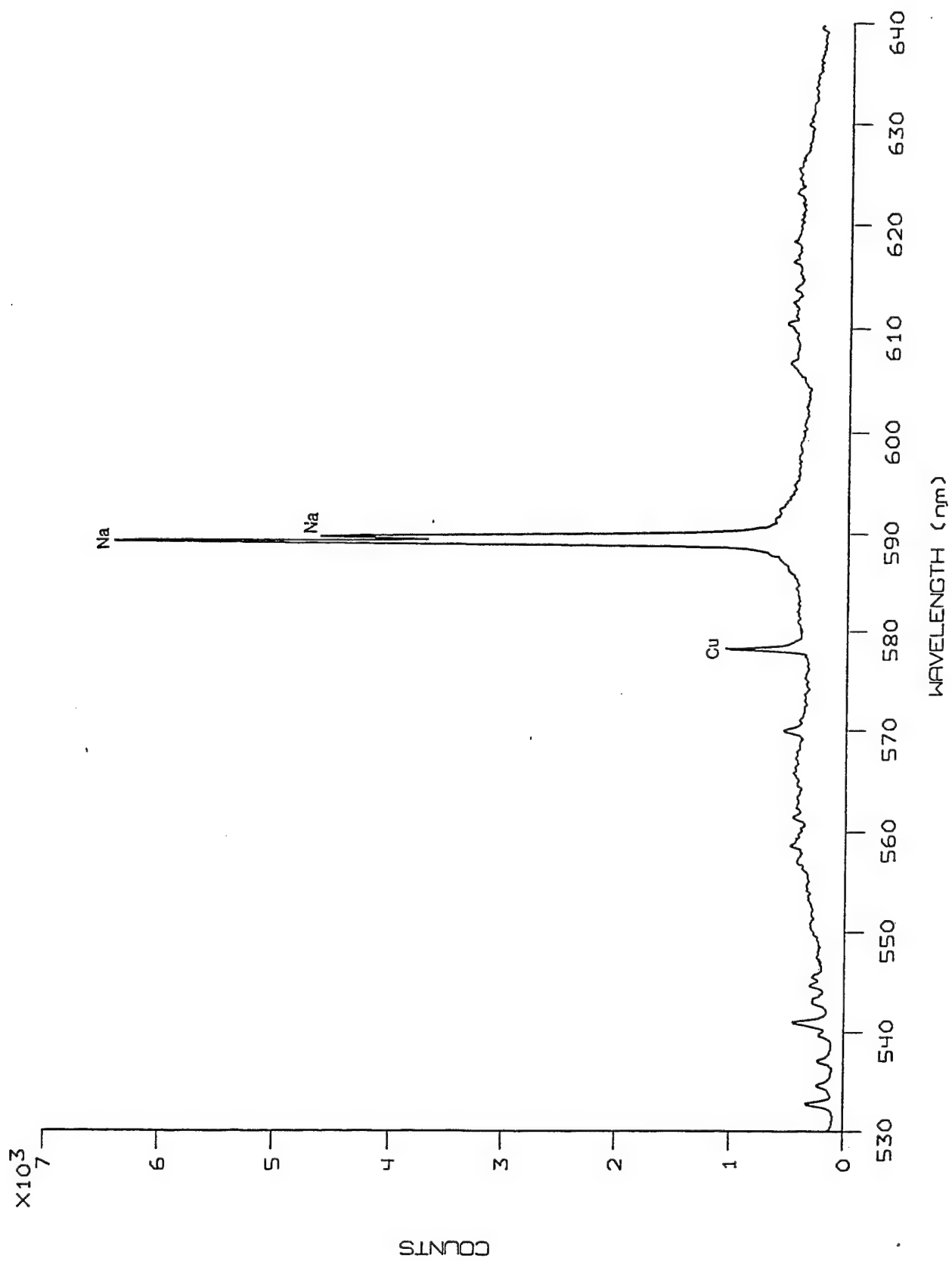


Figure D-3 Spectra Measurements of Na and Cu, Test Run 23

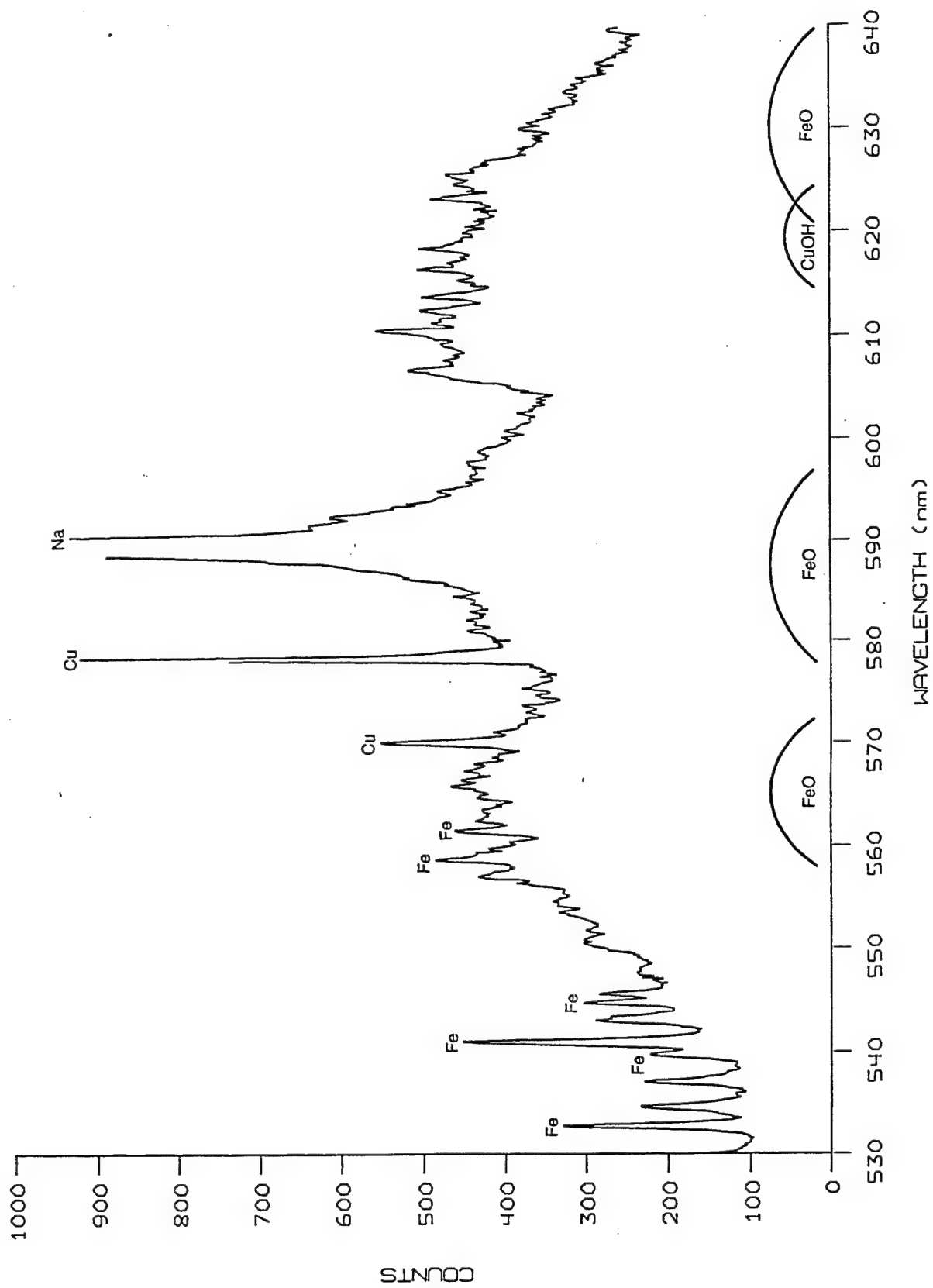


Figure D-4 Spectral Measurements of Na and Cu, Test Run 23

approximate structure. FeO appears in three main bands that in flames are a complex mixture of headless maxima and heads shaded to the red. CuO appears in double headed bands shaded to the red while CuOH is continuous radiation from 615 nm to 625 nm peaked at 620 nm. Although not unambiguous, it appears that the weak molecular radiators FeO, CuO, and CuOH are radiating in the yellow region of the spectrum.

With the OMA calibrated in the UV wavelength region, it should be possible to calculate the number density of Cu radiators from the line emission. However, in the UV region, there are only two Cu lines that are uniquely identified without overlap by other atomic or molecular radiators. These Cu transitions at 324.75 nm and 327.36 nm are the strong resonance lines for the neutral Cu atom. Since these are resonance lines, their recorded intensities are modified by any absorption by ground state Cu between the radiating source and the collection optics. For the present experimental arrangement this path length is approximately three feet. Thus, the resonance line radiation is probably compromised and not a reliable source for a number density calculation.

In the yellow region of the spectrum, as shown in Figure D5, there is a Cu atomic line that is uniquely identified near the Na doublet. This transition at 578.21 nm has an excited state for its lower level and thus, not susceptible to absorption by ground state Cu. The problem in the yellow region of the spectrum is that the OMA is not calibrated in spectral radiance. To obtain an approximate Cu number density, this problem can be mitigated.

Figure D-5 shows a yellow region spectrum that was obtained without an order sorting filter in place to prevent the UV spectrum from appearing in second order. Thus, the UV spectral lines dominate this recorded spectrum. Comparing Figure D-4 with Figure D-5, very similar line structures are seen at the longer wavelengths. However, the Na doublet is clearly distinguishable at 589.4 nm and 589.71 nm in Figure D-5, the yellow region of the spectrum. Since the UV gas cap radiation is already known in units of spectral radiance, the yellow region spectral radiance can be derived by its comparison to the UV. What is needed for this comparison are the wavelength corrections for the instrument response difference between UV and yellow light. These major differences are in the transmission of the fiber optic cable, the dispersion efficiency of the grating, and the response of the detector. Assumed negligible are mirror reflectivities, lens variations, order sorting filter transmission, and run-to-run variability. The following quantifies this general approach.

Ultimately, we want the spectral radiance of the Cu line at 578.21 nm which is not clearly distinguishable in Figure D-5. Since the Na line at 589.71 nm is nearby in

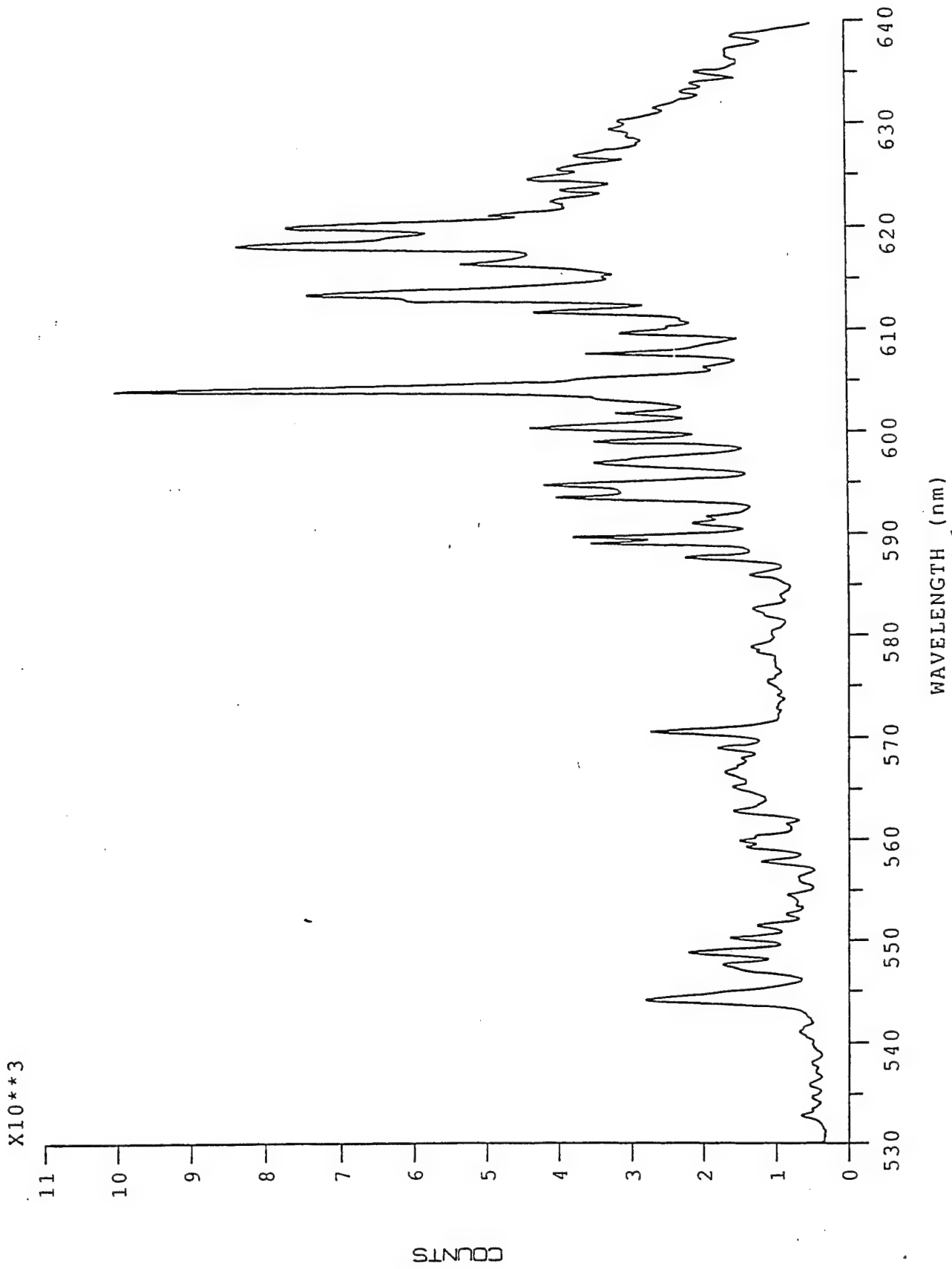


Figure D-5 Spectral Measurements, Test Run 22

wavelength and clearly distinguishable, we choose to work with it. For the nearby UV line choose 594.87 nm (second order of 297.43 nm). From Run 21, Figure D-6, a run with similar test conditions, the 297.43 nm line has an observed spectral radiance of 10 $\mu\text{w}/\text{nm sr mm}^2$ at its peak. The Na peak height is 85% of the UV peak height so that the uncorrected Na spectral radiance is

$$R_{590}^{\text{unc}} = (.85) (10) = 8.5 \mu\text{w}/\text{nm sr mm}^2$$

The fiber optic cable is 9 m in length. The UV transmission is 85%/m for a total transmission of 23%. The visible transmission is 99%/m for a total transmission of 91%. The difference is a factor of 4 greater transmission of yellow light. So the Na radiation corrected for the fiber optic becomes

$$R_{590}^{\text{c.f.o.}} = \frac{8.5}{4} = 2.1 \mu\text{w}/\text{nm sr mm}^2$$

since the radiating source is 4 times weaker to generate a similar signal.

The spectrometer grating efficiency is 35% in the UV as opposed to 60% in the yellow. A factor of 1.7 more efficient in the yellow. The detector response is a factor of 1.5 greater in the yellow than in the U.V. The corrected Na spectral radiance is then,

$$R_{590} = \frac{2.1}{(1.7)(1.5)} = 0.82 \mu\text{w}/\text{nm sr mm}^2$$

In run 23, the order sorting filter was in place so that the first order spectrum for the yellow wavelength range is clear. The test conditions for run 23 are slightly different than those for run 22. The Na 589.8 nm line is increased in signal height by a factor of 1.75. Thus, the source spectral radiance must be increased by the same factor

$$R_{590}^{23} (1.75) (0.82) = 1.44 \mu\text{w}/\text{nm sr mm}^2$$

The adjacent Cu line of interest has a peak height a factor of 0.17 of that of the Na. Thus, the 578.21 nm Cu line spectral radiance is

$$R_{578} = (.17) (1.44) = .245 \mu\text{w}/\text{nm sr mm}^2$$

With the observed line half-width of 0.7 nm, the Cu line radiance is

$$L_{578} = (0.7) (.245) = .172 \mu\text{w}/\text{sr mm}^2$$

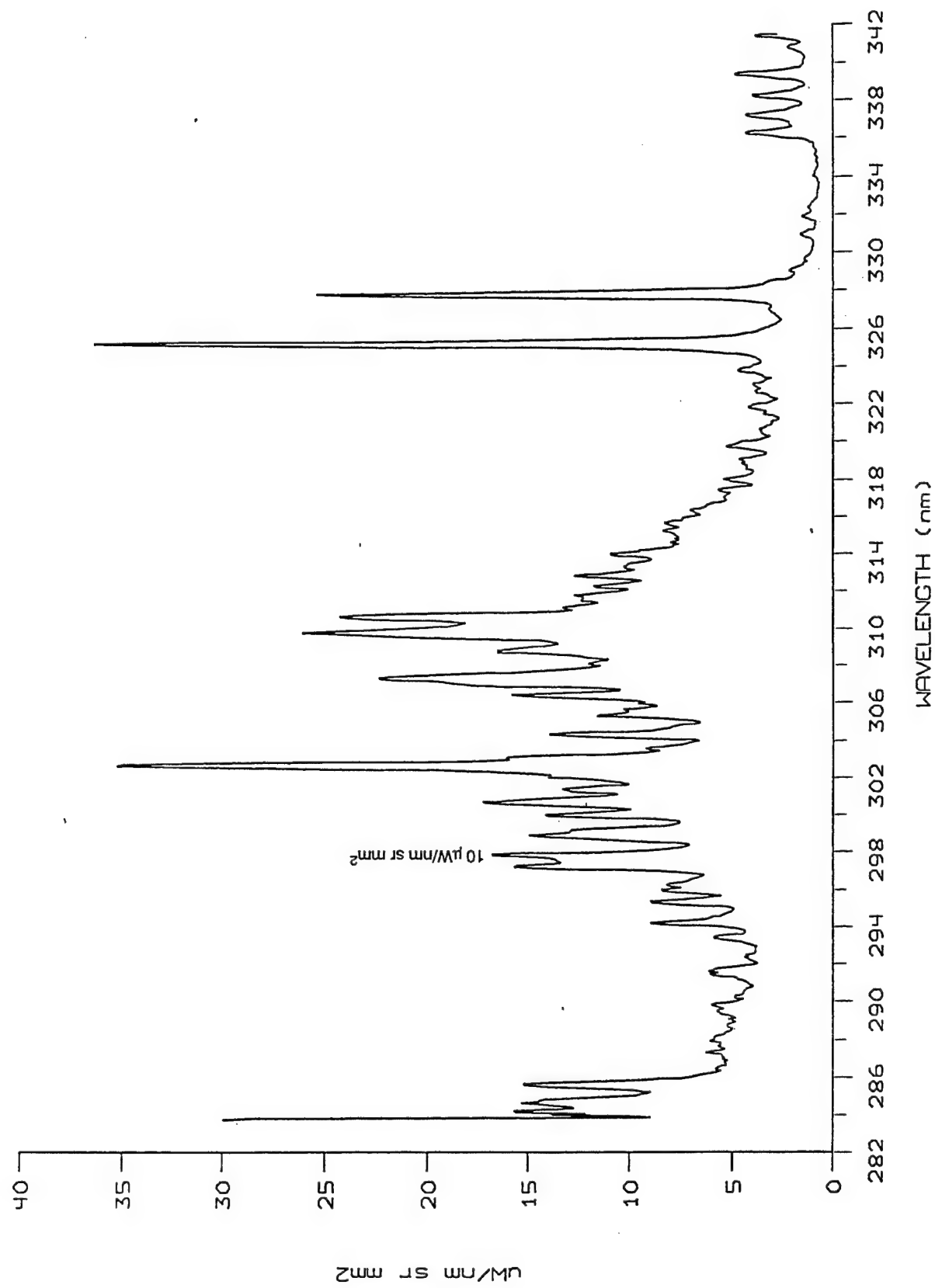


Figure D-6 Calibrated Spectral Measurements, Test Run 21

and with a radiating source area of 57 mm², the Cu line radiant intensity is

$$I_{578} = (57) (.172) = 9.78 \mu\text{w/sr} = 9.78 \times 10^{-6} \text{w/sr}$$

From reference 2, the emission intensity of N_i radiators is given by

$$I_{\text{em}} = \frac{8\pi^2 e^2 h}{m \lambda^3} N_i f_{ij}$$

where the radiation is emitted in all directions.

In units other than cgs, this becomes :

$$I_{\text{em}} = \frac{2\pi e^2 h}{\epsilon_0 m \lambda^3} N_i f_{ij}$$

where e = electron charge
 h = Planck's constant
 ϵ_0 = permittivity of vacuum
 m = electron mass
 λ = transition wavelength
 f_{ij} = emission f-value

Radiant intensity is obtained by describing the emission intensity per unit solid angle. Since I_{em} is radiating into 4π steradians

$$I = \frac{e^2 h}{2\epsilon_0 m \lambda^3} N_i f_{ij} \quad \text{in units of watts/sr}$$

with appropriate values

$$I = 1.055 \times 10^{-30} \frac{N_i f_{ij}}{\lambda^3} \quad \text{where } \lambda \text{ is in m}$$

For the 578.21 nm Cu line, ref 2 lists

$gf = 0.027$
 $E_i = 3.786 \text{ eV}$
 $E_j = 1.642 \text{ eV}$

The gf-value is the state degeneracy times the emission f-value. Since $g = 2J + 1$ where J is the electron spin quantum number, for the Cu upper level i, a $^2P_{1/2}$ state,

$$g_i = 2(1/2) + 1 = 2$$

Thus,

$$f_{ij} = \frac{0.027}{2} = 0.013$$

E_i is the energy level of the Cu transition upper state and E_j the energy level of the Cu transition lower state.

Thus, the calculated Cu line radiant intensity is

$$I_{578} = (1.055 \times 10^{-30}) \frac{(0.013)}{(578.21 \times 10^{-9})^3} N_i = 7.09 \times 10^{-14} N_i$$

With the measured radiant intensity given by

$$I_{578} = 9.78 \times 10^{-6} \text{ watts/sr}$$

The number of radiators is

$$N_i = \frac{9.78 \times 10^{-6}}{7.09 \times 10^{-14}} = 1.38 \times 10^8$$

With a radiating volume of 0.684 cm^3 , the number density of radiators is

$$N_{578} = \frac{1.38 \times 10^8}{0.684} = 2.02 \times 10^8 \text{ cm}^{-3}$$

Since the radiating gas is assumed to be in thermal equilibrium at a temperature of 6000 K, the total number density of Cu atoms, N_{Cu} , is given by the Boltzmann relation

$$\frac{N_{578}}{N_{\text{Cu}}} = \frac{g_i e^{-E_i/kT}}{\sum g_j e^{-E_j/kT}}$$

where the summation over j is over all levels of the Cu atom distribution. At $T = 6000 \text{ K}$, the significant levels are the ground state and the two $^2D_{1-1/2, 2-1/2}$ levels near 1.5 eV. The number density of Cu atoms then becomes :

$$N_{\text{Cu}} = N_{578} \frac{(2 + 6e^{-\frac{1.389}{0.52}} + 4e^{-\frac{1.64}{0.52}})}{2e^{-\frac{3.786}{0.52}}}$$

where the 2 in the numerator represents the multiplicity and degeneracy of the ground state, $E_{2D_{3/2}} = 1.389$ eV, $E_{2D_{5/2}} = 1.64$ eV, $E_{578} = 3.786$ eV, and $kT = 0.52$ at 6000 K.

$$N_{\text{Cu}} = N_{578} (1.877 \times 10^3)$$

$$N_{\text{Cu}} = (2.02 \times 10^8) (1.877 \times 10^3) = 3.79 \times 10^{11} \text{ cm}^{-3}$$

The Boltzmann distribution law is also valid for the ionization level. For Cu the ionization level is at 7.726 eV. With the Boltzmann relation now written as :

$$\frac{N_i}{N_j} = \frac{g_i e^{-E_i/kT}}{g_j e^{-E_j/kT}}$$

N_i will be taken to be the number density of ions or electrons and N_j will be taken to be the number density of Cu atoms in the upper level of the 578 nm transition or N_{578} . Thus

$$N_e = (2.02 \times 10^8) \frac{e^{-\frac{7.726}{0.52}}}{2e^{-\frac{3.786}{0.52}}}$$

$$N_e = 1.03 \times 10^5 \text{ cm}^{-3}$$

Bowshock Radiation

This electron number density resulting from Cu in the gas stream is insignificant when compared to the measured number densities of 10^{10} - 10^{11} in the experimental test. It is recognized that this density is calculated through a circuitous route. During future tests, more appropriate experimental data can be recorded to provide a more direct calculation. However, this "order of magnitude" calculation gives some perspective on the role of additional electron sources in the experimental test.

References

1. Tables of Spectral Lines of Neutral and Ionized Atoms, A.R. Stigantov and N.S. Iventitski, Plenum, New York 1968.
2. Flame Spectroscopy, R. Navrodineanu and H. Boiteux, John Wiley and Sons New York 1965.

APPENDIX E FLUSH-MOUNTED SURFACE ELECTROSTATIC PROBE DATA

In addition to the large database of thin-wire electrostatic electron number density measurements established in this research program, a number of surface flush-mounted electrostatic measurements were also performed. A total of six instruments were located on-board the test vehicle. These were the same instruments that were employed in a previous program conducted at S and X band RF irradiation. Reference 1 in the main body of Volume I of this report summarizes the previous research program.

The flush-mounted current-collecting probes were installed on the model at locations fore and aft of the RF antenna locations (see Fig. E-1) These probes consisted of a 0.635 cm (0.25 in) diameter brass slug mounted concentrically in a 0.127 cm (0.5 in) dielectric insert installed into the surface of the test vehicle. The inserts were machined to conform to the contour of the model surface. These probes could be used to collect a probe characteristic in much the same manner as the thin-wire probes used to measure the number density profiles. However, in this program the flush-mounted probes were primarily used for monitoring purposes under a constant bias voltage condition at -5 volts.

The milliamp measurements for the six current-collecting probes are reported in Table E-1. This data represents the average current measured over an interval in which steady flow field conditions were achieved. An analysis of this data was performed for the zero angle of attack test runs only and are reported herein. Two simple expressions were used in order to compute an electron number density in the near-field of the ion collecting probes. In order to perform this reduction process, the Navier-Stokes computations that were conducted and described earlier in this report were used for the required flow field variable inputs. Two theoretical expressions were used to reduce the data which yield results which differ approximately by a factor of two. The first expression developed by Denison (Ref. E-1) is shown in Eq. 1.

$$n_{eo} = 3.68 \times 10^{18} \frac{S_{ci} \sqrt{Re_x} \rho_o}{CU_e \rho_e} (-J_{is}) \quad (E-1)$$

where : n_{eo} = peak electron number density, particles/cm³

S_{ci} = ion Schmidt number (0.7 for laminar flow)

Re_x = local Reynolds Number at the probe location

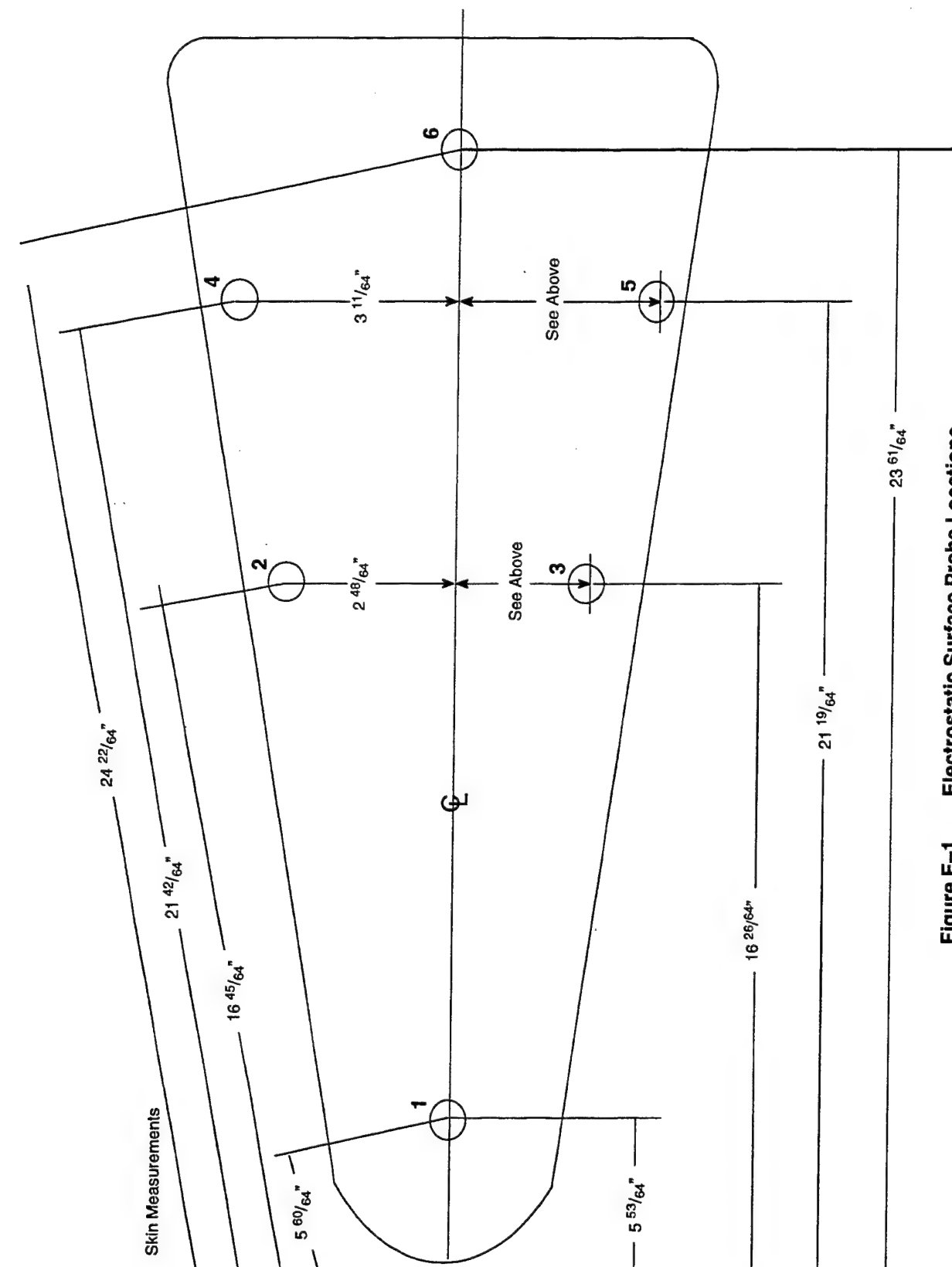


Figure E-1 Electrostatic Surface Probe Locations

Table E-1 Flush Mounted Electrostatic Probe Results

RUN NUMBER	* VEHICLE ORIENTATION			Electrostatic Probe Number					
	ATTACK	PITCH	YAW	1	2	3	4	5	6
1	0	0	0	-.0471	-.0314	-.0315	-	-.0226	-.01934
2	0	0	0	-	-.0380	-.0411	-.0273	-.02719	-.0227
25	0	0	0	-	-.0141	-.0108	-.0139	-.0097	-.0120
33	0	0	0	-	-.0120	-.0095	-.0142	-.0100	-.0115
4	2	+ 2	0	-.0380	-.0273	-.0279	-.0296	-.0213	-.0177
5	2	+ 2	0	-	-.0296	-.0309	-.0259	-.0247	-.0215
6	2	+ 2	0	-	-.0312	-.0273	-.0335	-.0238	-.0251
9	2	- 2	0	-	-.0206	-.0251	-.0194	-.0202	-.0191
10	2	- 2	0	-	-	-	-	-	-
29	2	- 2	0	-	-.0131	-.0125	-.0111	-.0106	-.0102
30	2	- 2	0	-	-.0106	-.0091	-.0113	-.0082	-.0082
13	2	0	+ 2	-	-	-	-	-	-
14	2	0	+ 2	-	-	-.0177	-.0139	-.0148	-.0138
19	2	- 1.4	+ 1.4	-.0286	-.0130	-.0176	-.0133	-.0155	-.0138
20	2	- 1.4	+ 1.4	-	-.0123	-.0179	-.0146	-.0161	-.0157
21	2	+ 1.4	- 1.4	-	-.0154	-.0178	-.0214	-.0121	-.0129
22	2	+ 1.4	- 1.4	-	-	-.0166	-.0122	-.0128	-.0125
7	6	+ 6	0	-	-	-	-	-	-
8	6	+ 6	0	-	-.0166	-.0172	-.0170	-.0138	-.0097
11	6	- 6	0	-	-	-	-	-	-
12	6	- 6	0	-	-	-	-	-	-
26	6	- 6	0	-	-.0130	-.0460	-.0135	-.0369	-.0815
27	6	- 6	0	-	-.0130	-	-.0213	-.0178	-.0184
28	6	- 6	0	-	-.0144	-.0144	-.0105	-.0111	-.0101
15	6	0	+ 6	-	-	-	-.0122	-	-.0118
16	6	0	+ 6	-	-	-	-.0108	-	-.0116
17	6	- 4.2	+ 4.2	-	-.0173	-	-.0168	-	-.0186
18	6	- 4.2	+ 4.2	-	-.0162	-	-.0137	-	-.0194
23	6	+ 4.2	- 4.2	-	-.0120	-.0116	-	-.0061	-.0078
24	6	+ 4.2	- 4.2	-	-.0145	-.0123	-.0121	-.0097	-.0090
32	13	+ 13	0	-.0078	-.0049	-.0047	-.0035	-.0023	-.0078
31	13	- 13	0	-	-	-	-	-	-
	0	SHARP	NOSE	-	-	-	-	-	-

$$C = \text{Chapman-Rubeson Parameter, } \frac{\rho\mu}{\rho_e\mu_e}$$

J_{is} = probe ion saturation current (Table E-1)

The second theory of Blankenship and Chung (Ref. E-1) is shown below in Eqn. E-2.

$$n_{eo} = 1.9 \times 10^{18} S_{ci} \left(\frac{Re}{l} \right)^{0.5} \left(\frac{1}{u_s} \right) \left(\frac{\rho_o}{\rho_s} \right) n_o (-j_{is}) \quad (E-2)$$

where : $l = \left(\frac{\mu_w \rho_w}{\mu_o \rho_o} \right)^{0.2}$

The results for several of the instruments are shown in Fig. E-2. The electron number density values are shown with regard to position measured from the nose of the test vehicle. It should be noted that the values reported at approximately the 45 and 55 cm locations are off-line from the ray of the RF antennas, but at zero angle of attack these values should be equivalent along any ray drawn from the nose along the surface of the test vehicle. The major feature of these data may be that the magnitude of the number density is in relatively good agreement with the number densities observed with the thin-wire profile measurements. A further effort is required to perform a more comprehensive study of these data which would necessitate Navier-Stokes computations of the vehicle flow field at angle of attack to provide the variables required to calculate the number density values at the other test vehicle orientations.

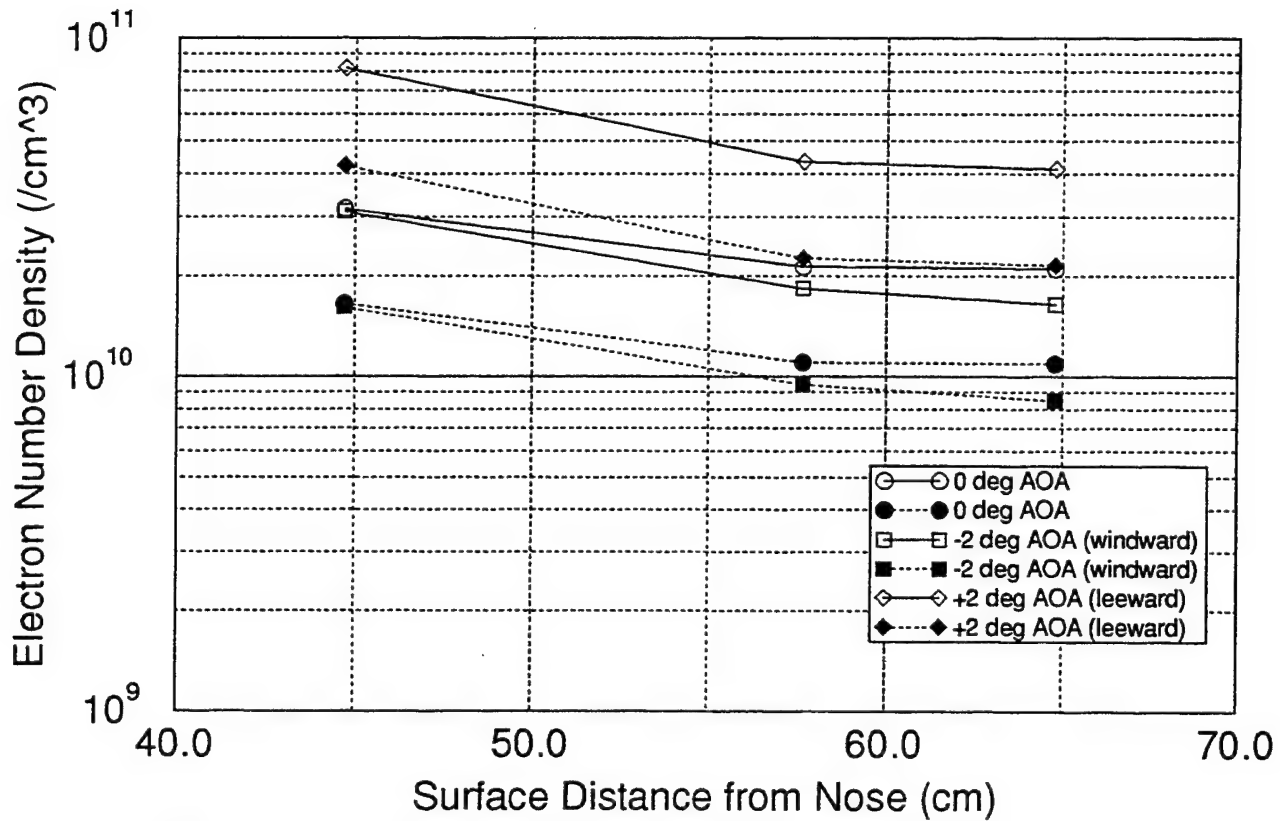
REFERENCES

E-1. Lien, H. et al, "RANT E-s Probe Experiment Preliminary Design," Avco Report AVSD-0120-70-CR, Rev. A, (June 1970).

E-2. Chung, P. M., and Blankenship, V. D., "Approximate Analysis of an Electrostatic Probe for Electron Density Measurements on Reentry Vehicles," J. Space Craft, Vol. 3, No. 12 (1966).

E-3. Denison, M. R., "Analysis of Flush Electrostatic Probes for Reentry Measurements," TRW Report 06488-6065-R000, (September 1967)

Electrostatic Surface Probe Data



NOTES :

Open symbols denote theory of Blankenship and Chung
 Closed symbols denote theory of Denison

Figure E-2 Electrotatic Probe Data Summary

APPENDIX F

THIN WIRE ELECTROSTATIC PROBE DATA

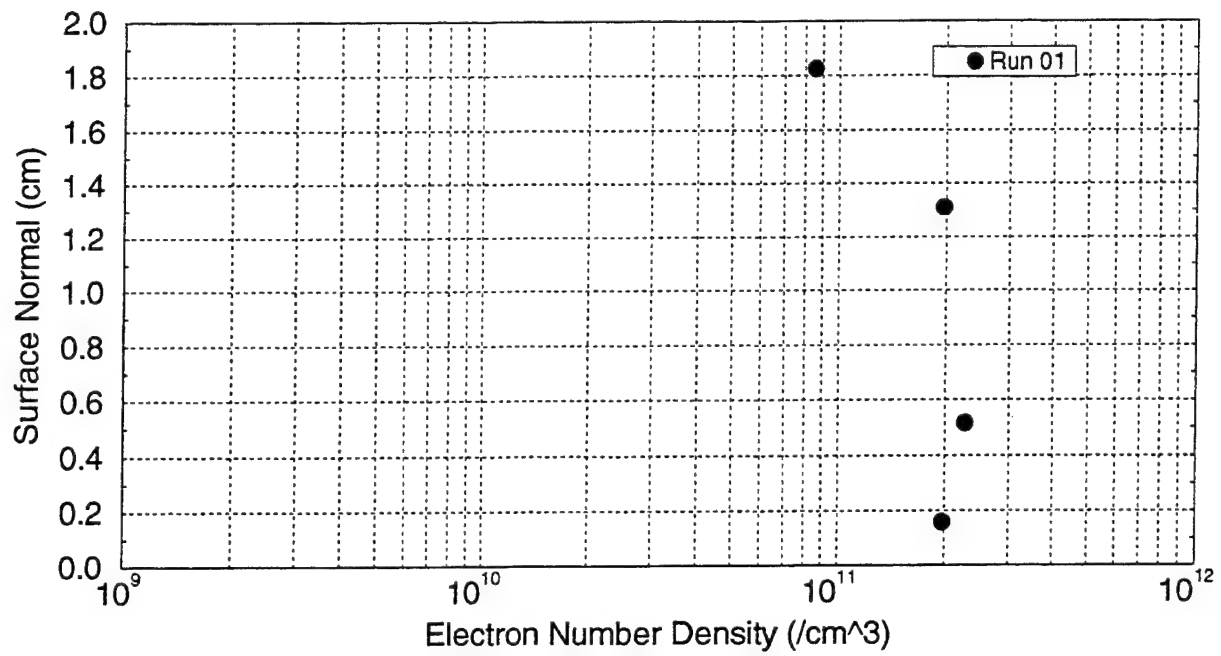


Figure F-1 Electron Number Density Profile, Test Run 01

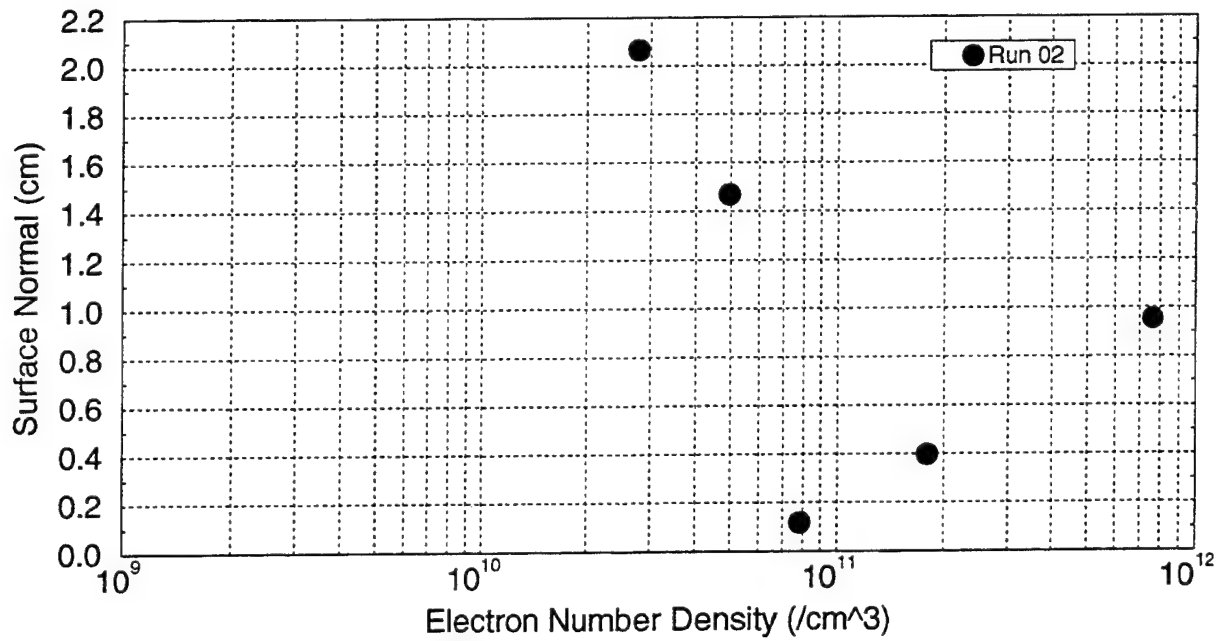


Figure F-2 Electron Number Density Profile, Test Run 02

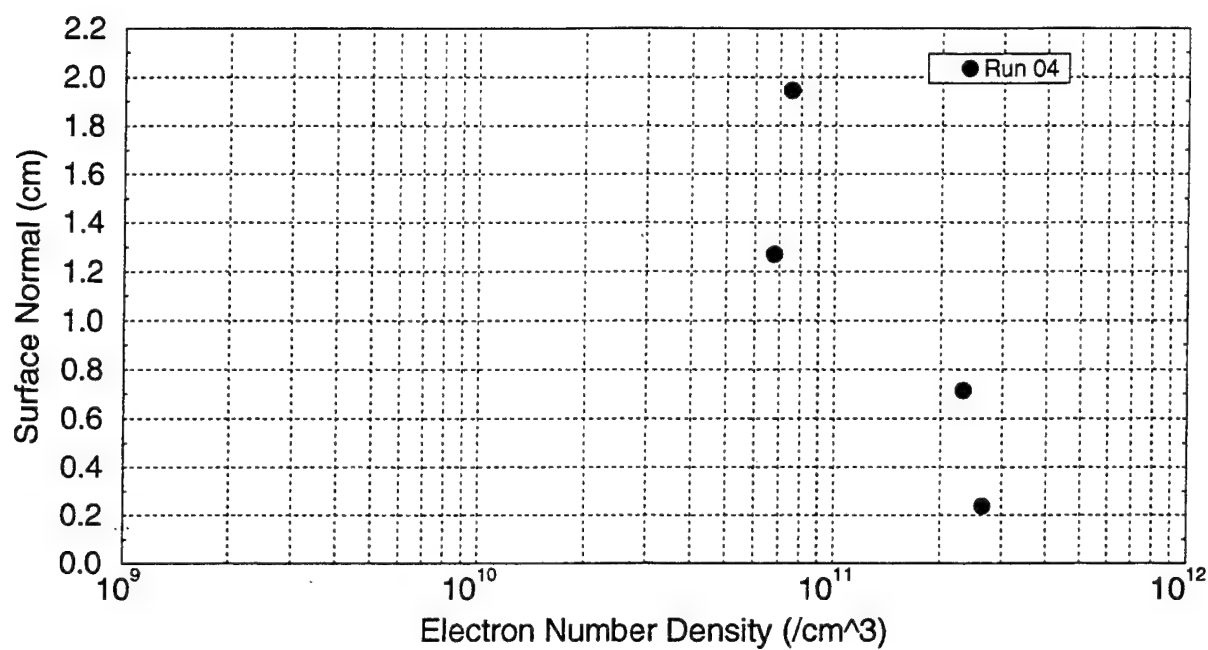


Figure F-3 Electron Number Density Profile, Test Run 04

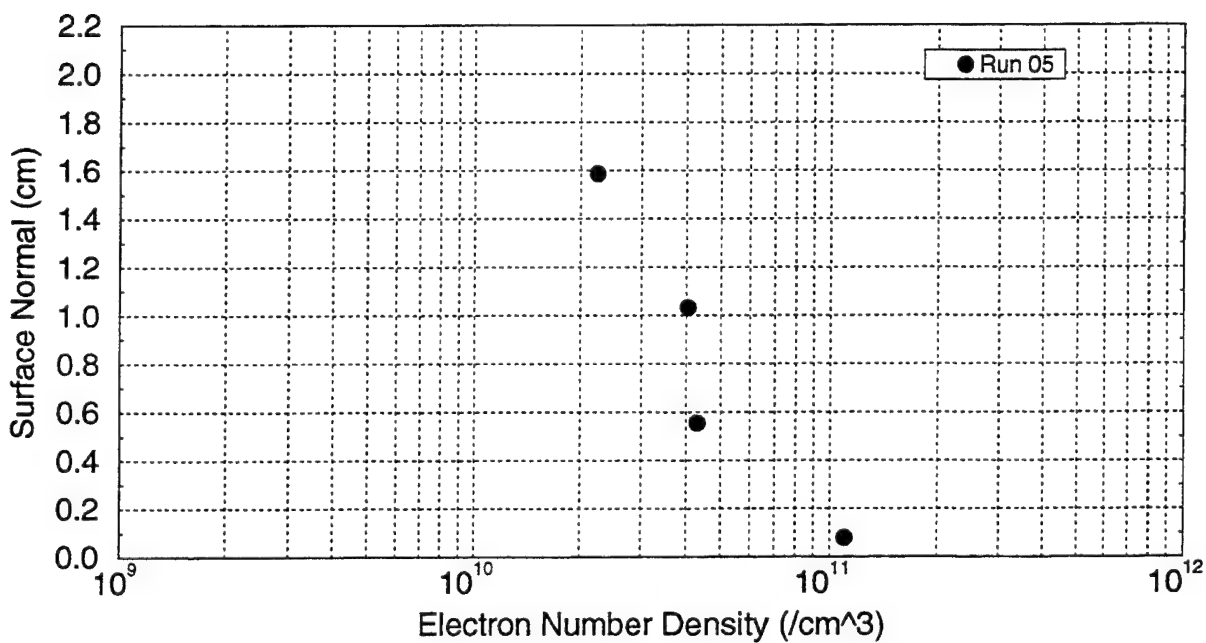


Figure F-4 Electron Number Density Profile, Test Run 05

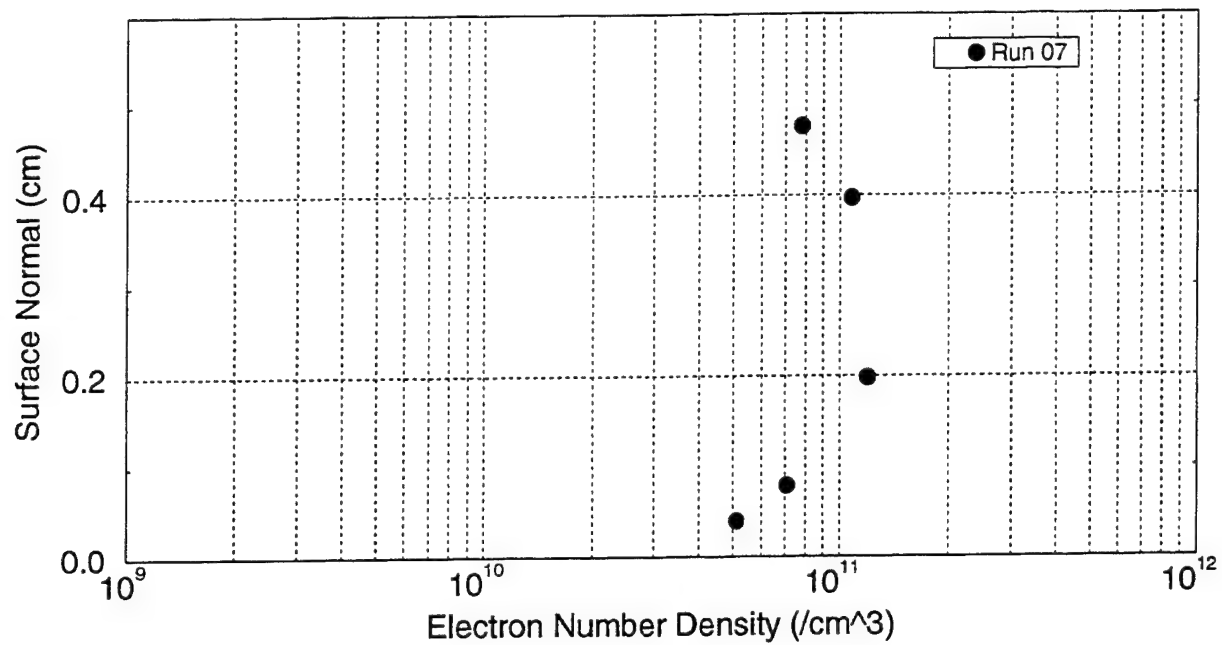


Figure F-5 Electron Number Density Profile, Test Run 07

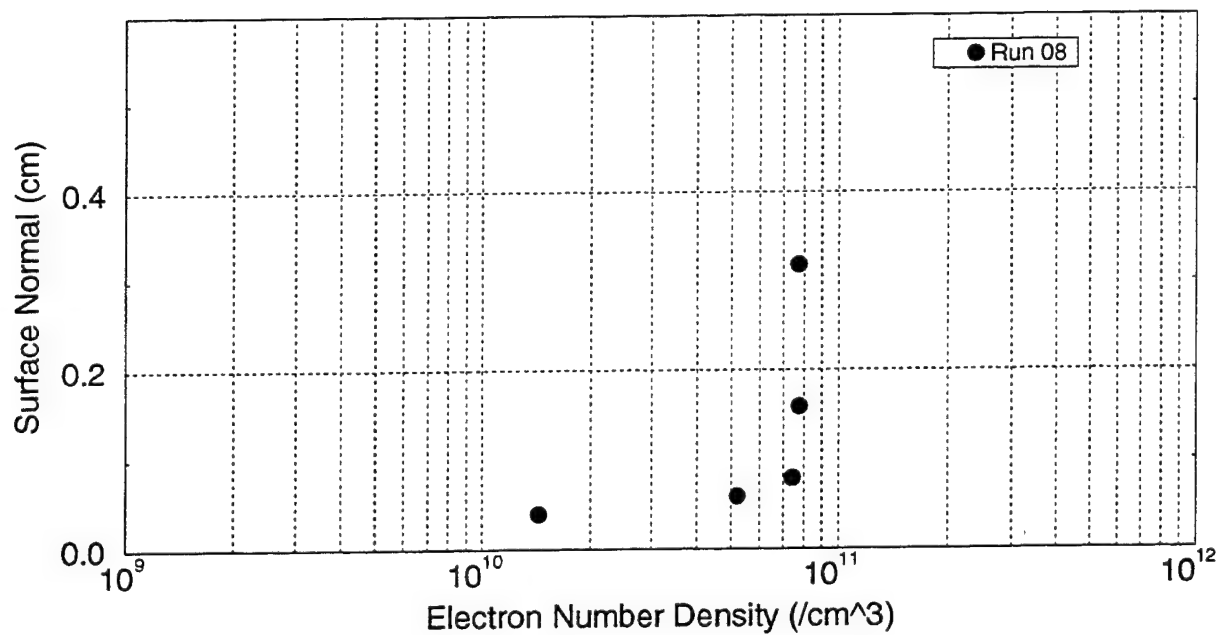


Figure F-6 Electron Number Density Profile, Test Run 08

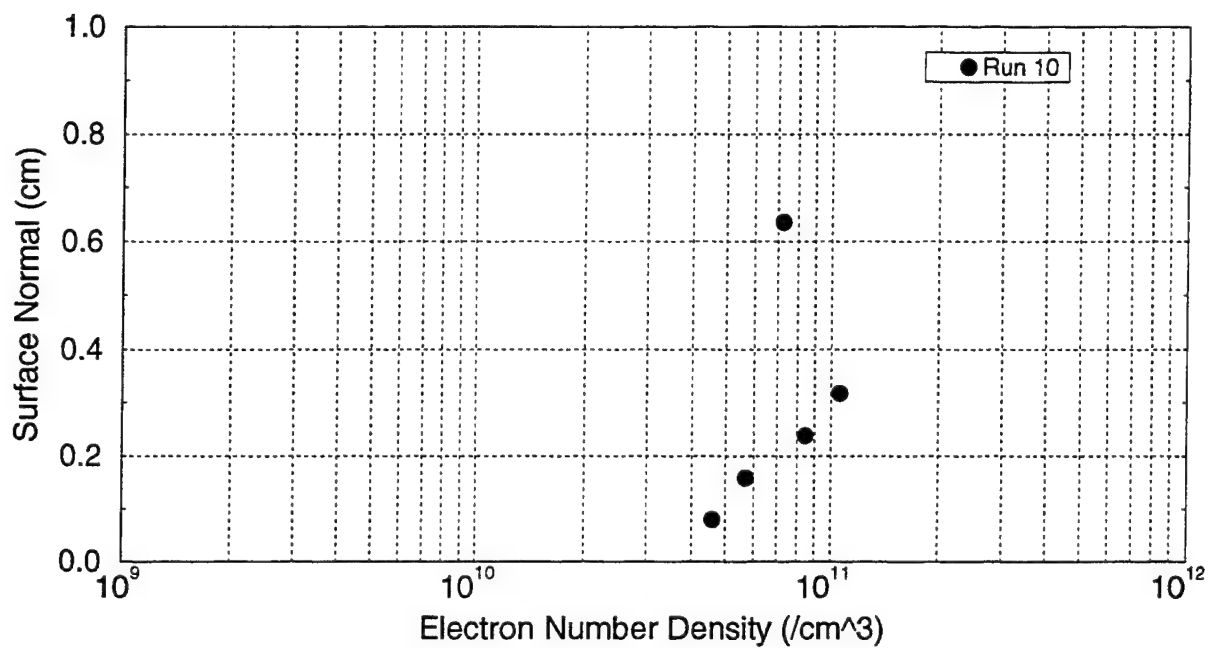


Figure F-7 Electron Number Density Profile, Test Run 10

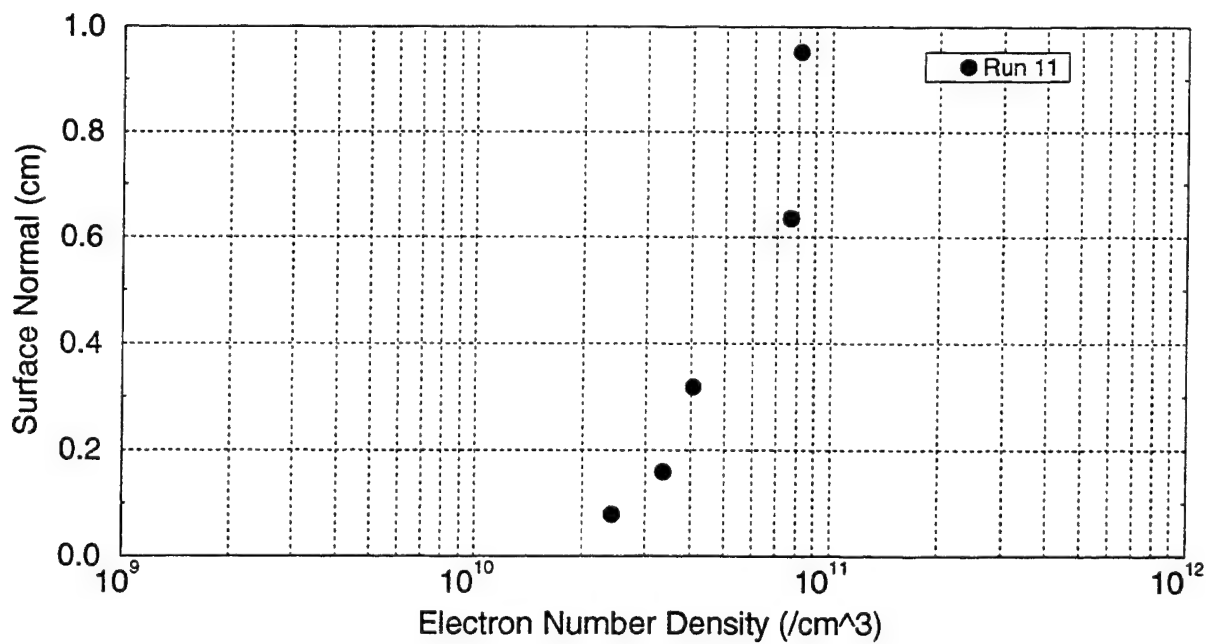


Figure F-8 Electron Number Density Profile, Test Run 11

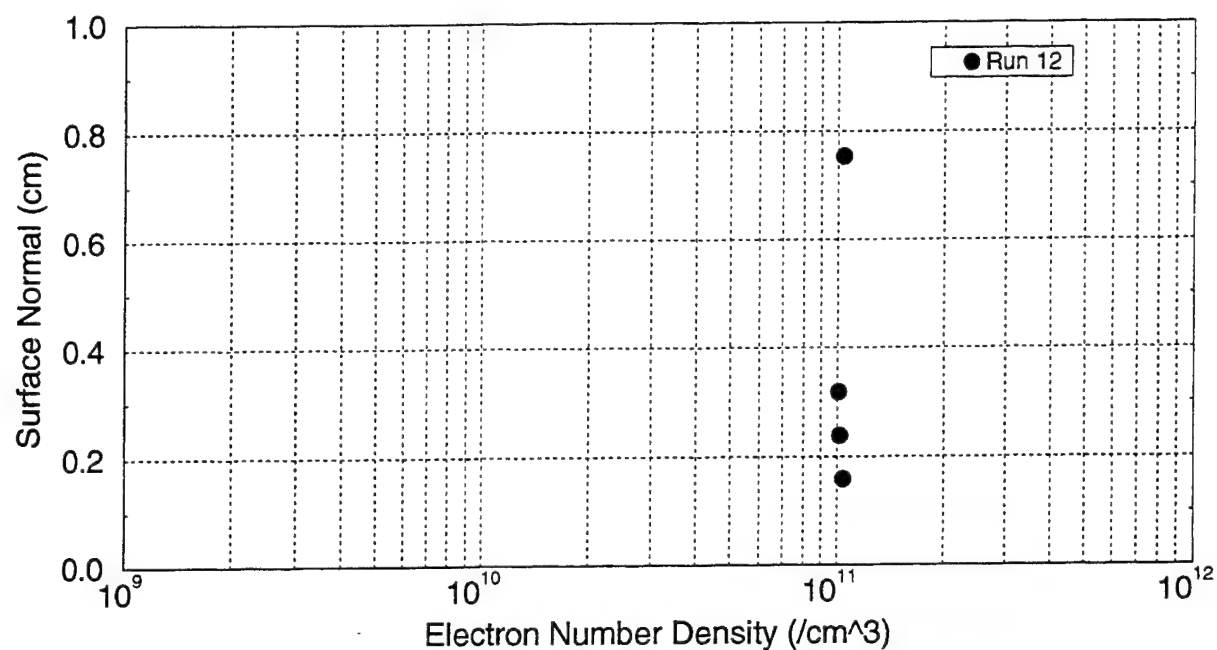


Figure F-9 Electron Number Density Profile, Test Run 12

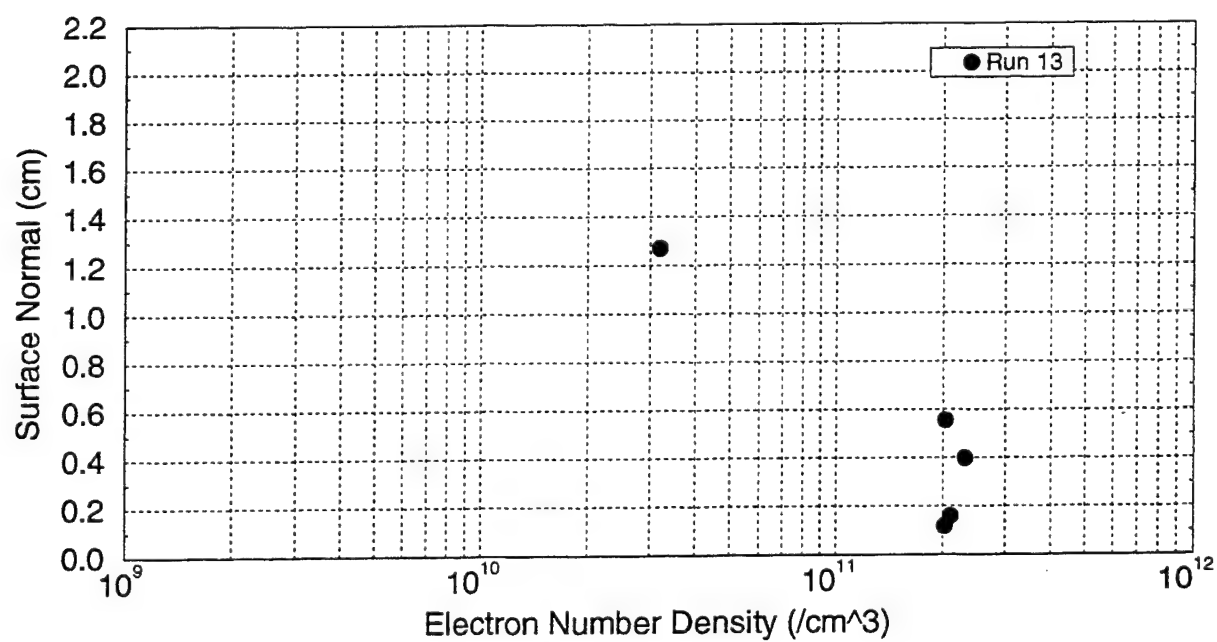


Figure F-10 Electron Number Density Profile, Test Run 13

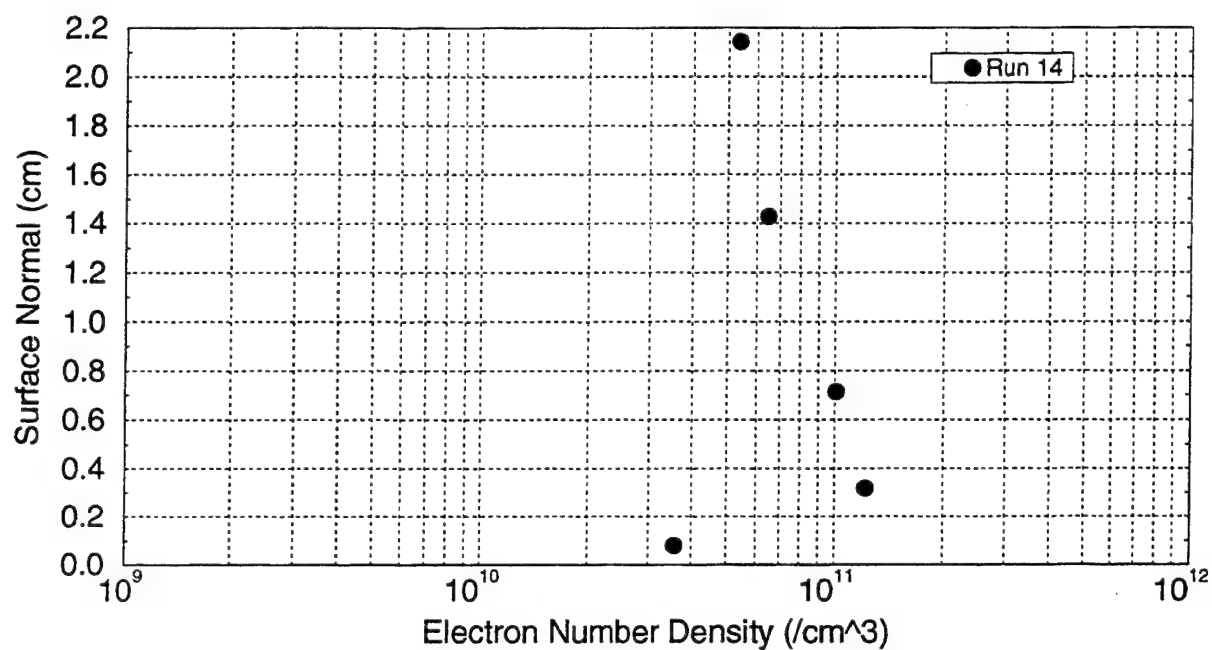


Figure F-11 Electron Number Density Profile, Test Run 14

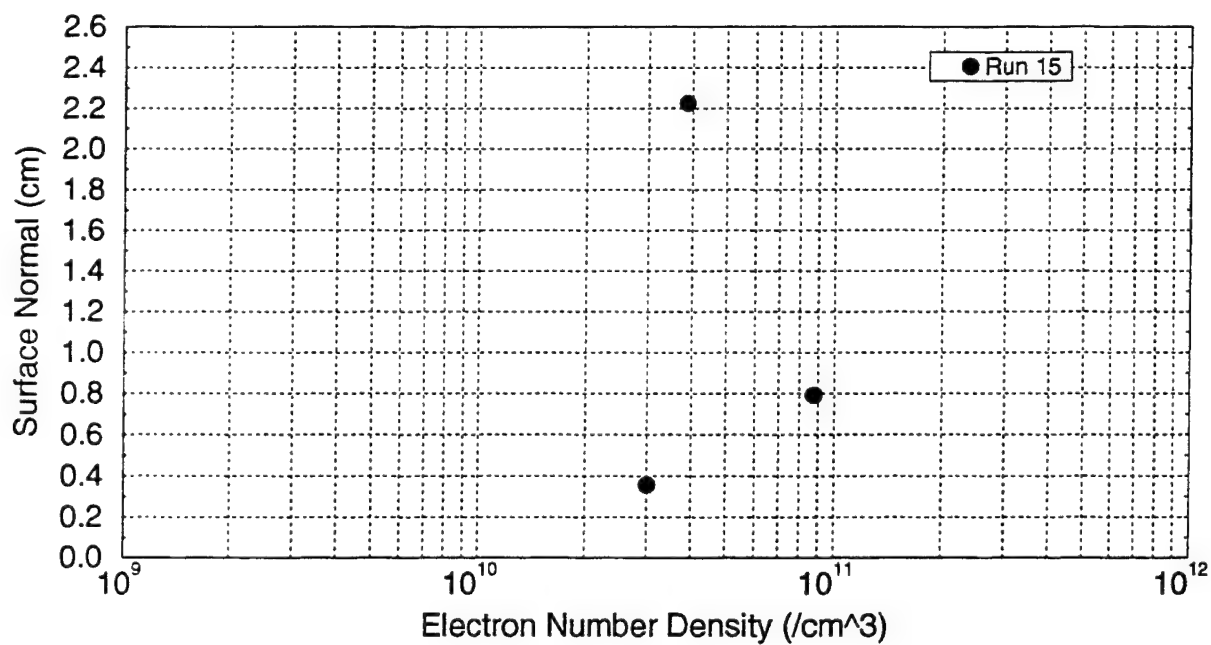


Figure F-12 Electron Number Density Profile, Test Run 15

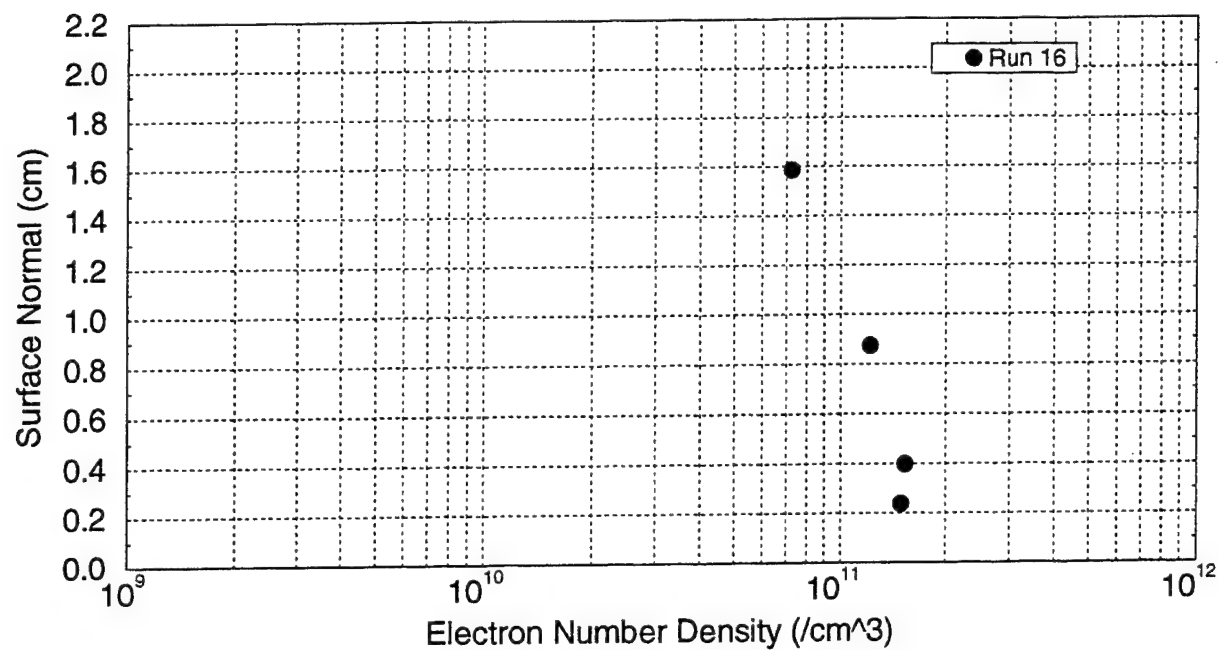


Figure F-13 Electron Number Density Profile, Test Run 16

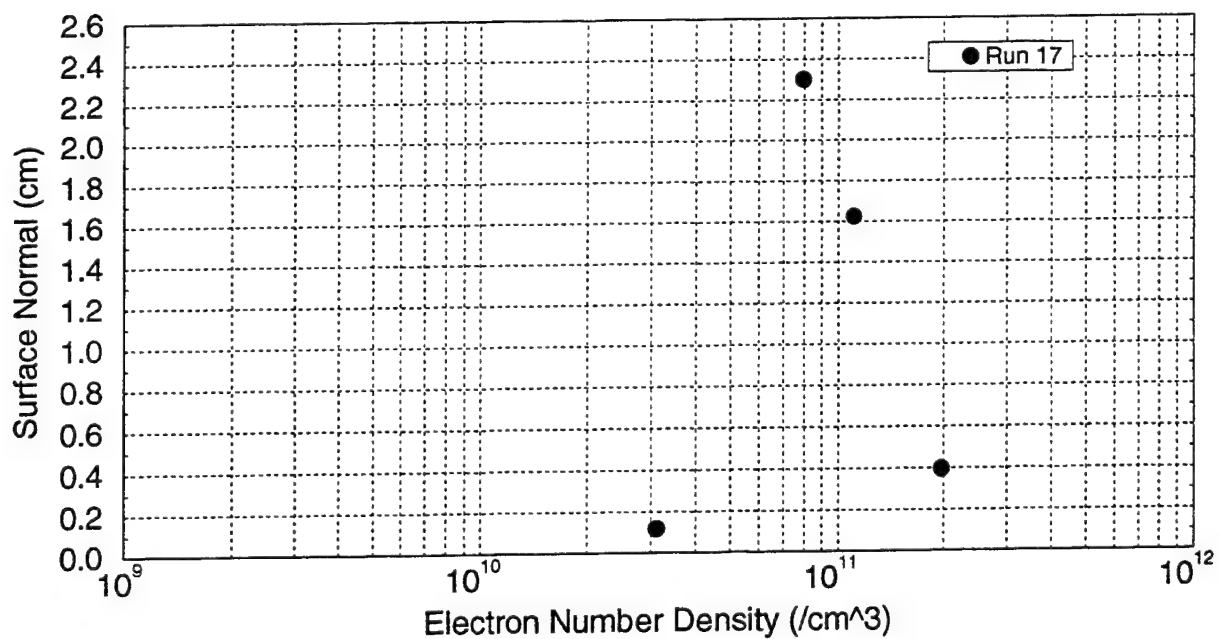


Figure F-14 Electron Number Density Profile, Test Run 17

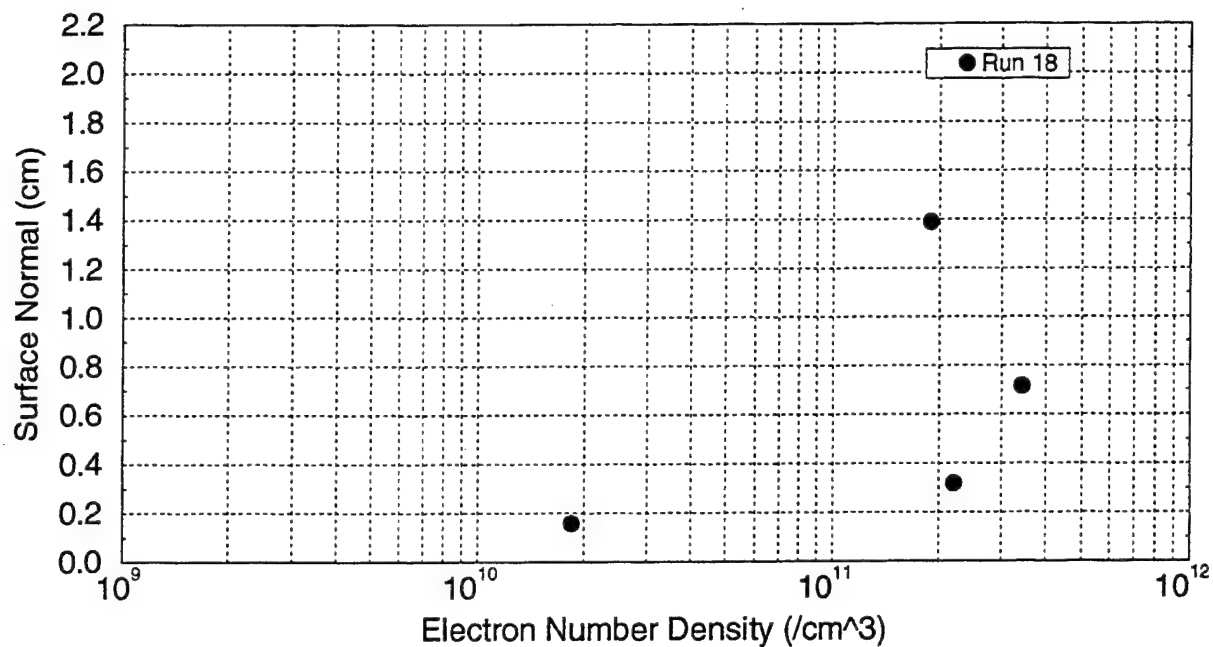


Figure F-15 Electron Number Density Profile, Test Run 18

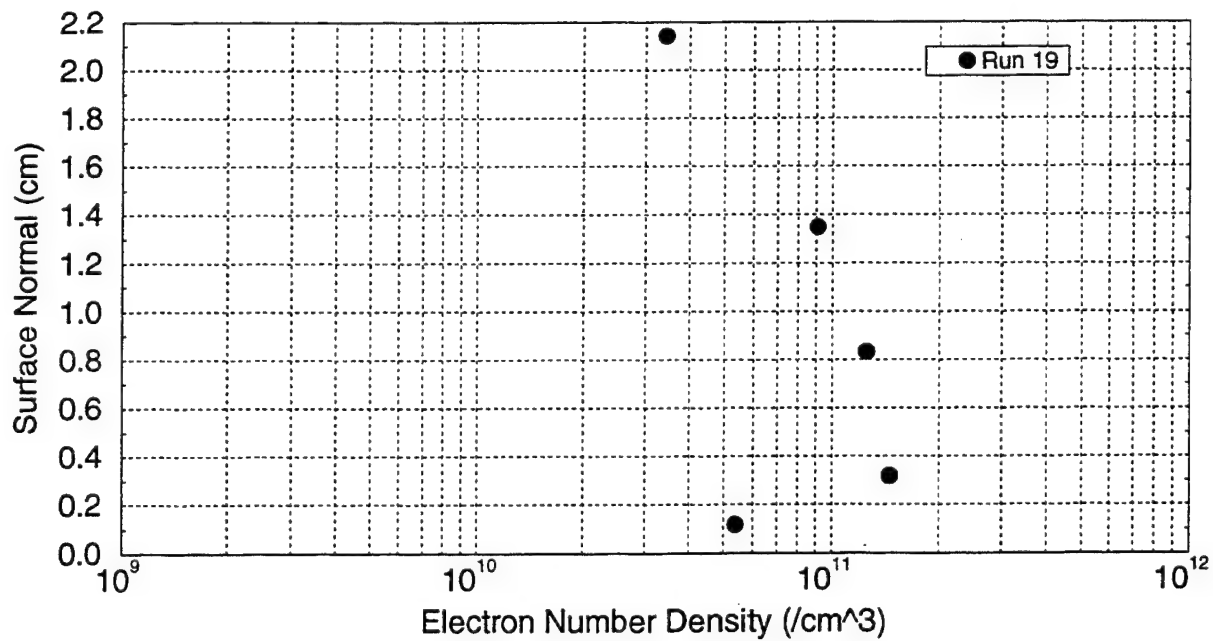


Figure F-16 Electron Number Density Profile, Test Run 19

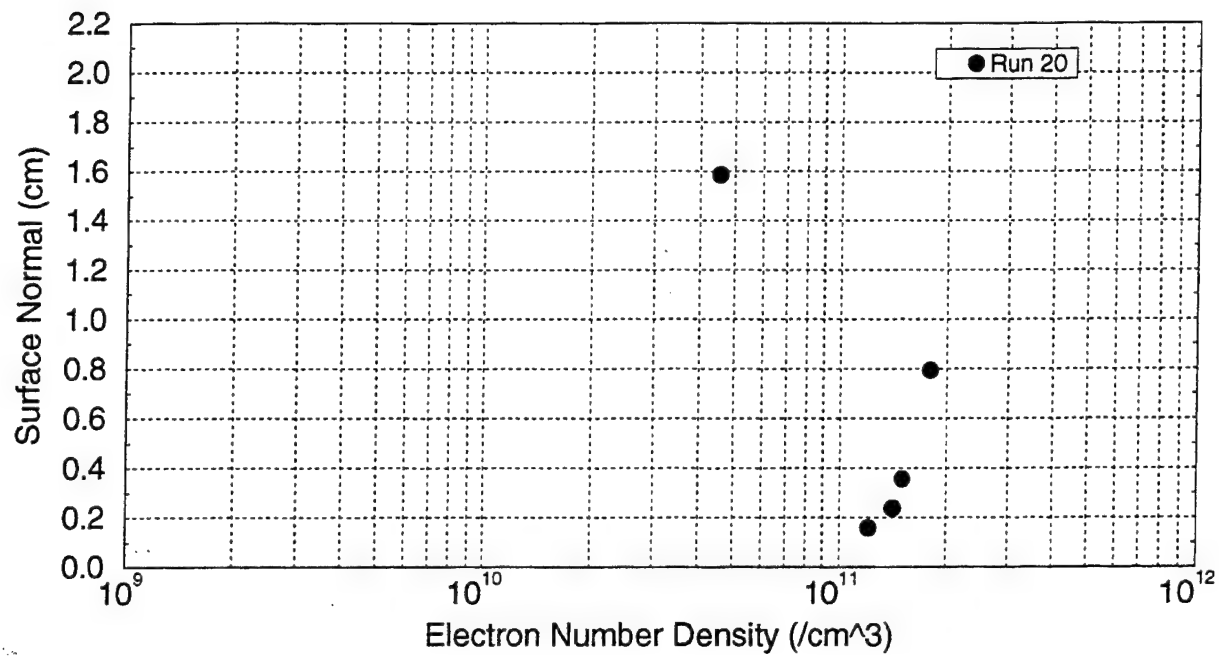


Figure F-17 Electron Number Density Profile, Test Run 20

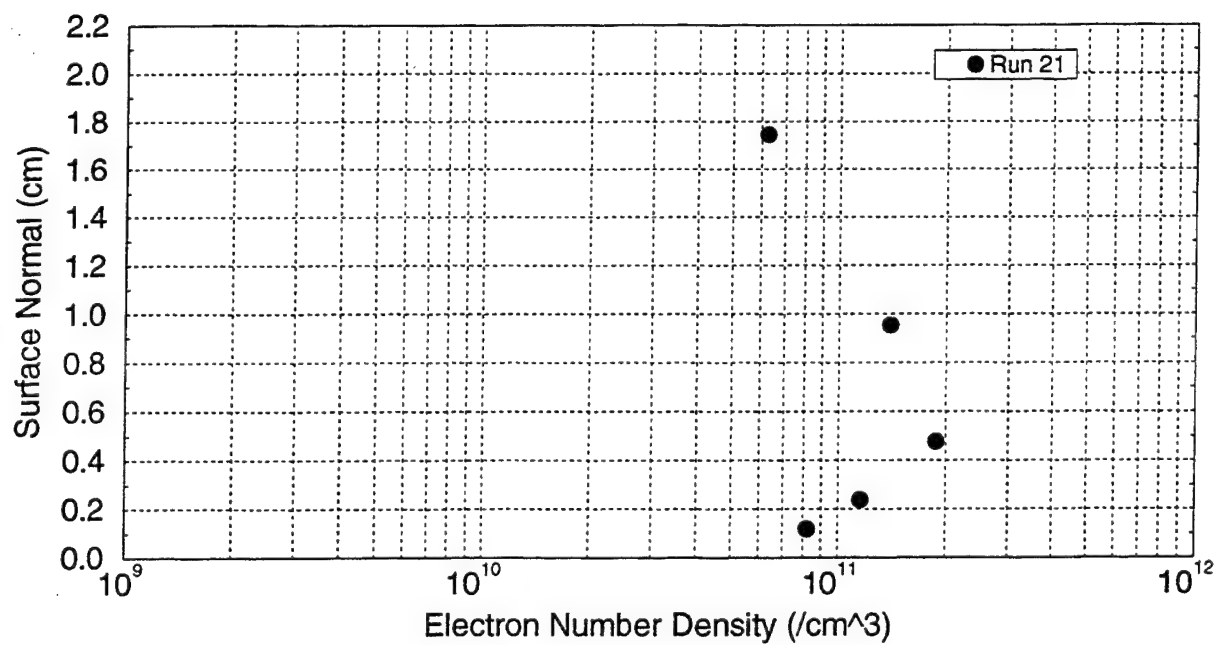


Figure F-18 Electron Number Density Profile, Test Run 21

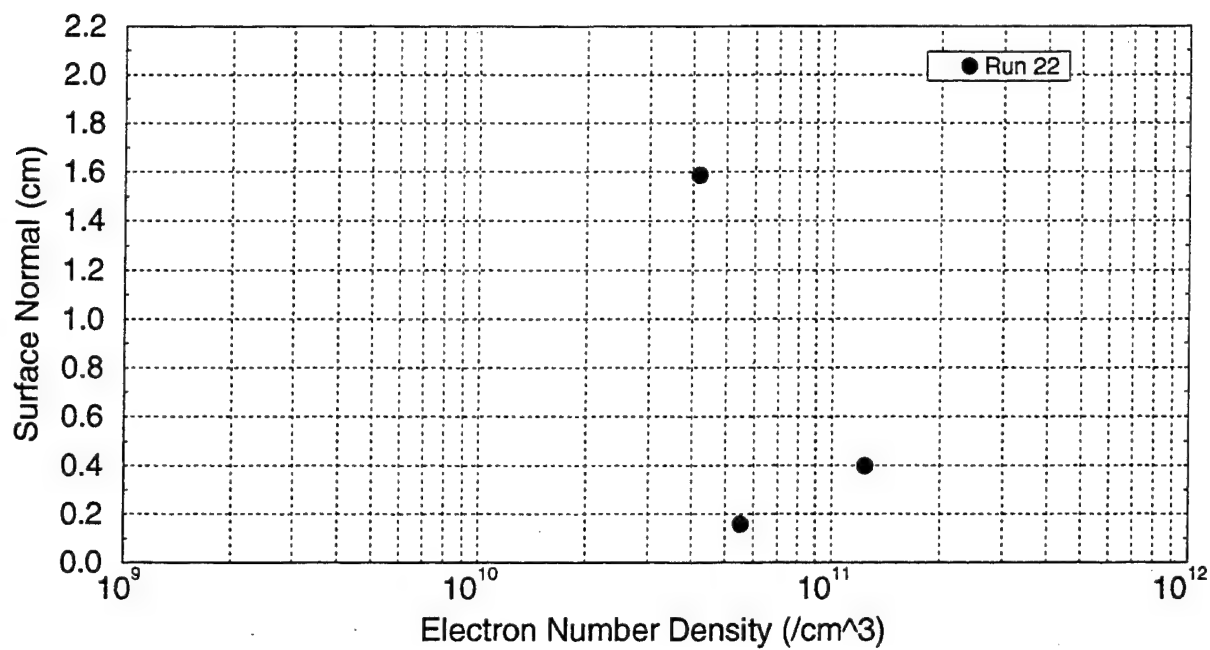


Figure F-19 Electron Number Density Profile, Test Run 22

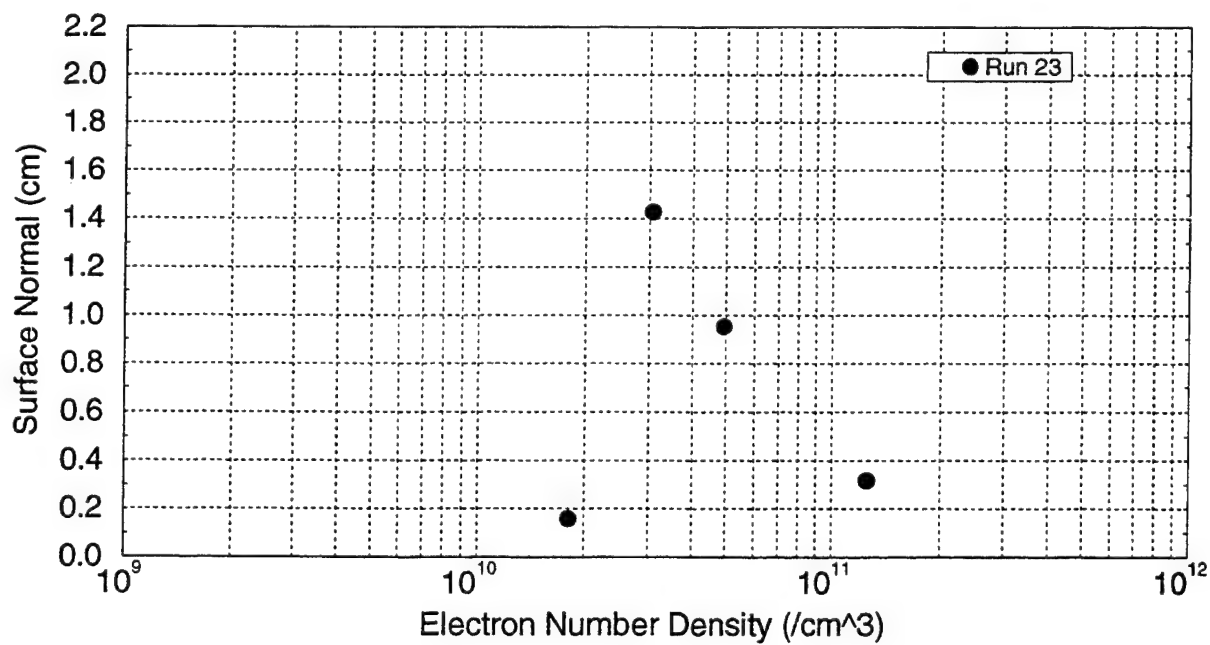


Figure F-20 Electron Number Density Profile, Test Run 23

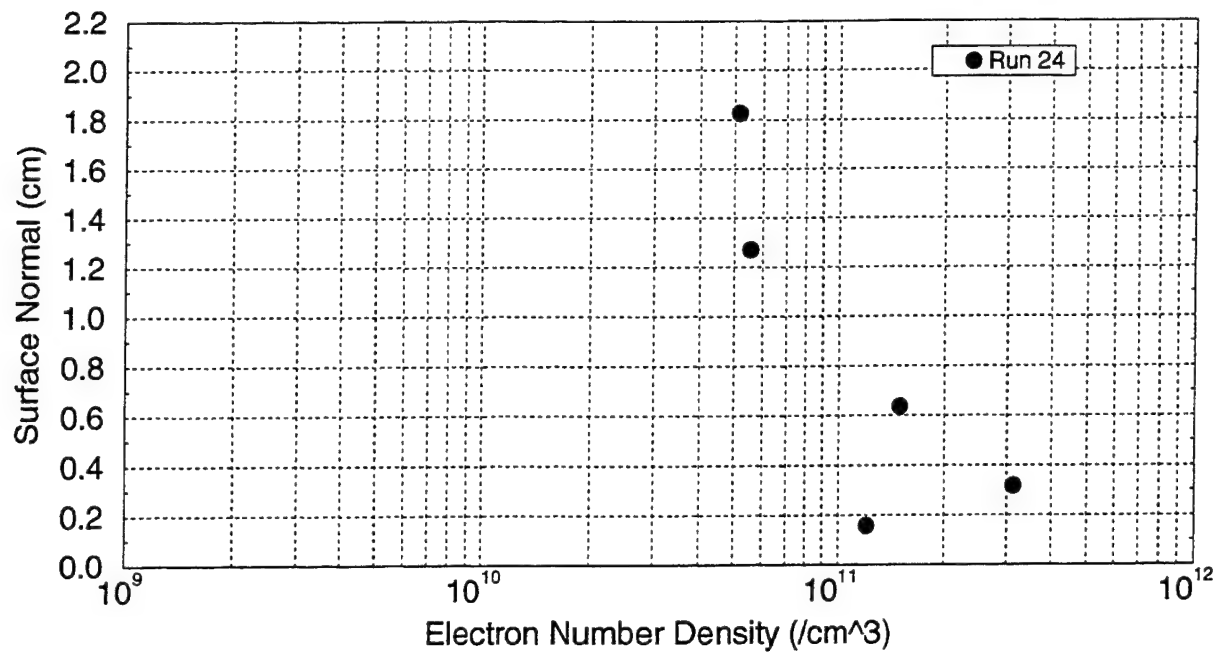


Figure F-21 Electron Number Density Profile, Test Run 24

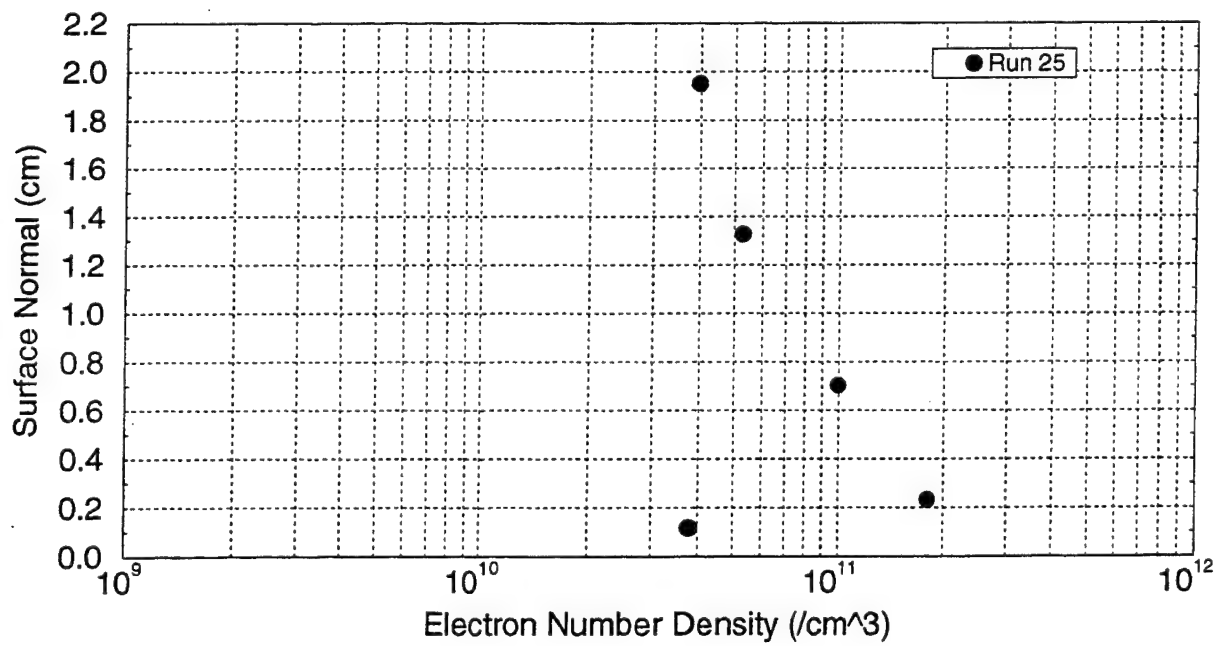


Figure F-22 Electron Number Density Profile, Test Run 25

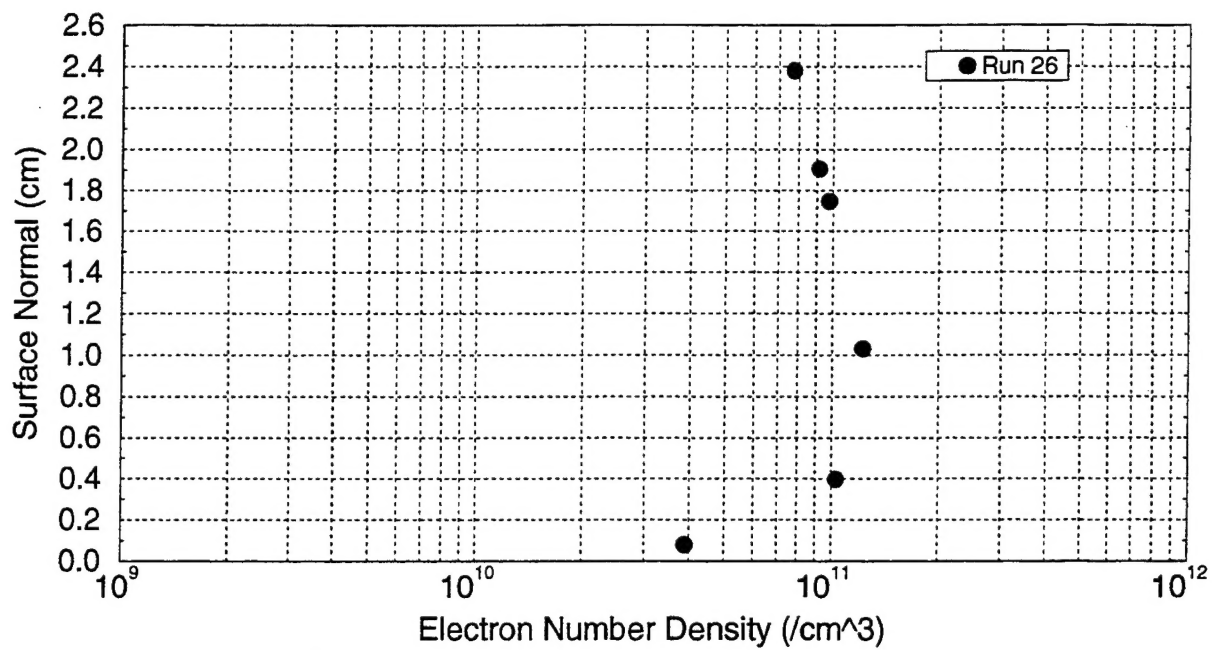


Figure F-23 Electron Number Density Profile, Test Run 26

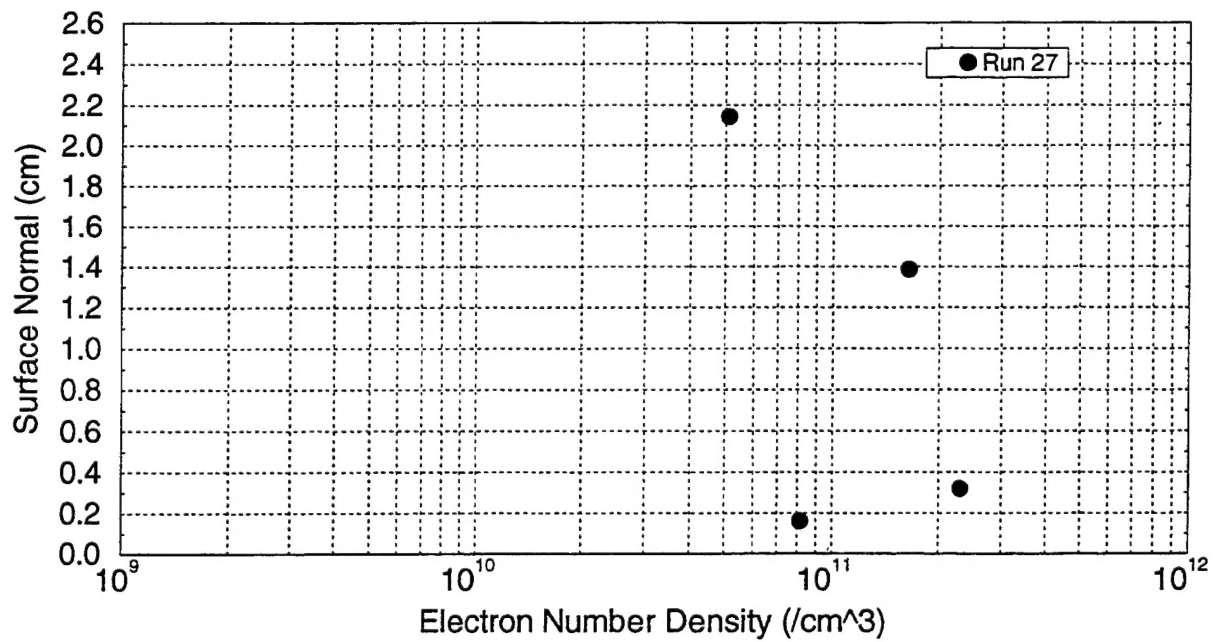


Figure F-24 Electron Number Density Profile, Test Run 27

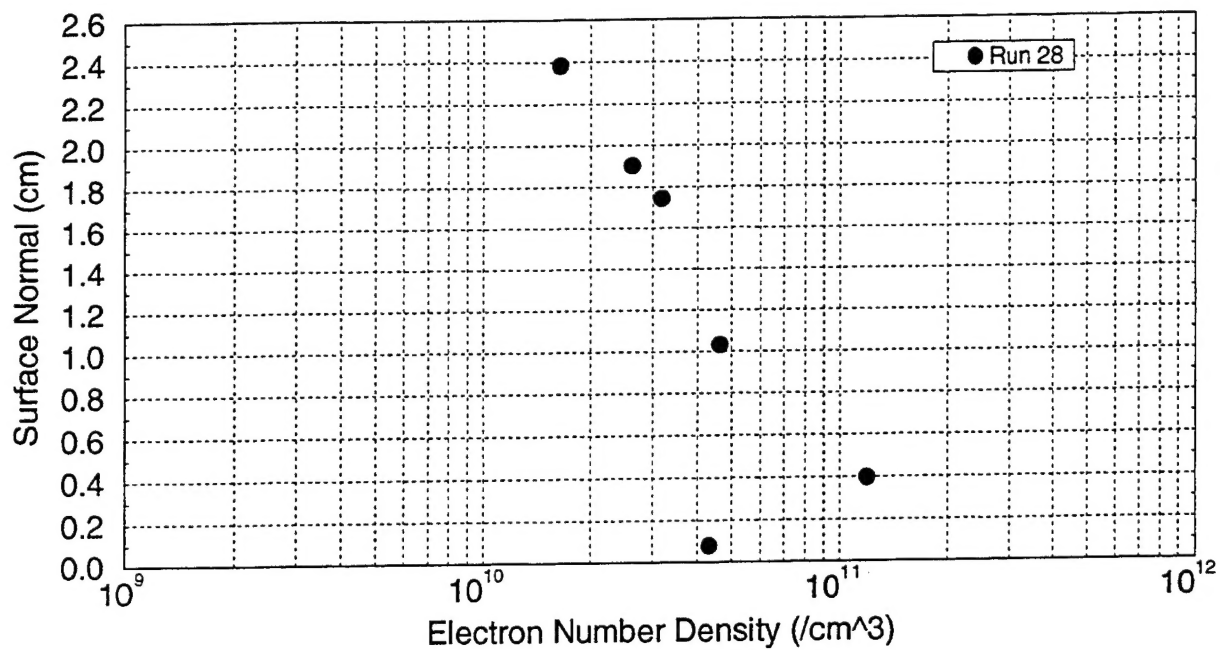


Figure F-25 Electron Number Density Profile, Test Run 28

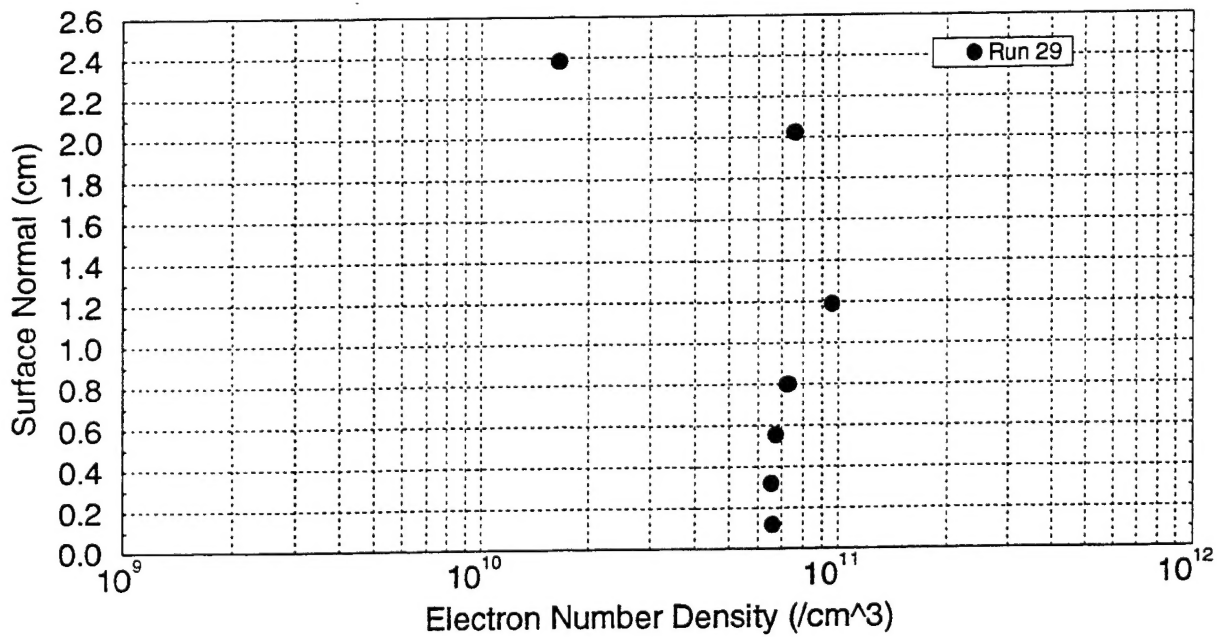


Figure F-26 Electron Number Density Profile, Test Run 29

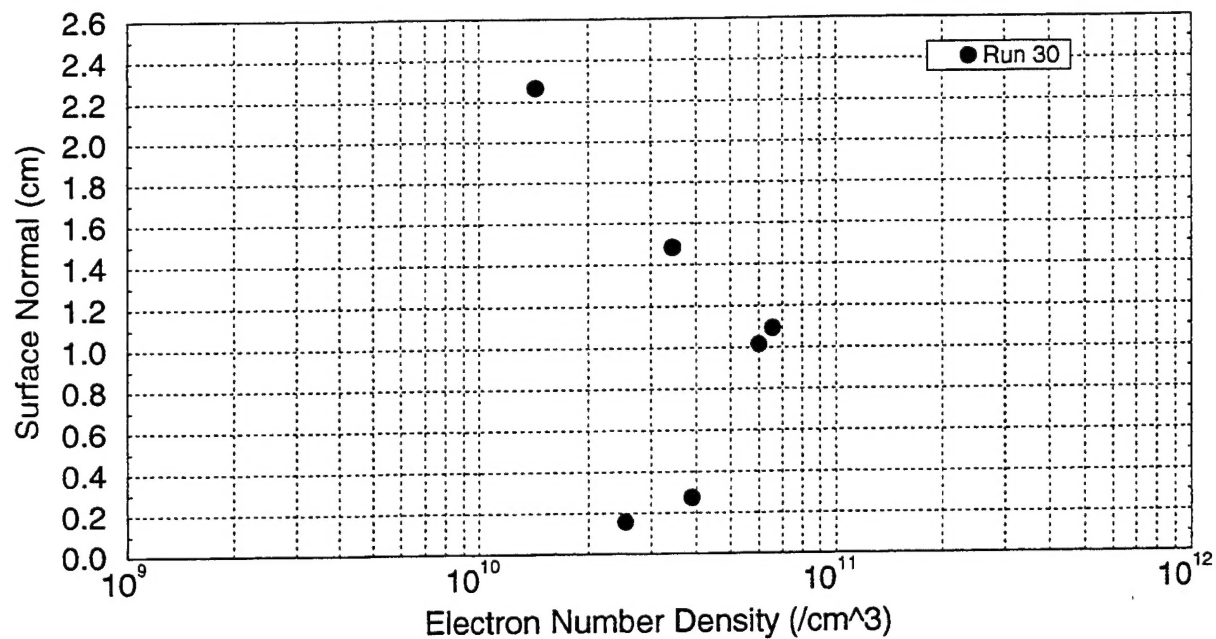


Figure F-27 Electron Number Density Profile, Test Run 30

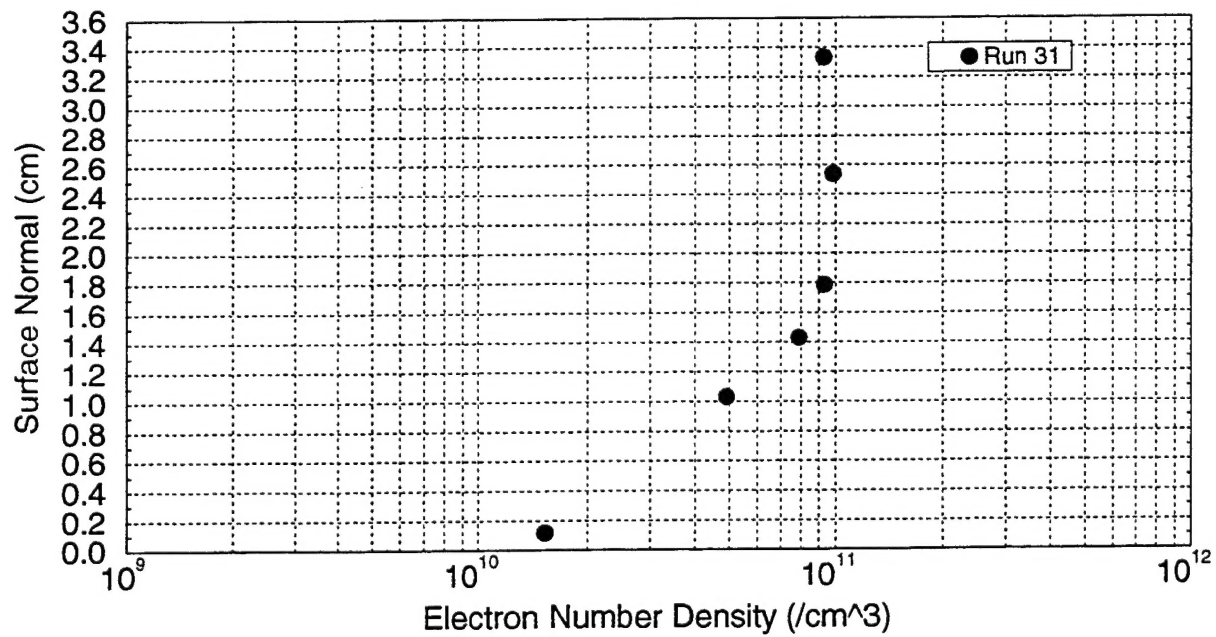


Figure F-28 Electron Number Density Profile, Test Run 31

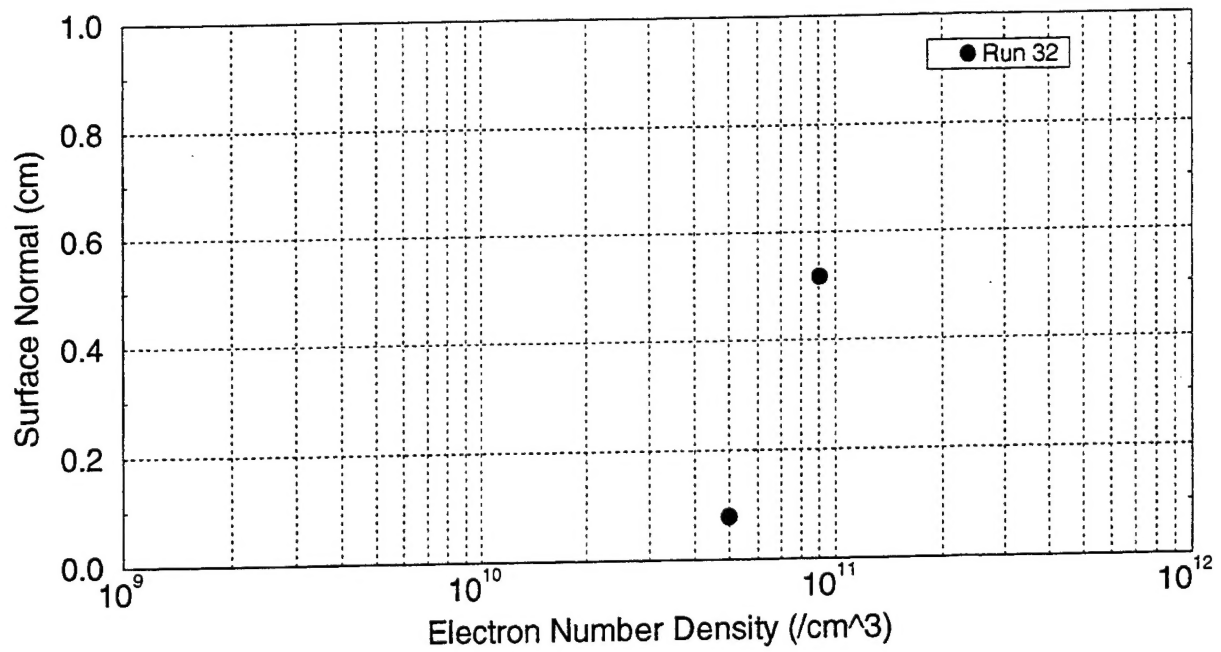


Figure F-29 Electron Number Density Profile, Test Run 32

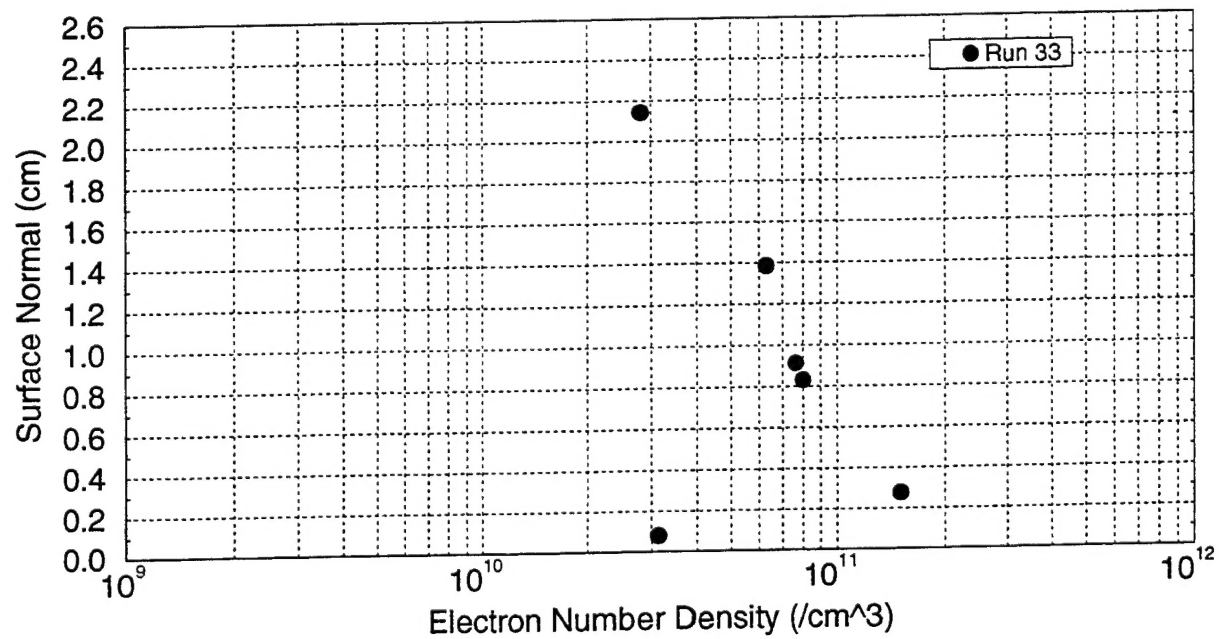


Figure F-30 Electron Number Density Profile, Test Run 33